Doctoral Thesis

# Enhancing Mechanical Properties of Nanoporous Gold by Controlling External and Internal Microstructural Factors

Eun-Ji Gwak

Department of Materials Science and Engineering

Graduate School of UNIST

2019

# Enhancing Mechanical Properties of Nanoporous Gold by Controlling External and Internal Microstructural Factors

Eun-Ji Gwak

Department of Materials Science and Engineering

Graduate School of UNIST

# Enhancing Mechanical Properties of Nanoporous Gold by Controlling External and Internal Microstructural Factors

A thesis/dissertation
submitted to the Graduate School of UNIST
in partial fulfillment of the
requirements for the degree of
Doctor of Philosophy

Eun-Ji Gwak

6. 10. 2019

Approved by

Ju-Young Kim

Advisor
Prof. Ju-Young Kim

# Enhancing Mechanical Properties of Nanoporous Gold by Controlling External and Internal Microstructural Factors

Eun-Ji Gwak

This certifies that the dissertation of Eun-Ji Gwak is approved.

6.10.2019

signature
Ju-Young Kim
Advisor: Prof. Ju-Young Kim

signature
Prof. Sukbin Lee

signature
Prof. Han Gi Chae

signature
Prof. Eun-chae Jeon

signature
Prof. Young-Cheon Kim

# Abstract

Mechanical integrity becomes a decisive factor to assess applicability of nanoporous materials due to their mechanical fragility in tension. Nanoporous materials with large surface area and physicochemical reactivity by nanoscale open-cell structure have considerable potential for sensing, actuating and catalytic applications. Since scale of constituent material is in nanometer-scale, nanoporous metals show unique mechanical characteristics due to large free surface and confined volume for deformation.

The goal of this research is investigation of mechanical properties of nanoporous gold(np-Au) depending on external and internal microstructure based on the nanomechanics and suggesting process to enhance mechanical reliability of np-Au.

Mechanism of indentation size effect in nanoindentation with sharp tip and spherical tip will be discussed by ligament size dependent plasticity. It has been well-known that indentation hardness is increased with decreasing ligament size similarly to size effect in nanopillar compression where probability of dislocation existence in very small volume determine strength of nanopillar. Nanomechanical modeling and experimental results from uniaxial compression, pure shear test and nanoindentation well-describes mechanism of indentation size effect in np-Au regarding of ligament size.

Fabrication methods for nanocrystalline, prestrained and nanotwinned np-Au is suggested and mechanical properties and deformation behavior is described by interaction of dislocation with internal microstructural factors. Grain boundary, twin boundary and dislocations are important defects which determine mechanical behavior of metals by acting as obstacles of dislocation movement. In np-Au, dislocation motion in ligaments and junctions are responsible for deformation. Nanoindentation, flexural test and in-situ tensile test are conducted to investigate effect of microstructural defects on mechanical behavior of np-Au. Nanomechanical studies reveal that grain boundaries weaken flexural strength of np-Au, on the other hand, nanotwin structure in ligament improves tensile strength of np-Au.

# Contents

**1. Research Background**

**2. Mechanical Behavior of Np-Au Depending on External Microstructures**

**3. Mechanical Behavior of Np-Au Depending on Internal Microstructures**

# List of Figures

# 1. Introduction

Nanoporous metal(np-metal) foams is a cellular material that has three-dimensional bicontinuous porous structure composed with interconnected solid metal ligaments and pores. In general, np-metals exhibit porosity of more than 50% and pore size of several nanometers to micrometers. Random nanoporosity in np-metals leads to high surface-to-volume ratio and unique chemical, physical and mechanical properties. Based on these advantages, np-metals have attracted considerable attentions in various applications such as sensors, catalysts, actuators, capacitors and biomedical fields[1-6].

Np-metals are usually fabricated by selective dissolution of sacrificial element from precursor alloy, which is called dealloying process. In order to obtain uniform nanoporous structure, precursor alloys are preferred to be solid solution or metallic glass of more than two elements with suitable composition for uniform porous structure and there should be difference in chemical reactivity for selective etching. During dealloying, less noble element dissolves into etchant leaving more noble element at dealloying surface and left noble adatoms agglomerate into interconnecting ligaments. Ligament size is the most important factor to determine various properties of np-metals because it is directly related with surface area. We can adjust pore and ligament size in np-metals by controlling dealloying conditions such as temperature and concentration of etchant and dealloying time[7]. Details of synthesis for np-Au will be addressed in Chapter 2.

Mechanical properties of np-metals are also dependent on ligament size and relative density. In many previous researches, strength of pillar increases with decreasing diameter since probability of existence of dislocation source becomes rare as sample size decreases[8-10]. In the same line with size effect in nanopillar compression, strength of np-metal increases with decreasing ligament size[11-12]. During deformation of np-metals, dislocations are generated neck surface of hourglass-shaped ligament and move to opposite neck surface or thicker junction and slip motions are confined in very small volume of ligaments[13]. Also, nanopores in np-metal volume could act as stress concentrator that make crack propagation faster than solid material showing brittle failure in tension. Brittleness of np-metals is the most critical issue for practical application where mechanical reliability should be assured. Research background about mechanical properties of np-metals will be addressed in Chapter 2 as well.

Though microstructural characteristic lengths such as ligament size, grain size, initial dislocation density and twin spacing, which have played a considerable role in deformation behavior in metals, should be involved in deformation behavior of np-metals, these factors have not been considered comprehensively. In this research, np-gold(np-Au) is chosen as a typical np-metal as it has chemical inertness and ease of fabrication and systematic studies for structure-property relations of np-metals are introduced.

In the Chapter 3, indentation size effect in nanoindentation on np-Au is investigated regarding with ligament size[14]. As ligament size increased, more dislocation sources could exist in ligaments causing dissimilar response during nanoindentation. Nanomechanical modeling is suggested for indentation size effect in np-metals and deformation mechanism depending on ligament size is discussed based on uniaxial compression and pure shear tests.

In the Chapter 4, effects of internal microstructure in ligaments on mechanical properties and deformation behavior are researched based on nanomechanics. Nanocrystalline np-Au is fabricated by using ball-milled precursor alloy and nanoindentation and flexural test are conducted to investigate mechanical properties by microstructural factors[15]. Nanotwinned np-Au is synthesized by using optimized conditions in co-sputtering of precursor foil. By correlating microstructure and mechanical properties, we can design and manufacture np-metals with desirable performance for applications[16].

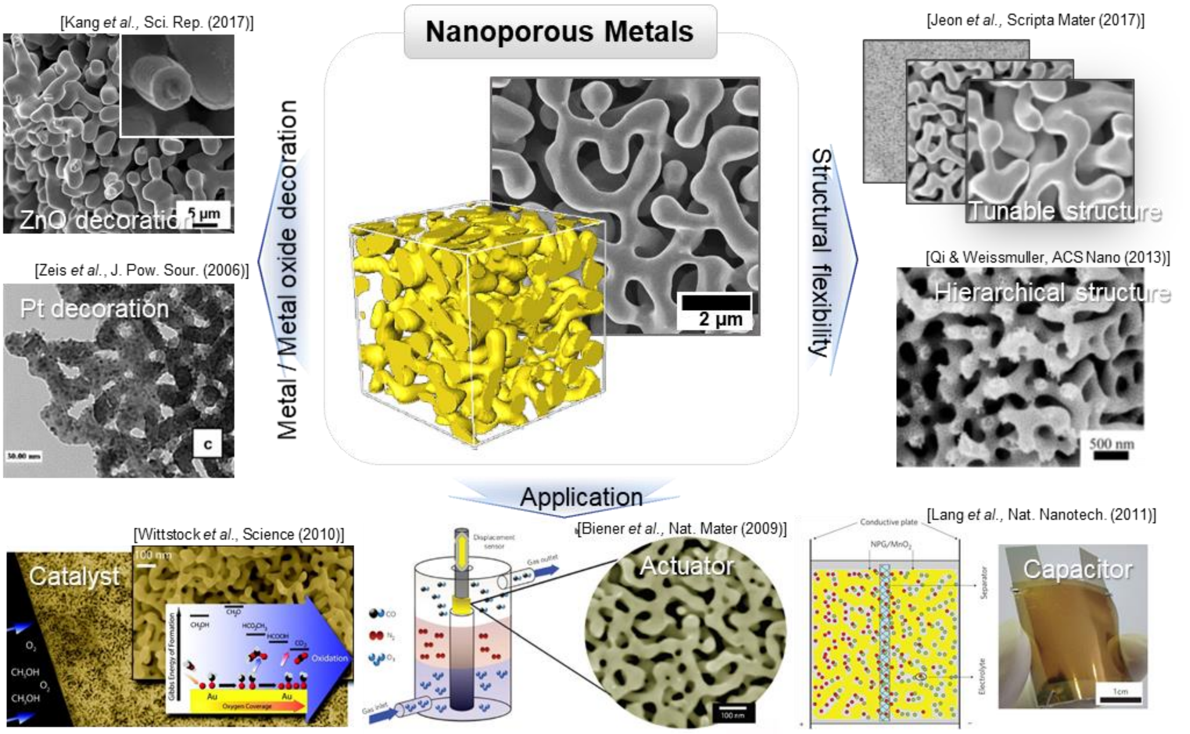

**Figure 1** Wide research area of nanoporous metals ranging from structural tunability (adapted from Jeon et.al., Copyright 2017 Elsevier[17] and Qi and Weissmuller Copyright 2013 American Chemical Society[18]) , heterogeneous composites(adapted from Kang et.al., Copyright 2017 Nature[19] and Zeis et.al., Copyright 2006 Elsevier[20]) to various applications with large surface area(adapted from Wittstock et.al., Copyright 2010 Science[21], Biener et.al., Copyright 2009 Nature[22] and Lang et.al., Copyright 2011 Nature[4]).

# 2. Research Background

## 2.1 Fabrication of np-Au

Fabrication strategies for np-metals have been numerously suggested until now from bottom-up method such as self-assemble of nanoparticles[23] to top-down method such as template deposition[24] and combustion synthesis[25]. Among various synthesis technique of np-metals, dealloying is the most notable fabrication method for np-metals based on corrosion of selective element in precursor[26-27]. So, precursor alloy consists of at least two elements and there should be difference in electrochemical potential for selective dissolution. For np-Au, many precursor alloy systems such as Au-Ag, Au-Cu and Au-Ni have been used in researches and Au-Au binary alloy is the most likely used. Au-Ag precursor alloy forms solid solution in entire range of composition, as shown in Fig. 2-1, because gold and silver have FCC structure, similar lattice constant and large difference in chemical activity. Single phase of Ag-Au precursor alloy makes np-Au to produce uniform and homogeneous nanoporous structure during dealloying.

In general, Au-Ag precursor alloy is fabricated in multi-scale using furnace or arc-melting system for bulk-scale sample and sputtering system or thermal evaporator for nano- to micro-scale sample. Bulk-scale Ag-Au alloy is synthesized by melting pure Ag and Au source at very high temperature in furnace. Ag-Au alloy thin film or foil could be fabricated using co-sputtering of highly pure Ag and Au target on desirable substrate. This method has advantages of controlling composition by sputtering power and thickness by sputtering time and working pressure. Microstructure in precursor alloy thin film is also diversified by sputtering conditions such as temperature and deposition rate. After alloying processes above, precursor alloy should undergo homogenization step for uniform solid solution phase and uniform composition in total volume of sample in order to obtain uniform nanoporous structure and ligament size. Homogenization temperature has to be decided considering phase diagrams with substrate material and adhesive layer to block diffusion of those un-wanted elements.

Dealloying is a common process to produce nanoporous structure from precursor alloy using difference in chemical reactivity in electrolyte. It could be conducted by either free corrosion without external potential or electrochemical dealloying with external potential depending on sacrificial element and target microstructure. Competition between selective etching of less noble element and surface diffusion of more noble element generates bicontinuous open-cell nanoporous structure during dealloying. For Ag-Au precursor alloy, less noble Ag element dissolves into nitric acid by reaction below leaving Au adatoms on surface and Au adatoms agglomerate by surface diffusion making Au islands.

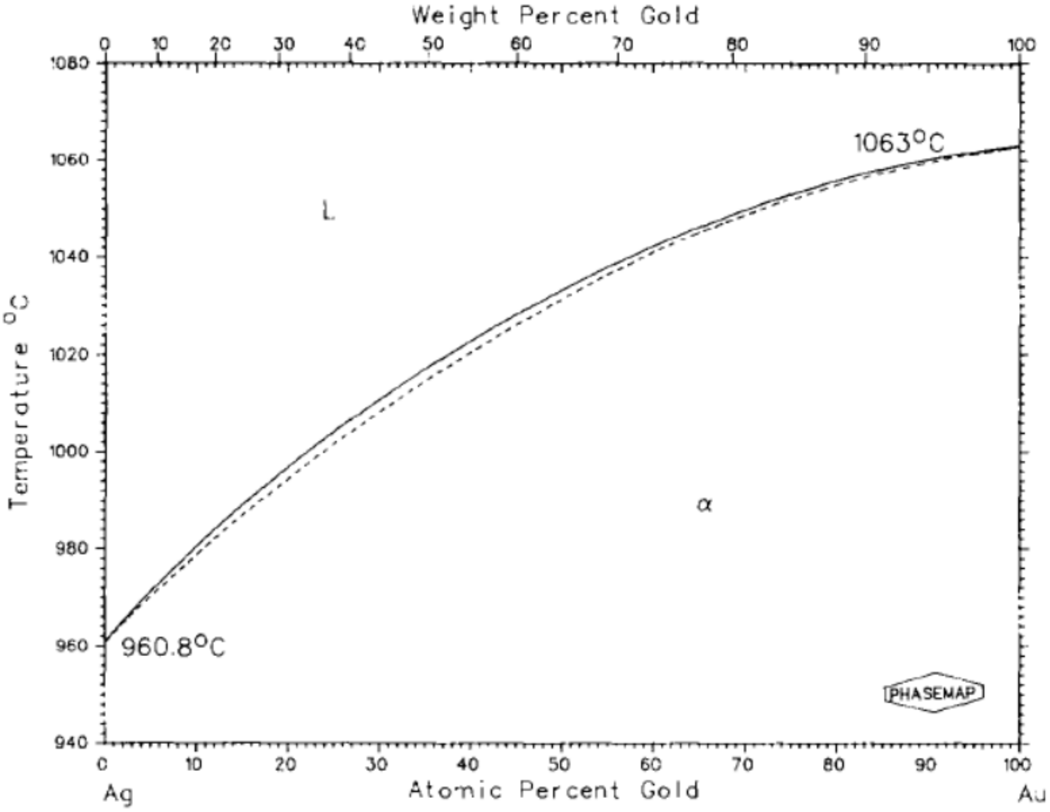

**Figure 2-1** Binary phase diagram of gold and silver. Au-Ag alloy exist as solid solution in entire range of composition. (adapted from Elliott and Shunk Copyright 1980 Springer Nature [28])

$$\mathrm{Ag}(s) + \mathrm{HNO_3}(aq) \rightarrow AgNO_3(aq) + \frac{1}{2}H_2(g)$$

As dealloying process continues, Ag element in internal volume is leached and three-dimensional interconnected ligaments are formed.

Uniform nanoporous structure can be formed with sacrificial element of suitable composition in precursor alloy. The critical composition of more noble element for complete dealloying is called parting limit[26]. For Ag-Au alloy, Au should be contained in range from 20 to 60 at.%. If amount of Au in precursor alloy is less than 20%, Au nanoparticles are formed rather than interconnected ligament. If composition of Au is higher than 60%, passivation layer of Au is formed at surface halting further dissolution of Ag and formation of nanoporosity. Therefore, atomic proportion of more noble and less noble element in precursor alloy has to be considered to control dealloying process.

Dissolution of half or over half of elements into electrolyte causes change in composition and microstructure and volume contraction during dealloying. Volume contraction leads to generate microcracks and change in relative density, ratio of np-Au density to pure gold density, which is closely related with mechanical properties of np-metals.

It has been reported that defects such as dislocations or twin structure are produced after dealloying because of plastic deformation of ligaments due to surface-induced stress during dealloying. Those plastic deformation in ligament during dealloying could be origin of volume contraction in np-Au. While surface crack generated during dealloying could induce reliability issue by lowering mechanical properties of np-metals, techniques to regulate crack formation have been suggested. For example, surface crack in np-metal could be formed by fast dissolution of Ag by reducing time of surface diffusion of Au. Base on this, researchers have been revealed that volume contraction and crack formation could be reduced by slow dissolution condition or stepped-dealloying process[29].

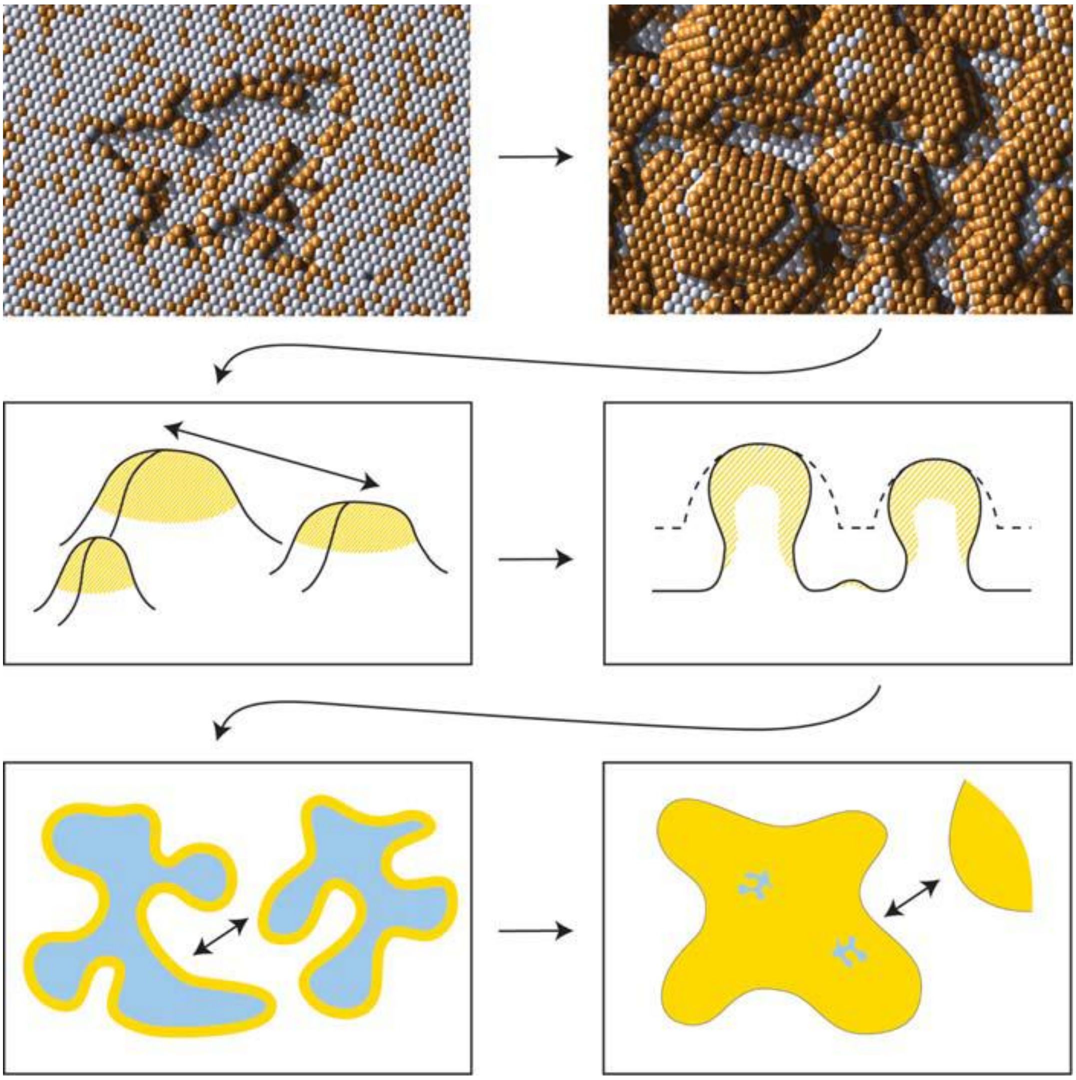

**Figure 2-2** Evolution of nanoporosity during dealloying. Dissolution of less noble element (in this case, silver) and surface diffusion of more noble element (in this case, gold) produce bicontinuous nanoporous structure and further coarsening occurs in more dealloying time. (adapted from Erlebacher and Sechadri Copyright 2011 Cambridge University Press [30])

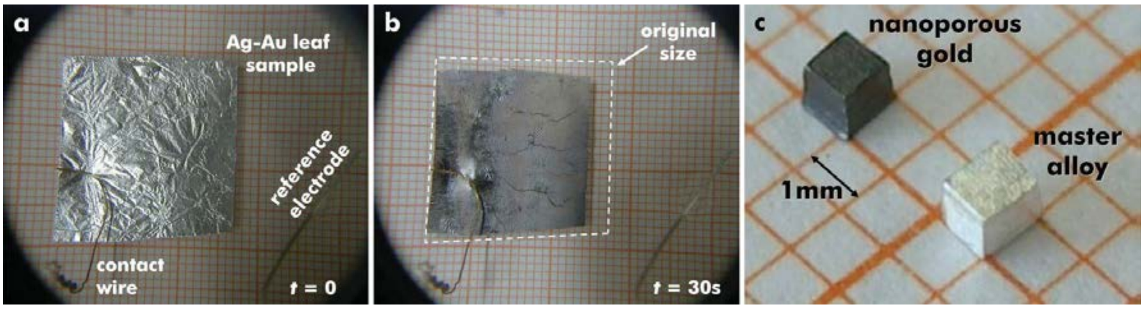

**Figure 2-3** Volumetric contraction during dealloying (adapted from Parida et. al., Copyright 2006 American Physical Society[31]).

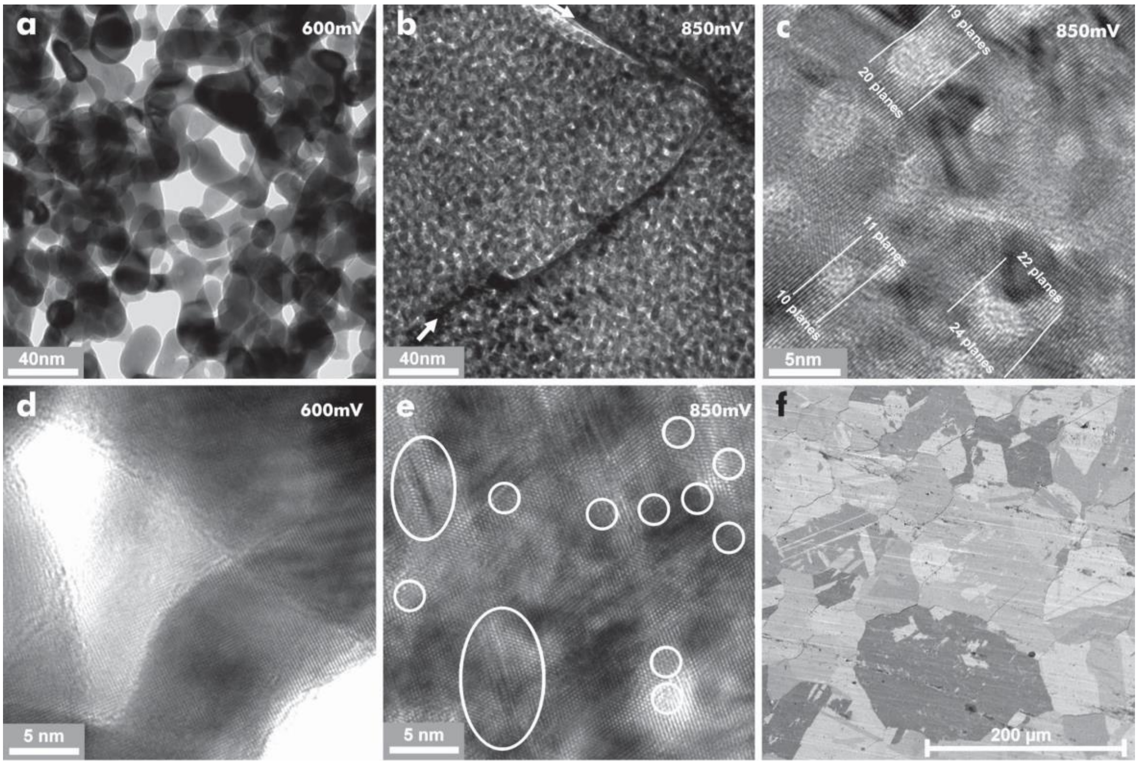

**Figure 2-4** TEM images showing volumetric contraction during dealloying. Large amount of lattice dislocations and stacking faults are generated during dealloying process (adapted from Parida et. al., Copyright 2006 American Physical Society [31]).

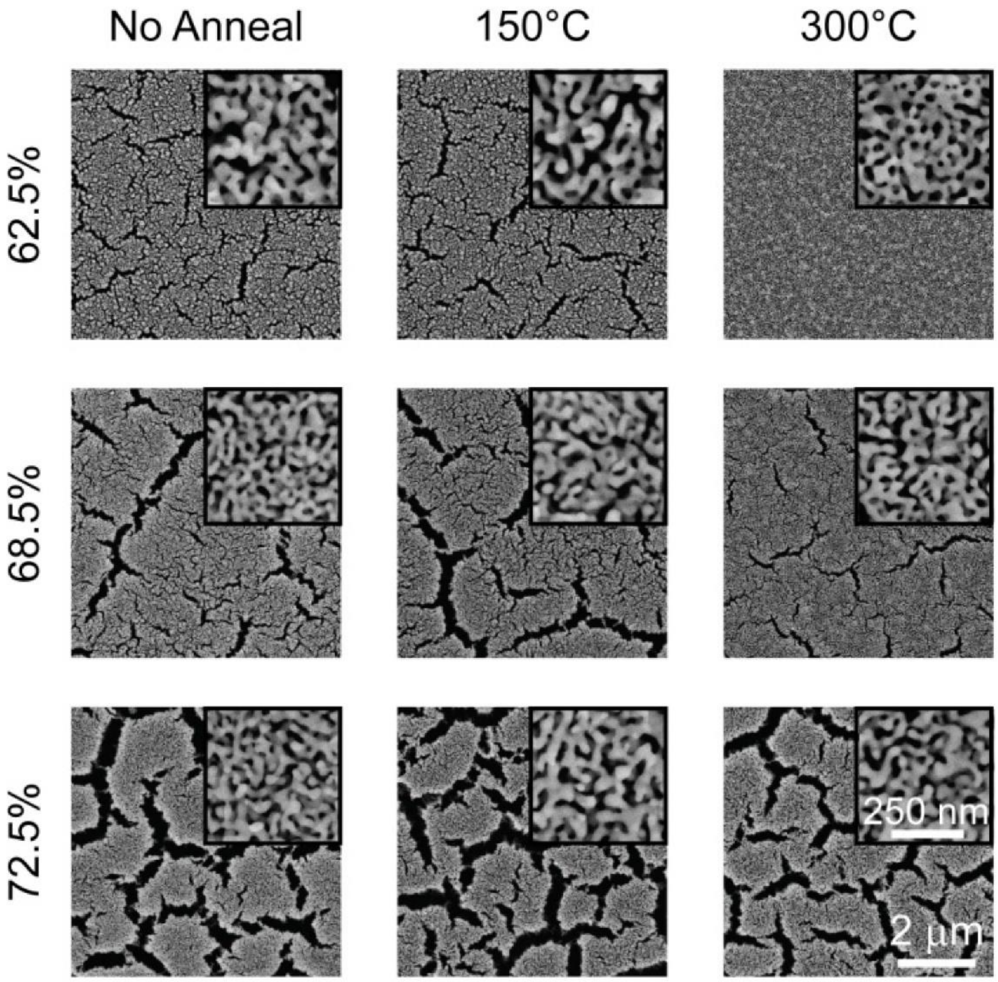

**Figure 2-5** SEM images of nanoporous gold thin films with different silver composition and annealing temperature. Large density of crack in np-Au thin film is produced by constraint of substrate during volume contraction of dealloying (adapted from Seker et. al., Copyright 2009 MDPI [32]).

As mentioned above, dealloying has a huge advantage that microstructure and nanoporosity could be controlled by changing dealloying conditions. In free-corrosion dealloying, immersion of Ag-Au precursor alloy into nitric acid or perchloric acid make nanoporous structure immediately due to large difference in reactivity of Ag and Au for acidic solution. Ligament size is controlled by concentration and temperature of nitric acid and dealloying time in free-corrosion dealloying as they control dissolution rate of Ag and surface diffusion rate of Au. For example, high temperature of nitric acid increase both dissolution rate and surface diffusion rate making coarsened ligament comparing with dealloying in low temperature. Therefore, ligament size '$d(t)$' could be described by function of temperature 'T' as below.

$$d(t)^n = at\exp\left(-\frac{E}{RT}\right),\ \mathrm{D_s} = \frac{d(t)^4 kT}{32\gamma t a^4} \qquad 7$$

where $n$ is exponent for nanoporosity evolution, $a$ is lattice constant, $t$ is dealloying time, $E$ is activation energy for nanoporosity evolution, $R$ is gas constant, $D_s$ is diffusivity of Au, $k$ is Boltzmann constant, and $\gamma$ is surface energy. As described with equation, ligament size is strongly controlled by surface diffusion of Au at interface between alloy surface and electrolyte and ligament size increases with increasing diffusivity of Au[33]. Regrading with concentration of electrolyte, coarsened ligament is obtained by decreasing concentration of nitric acid as dissolution rate of Ag is reduced and time for surface diffusion of Au is extended. However, further dilution of nitric acid retards Ag etching and may cause formation of Ag oxides at dealloying surface. Ag oxide might hinder surface diffusion of Au due to poor solubility of Ag oxide to nitric acid. So, it is hard to obtain nanoporous structure from the inside out.

Figure 2-6 shows surface morphology of np-Au thin film samples obtained from different dealloying conditions. As dealloying temperature increases and concentration decreases, ligament size is increased. Nanoporosity isn't evolved in the case of 20℃, 1:3 (70% $HNO_3$ : $H_2O$) dealloying condition because of low dissolution rate of Ag and formation of Ag oxides at dealloying interface as described above. Free corrosion dealloying has great advantage of ease of process and controlling microstructure of np-Au by changing process conditions. However, it is hard to produce ligament size under 10 nm and control volume contraction and generation of crack.

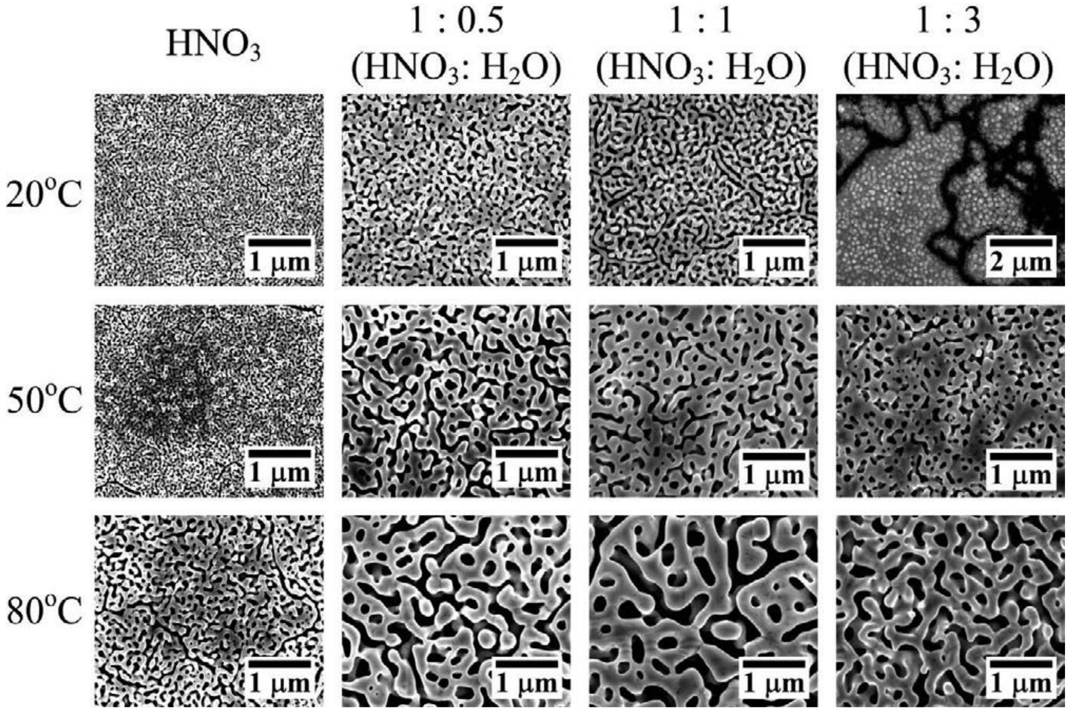

**Figure 2-6** SEM images of nanoporous gold thin films dealloyed in various temperature and concentration of nitric acid etchant. Crack free np-Au thin films are formed by delaminating np-Au films from Si substrate during dealloying (adapted from Gwak et al., Copyright 2013 Elsevier[7]).

Dealloying process by electrochemical method could make up the weakness of free corrosion dealloying[34-35]. By introducing external potential, Ag element is removed from Ag-Au precursor alloy which is served as anode (working electrode) in three-electrode electrochemical cell. Potentiostat could regulate potential and dissolution rate of Ag delicately during dealloying. It provides smaller ligament size and less crack formation than that of free corrosion, however, experimental set-up is more complex.

One of the most important factors in electrochemical dealloying is critical potential, $E_c$. External potential should be applied in some range where less noble element could be removed, but more noble element doesn't. In other words, applied potential has to be higher than dissolution potential of Ag and lower than dissolution potential of Au for selective leaching of Ag. If given potential is too low, Ag will not dissolve into electrolyte and passivation layer of Au will be formed at dealloying surface as shown in Fig. 2-7. If potential is increased to critical potential, dissolution current, which is associated dissolution rate, is rapidly increased exponentially.

Morphology of np-Au can be controlled by conditions of electrochemical dealloying such as temperature of electrolyte, applied current and potential similarly to free corrosion dealloying. As temperature of electrolyte increases, ligament size is also increased due to high surface diffusion rate of Au. Regarding with potential and current, dissolution rate of Ag increases with increasing applied potential and current leading to finer ligament size due to shorter time for surface diffusion. Concentration of electrolyte for electrochemical cell does not affect to microstructure evolution because it serves as electron carrier.

Microstructure of np-metals also depends on whether the potential or current is controlled. Potentiostatic method holds potential at constant value as measuring current change and galvanostatic method holds current at constant value as measuring potential change during dealloying. In potentiostatic electrochemical dealloying, current is proportional to dissolution rate of Ag as they flow between working electrode and counter electrode. When constant potential value is provided, dealloying current is decreasing as dealloying continues while dissolution of Ag is faster at surface than at interior of precursor alloy and amount of Ag is decreased by dissolution. Therefore, residual stress and crack is caused by difference in dissolution rate of Ag and surface diffusion time of Au adatoms between surface and interior. On the other hand, galvanostatic method keeps dissolution rate of Ag constant from beginning to end of dealloying. Therefore, crack formation is prevented in galvanostatic method by alleviating residual stress.

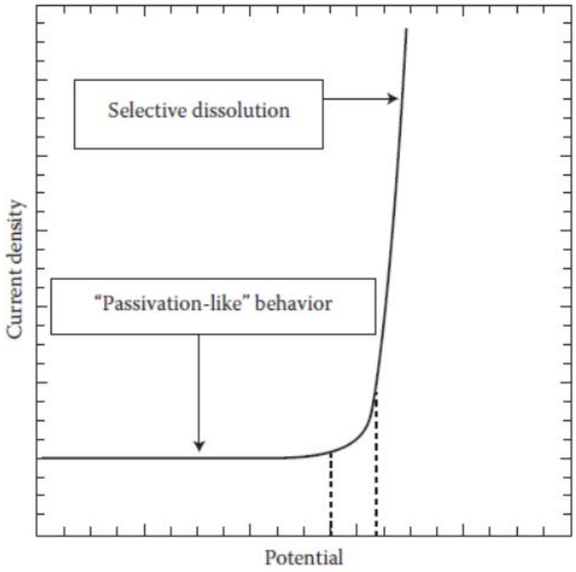

**Figure 2-7** Current/potential behavior undergoing selective dissolution of sacrificial element. Nanoporous structure can be generated above critical potential, $E_c$ (adapted from Sieradzki et al., Copyright 2002, The Electrochemical Society [36]).

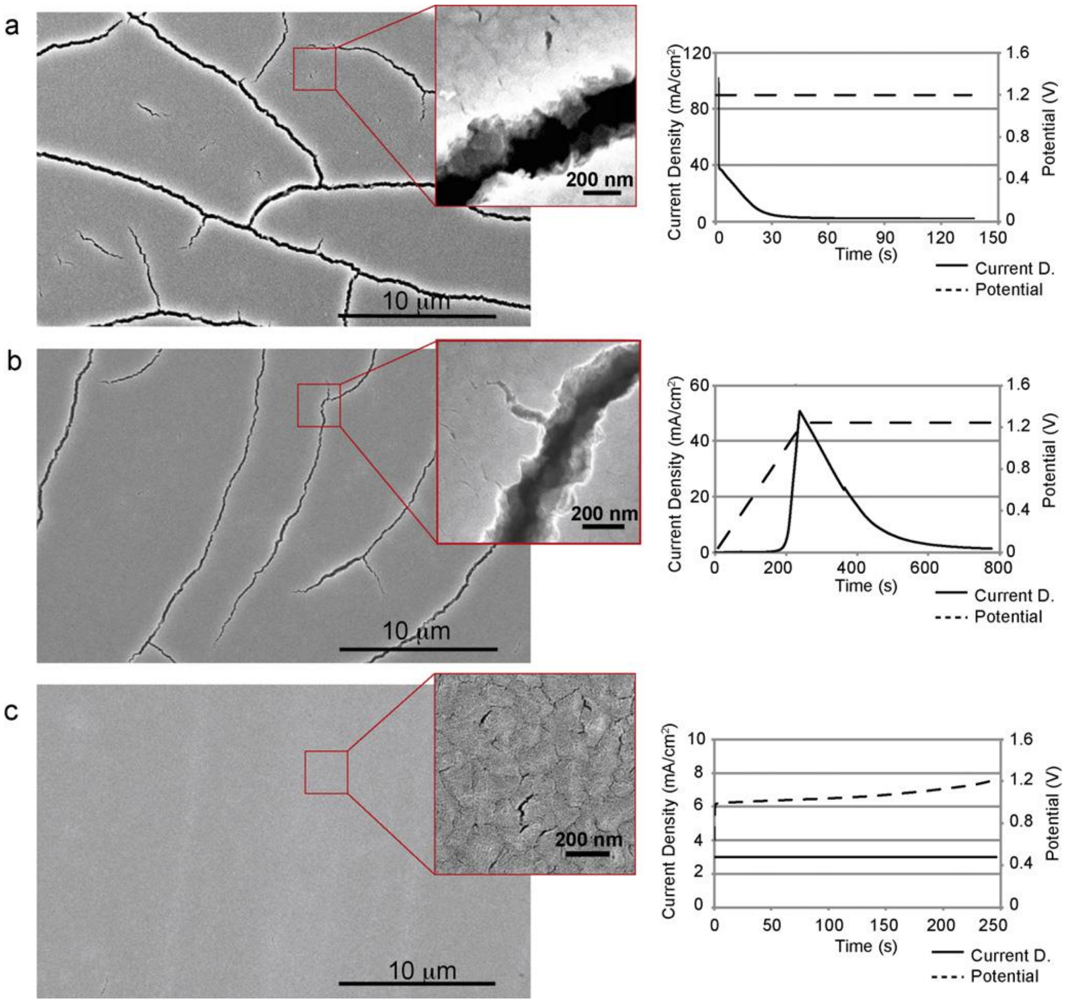

**Figure 2-8** Np-Au structures with their dealloying potential and current records. (a) potentiostatic method with stepped potential; (b) potentiostatic method with ramped potential; and, (c) galvanostatic method with constant current density of 3mA/cm$^2$ (adapted from Okman and Kysar Copyright 2011 Elsevier[35]).

Post treatments are conducted to further control of microstructure in np-metals. Post-dealloying can lower the residual amount of Ag. Residual Ag element in np-Au is associated with chemical activity and mechanical properties. Even if residual Ag is removed as much as they can, surface diffusion of Au could be occurred in nitric acid causing coarsening of ligament. Ligament coarsening can be occurred up to microscales by post heat treatment (annealing) [37-38]. Relation between ligament size and annealing temperature can be described by the equation

$$k \cdot t = \exp(-\frac{Q}{RT})$$

where $k$ is characteristic ligament size, $t$ is time, $Q$ is activation energy of coarsening, $R$ is Boltzmann constant and $T$ is annealing temperature. Previous results show relation between ligament size and annealing temperature and activation energy for coarsening of 34.1 kJ/mol for 2 hours annealing[17]. This value is very close to surface diffusion of Au and indicates that ligament coarsening is accomplished by surface diffusion. Also, 3D reconstruction by FIB-tomography of coarsened np-Au has demonstrated np-Au coarsening was carried out in self-similar manner where ligament size distribution, connectivity and surface-to-volume ratio is in similar trend.

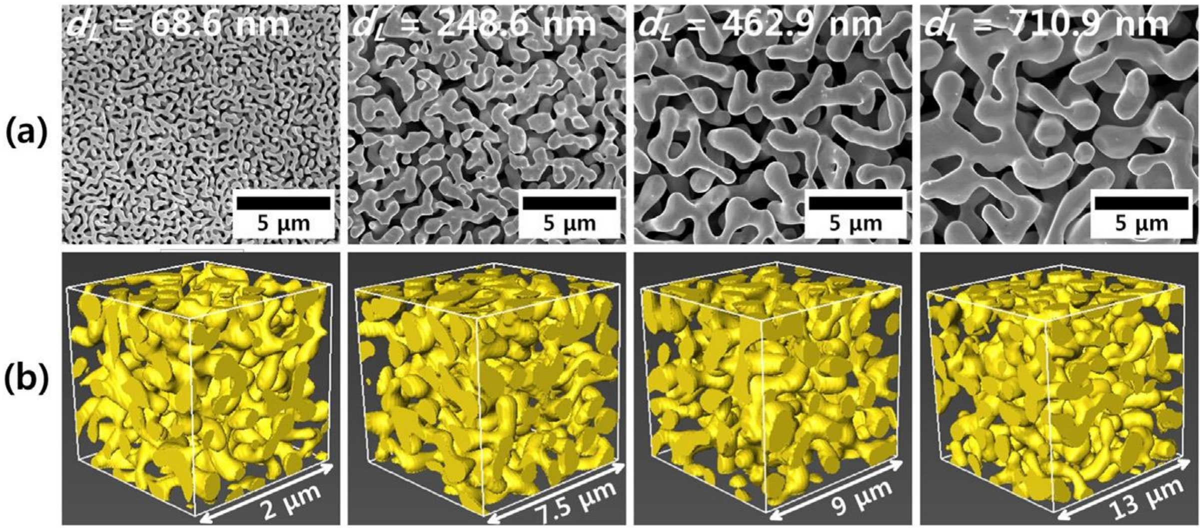

**Figure 2-9** Morphology evolution during coarsening by heat treatment. (a) SEM and (b) 3D reconstructed images of np-Au samples coarsened under different temperature (adapted from Jeon et al., Copyright 2017 Elsevier[17]).

## 2.2 Mechanical properties of np-Au

### 2.2.1 Effect of relative density

Np-metals made by corrosive dealloying are open-cell structure with over 50% porosity in volume. Figure 2-10 shows typical compressive stress-strain curve for open-cell material. It shows three deformation stage; linear elastic region; plateau region by plastic collapse and; densification region. After linear elastic region, plastic collapse is occurred without large increase in stress because it is proceeded by elastic buckling, shearing and fracture of ligaments with pore closing. Densification region appear when pore volume could be shrunk anymore.

Relative density, ratio of density of cellular material ($\rho^*$) to dense solid material ($\rho_s$), is an important factor to mechanical properties of cellular material[39]. In the book of Gibson and Ashby, yield strength($\sigma^*$) and elastic modulus($E^*$) of open-cell material have been described by the relation with relative density of foam ($\rho^*/\rho_s$) as

$$\sigma^* = C_2\sigma_s\left(\frac{\rho^*}{\rho_s}\right)^{1.5} \qquad (2\text{-}1)$$

$$E^* = C_1E_s\left(\frac{\rho^*}{\rho_s}\right)^{2} \qquad (2\text{-}2)$$

where $\sigma_s$ and $E_s$ is yield strength and elastic modulus of solid material, $C_1$ and $C_2$ is constant. By these equations, mechanical properties of foam could be expected from solid material. However, this Gibson-Ashby model has been well fitted for cellular material with relative density less than 0.1 and smaller ligament size than pore size. Np-metals have relative density of 0.2 ~ 0.5 and ligament size is similar to cell size. Therefore, new scaling equations for describing np-metal have been studied by many researchers.

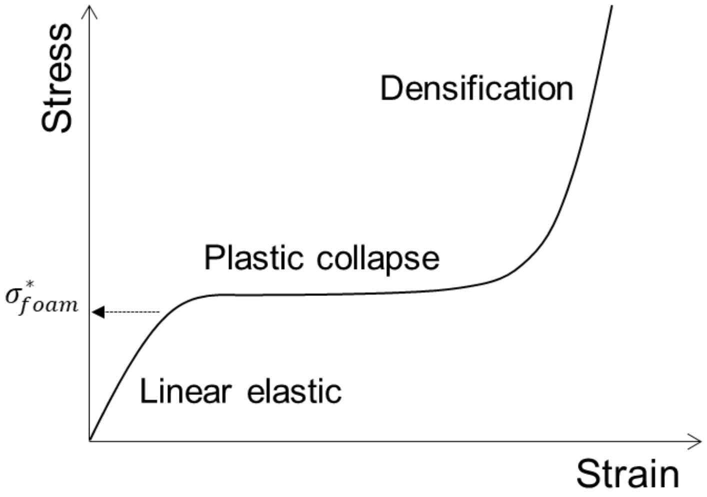

**Figure 2-10** Compressive stress-strain behavior of general open cell structured porous materials.

### 2.2.2 Effect of ligament size

Ligament size effect has been firstly illustrated by flexural test that brittle to ductile transition is occurred by increasing ligament size. As nanomechanical testing methods have been developed, mechanical properties of np-metals have been investigated by nanomechanical testing such as nanoindentation and nanopillar compression. Nanoindentation is a simple and easy technique to measure hardness and elastic modulus from indentation force versus depth curve obtained by indenting surface of materials with hard diamond tip. Previous researches have examined hardness and elastic modulus of np-Au with relative density of 0.25 to 0.42 and ligament size of 10 to 900 nm and have revealed that hardness is increased by decreasing ligament size even if np-Au samples have same relative density[11-12, 40].

When plastic constraint factor, Ψ, is assumed to be 1 in Tabor equation, $H = \Psi\sigma_y$, for cellular material, yield strength and elastic modulus of np-Au is in range of 15 to 240 MPa and 7 to 40 GPa, whose yield strength is higher than annealed gold of 2 MPa and cold-rolled gold of 200 MPa. Estimated yield strength of np-Au with same relative density by G-A equation is in range of 7.5 to 16 MPa which is much lower than yield strength obtained by nanoindentation. Therefore, scaling equation considering ligament size effect has been suggested[12].

$$\sigma^* = C_s\left[\sigma_0 + kL^{-\frac{1}{2}}\right]\left(\frac{\rho^*}{\rho_s}\right)^{3/2} \qquad (2\text{-}3)$$

Where $\sigma^*$ is yield strength of np-Au, $C_s$ is constant, $\sigma_0$ is yield strength of bulk gold, $k$ is Hall-Petch coefficient, $L$ is ligament size and $\rho^*/\rho_s$ is relative density of np-Au.

Recent research has suggested revised scaling equation for np-Au considering ligament size effect in nanoindentation, compression and tension and size effect in nanopillar compression[41]. Based on empirical fitting, constant $C_s$, size effect exponents for ligament size and scaling exponent for relative density is obtained as below equation,

$$\sigma^* = 1.939\sigma_s\left(\frac{\rho^*}{\rho_s}\right)^{2.618} \text{ with } \sigma_s = 0.0328l^{-0.551}. \qquad (2\text{-}4)$$

Ligament size effect on strength of np-Au can be explained by dislocation starvation theory in line with size effect in nanopillar compression. Np-Au is composed with interconnected nanowire network in three-dimensional way, thus existence probability of dislocation source decreases with decreasing diameter of ligament.

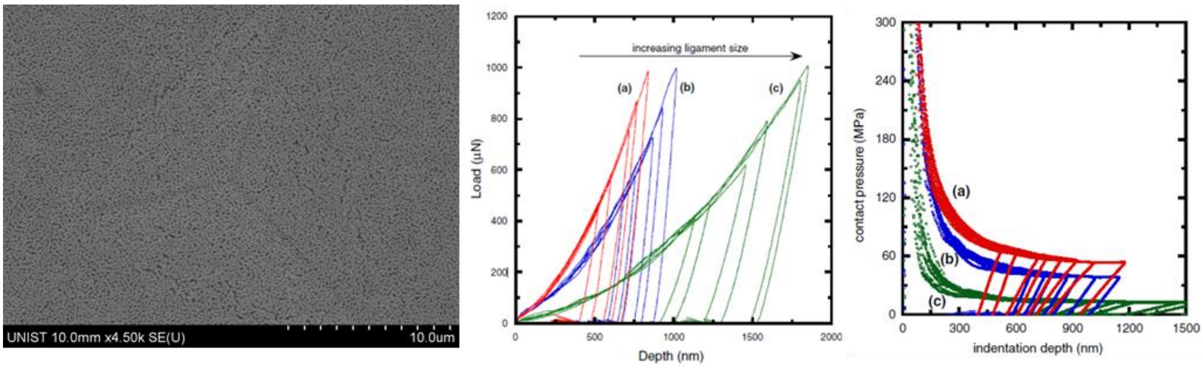

**Figure 2-11** SEM image of residual indent after sharp tip indentation and force-indentation depth and hardness-indentation depth curve on np-Au samples with different ligament size; (a) 60 nm; (b) 160 nm; (c) 480 nm (adapted from Hodge et al., Copyright 2007 Elsevier[12]).

Rare dislocation source in ligament leads to strength of individual ligament obtaining theoretical strength of gold and change in carrier of deformation from use of internal dislocation to surface nucleation of dislocation. Figure 2-13 shows that pre-existing dislocations (indicated in white arrows) in ligament is moved to node and pore closing is occurred by indentation[42].

One of important aspects of mechanical characteristics for np-metal is tension-compression asymmetry originated from nanoporous structure. Pores are closed during compression, on the other hand, pores are opened and enlarged during tension. Also, deformation mode in compression is mainly bending and torsion of ligament, whereas tension of ligament aligned with tensile direction is main deformation mode in tension. Pore opening during tension causes brittle fracture of np-Au. Figure 2-14 shows tensile behavior of np-Au that catastrophic brittle failure is occurred right after linear elasticity even though each ligament at fracture surface are ruptured by plastic deformation and necking. Furthermore, plastic deformation is localized at ligaments on outermost fracture surface. This means that crack propagates very fast when the weakest ligament is fractured. Therefore, some research groups have been suggested techniques for alleviating brittle fracture of np-Au such as coating ligament surface with polymers.

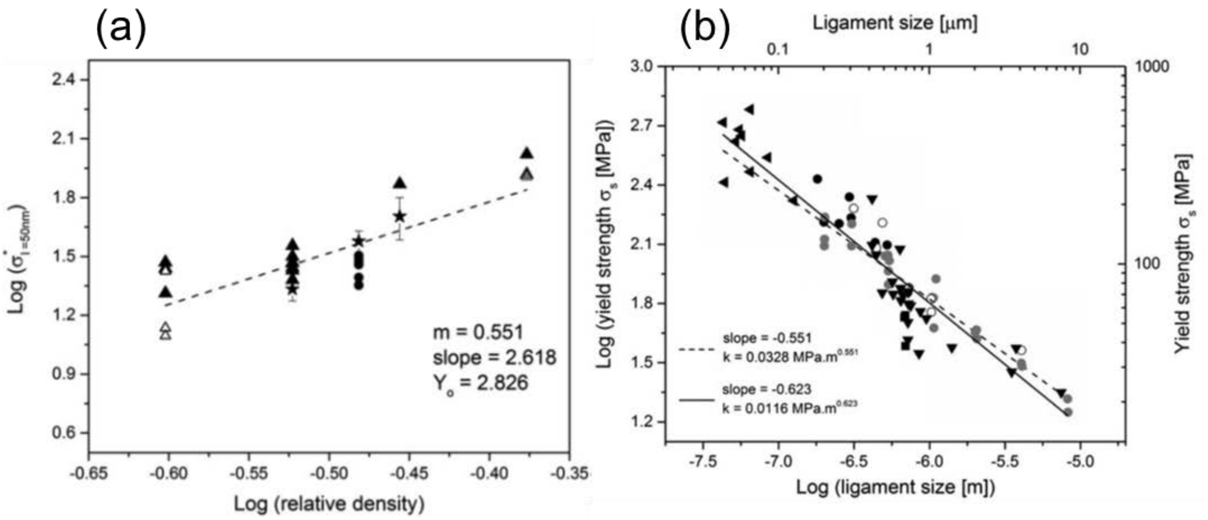

**Figure 2-12** Scaling relation of (a) strength-relative density and (b) strength-ligament size (adapted from Briot and Balk Copyright 2015 Taylor & Francis[41].)

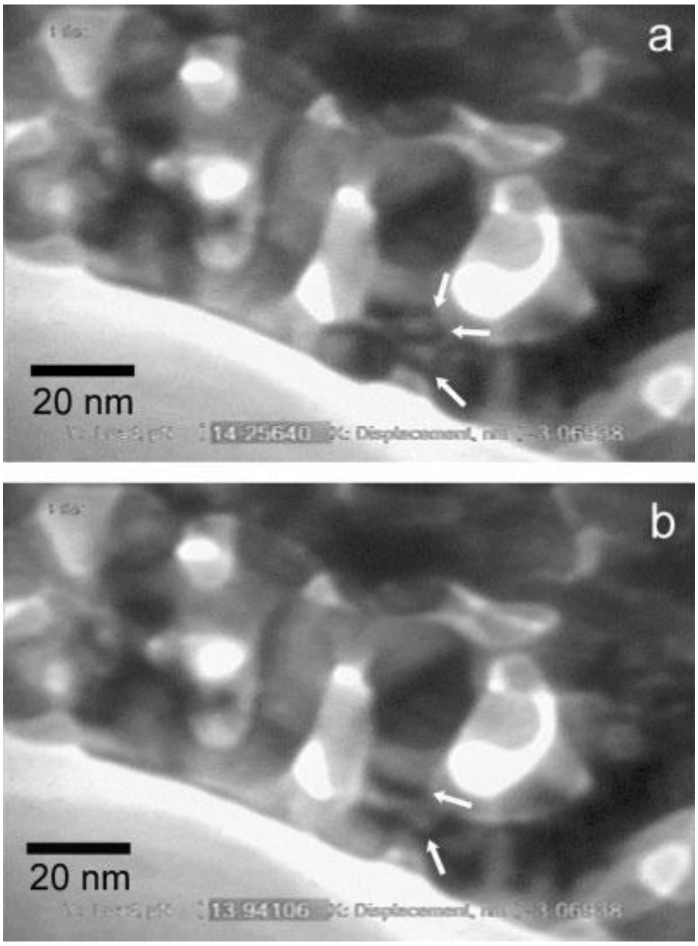

**Figure 2-13** Dislocation motion during nanoindentation on np-Au. Dislocations in ligament (indicated by arrows) move to ligament junction by indentation (adapted by Sun et al., Copyright 2009 John Wiley and Sons[43]).

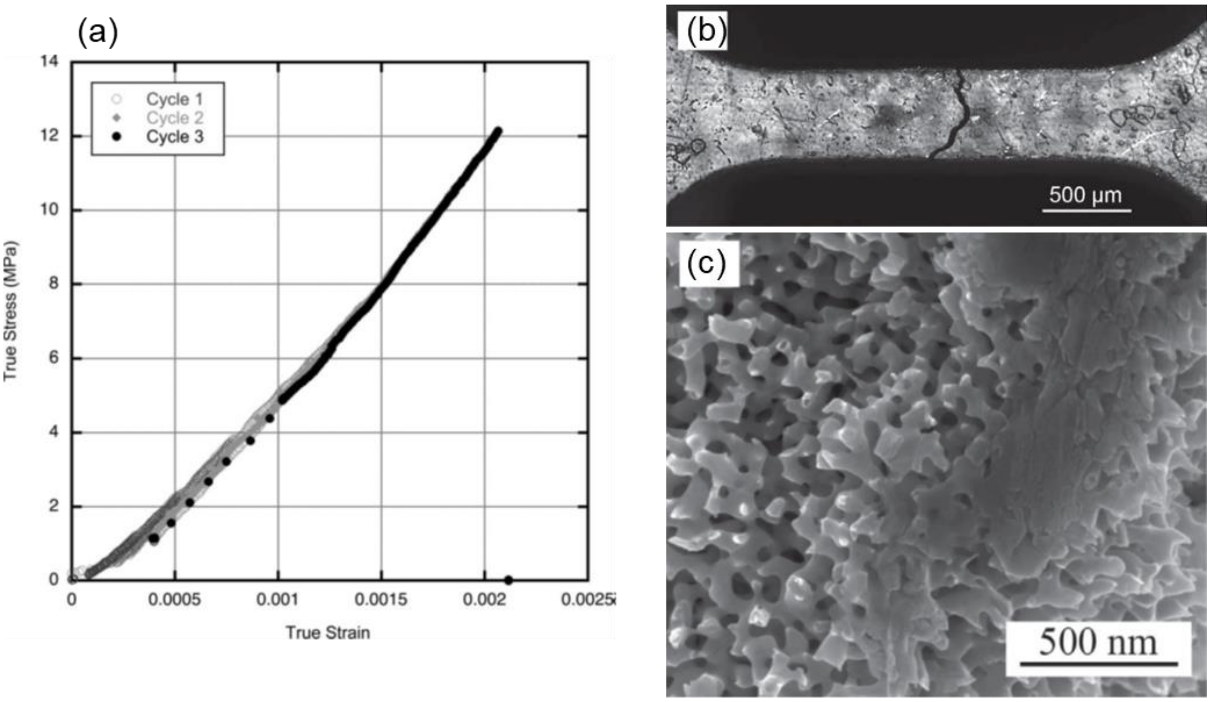

**Figure 2-14 (**a) Tensile stress-strain curve for np-Au. (b) Fractography of np-Au tensile specimen and (c) fracture surface (adapted by Hodge and Balk, Copyright 2012 Royal Society of Chemistry[44]).

# 3. Mechanical Properties of Np-Au Depending on External Microstructures

## 3.1 Indentation Size Effect of Np-Au in Sharp Tip Indentation

Recently, mechanical characterization in nanoscale material have been explored significantly because of decrease in size of constituent materials by miniaturization and integration of devices. Among various nanomechanical tests, nanoindentation is a powerful and nondestructive technique to determine mechanical behavior of materials such as indentation hardness, elastic modulus, residual stress and so on. In the case of solid materials, hardness is increased as indentation depth decreases under critical depth, which is called indentation size effect. When hardness is overestimated at shallow indentation, it is hard to affirm that measured hardness is representative hardness value of the material. So, there must be researches for mechanism and estimation of indentation size effect in order to obtain exact mechanical properties.

In general, indentation size effect in solid materials are explained by geometrically necessary dislocation. When indentation depth is very low, affected volume by indentation elastically and plastically is too small to have dislocation source inside, thus new dislocations should be nucleated to carry out deformation. The nucleated dislocations to carry deformation at low indentation depth are called as geometrically necessary dislocations and they requires higher stress because interaction volume is almost defect-free at low depth near surface. As indentation is proceeded into deeper volume, pre-existing dislocation sources are activated by indentation force. These pre-existing dislocations are called as statistically stored dislocations. Therefore, strain gradient generated during indentation causes indentation size effect of solid materials.

Indentation size effect could be explained with numerical explanation [45]. In geometrically self-similar sharp tip indentation, total length of geometrically necessary dislocation loops is defined as $\lambda = \pi h_p a/b$, where angle between sample surface and tip surface is $\theta$, residual plastic depth is $h_p$(=$h$), contact radius is $a$ and $b$ is Burger's vector. As interacting hemisphere volume by indentation of $h_p$ is $V = 2\pi a^3/3$, density of geometrically necessary dislocations in hemisphere is $\rho_G = \frac{\lambda}{V} = \frac{3}{2bh_p}\tan^2\theta$ where $\tan\theta = \frac{h_p}{a}$. Based on Taylor hardening model, shear strength, $\tau$, is described as function of total dislocation density, $\rho_T$, as $\tau = \alpha\mu b\sqrt{\rho_T}$ where $\mu$ is shear modulus and $\alpha$ is geometric constant. Total dislocation density is summation of statistically stored dislocation, $\rho_S$, and geometrically necessary dislocation, $\rho_G$, as described by $\rho_T = \bar{r}\rho_G + \rho_S$ where $\bar{r}$ is Nye factor. By the relation between flow stress and shear strength, $\sigma = \sqrt{3}\tau$, and Tabor factor, indentation hardness, $H$, is described by $H = 3\sqrt{3}\alpha\mu b\sqrt{\rho_T}$. Therefore, indentation size effect is represented by equation $H/H_0 = \sqrt{1 + h^*/h}$ where

*H* is indentation hardness, *H<sub>0</sub>* is macroscopic hardness $H_0 = 3\sqrt{3}\alpha\mu b\sqrt{\rho_s}$, $h$ is indentation depth and $h^*$ is characteristic length $h^* = 3\bar{r}\tan^2\theta/2b\rho_s$. The macroscopic hardness $H_0$ was found to increase and the indentation size effect characteristic length $h^*$ to decrease with increasing plastic pre-strain since initial statistically stored dislocation density is increased by pre-straining.

Indentation hardness of np-Au is increased with decreasing ligament size and decreasing indentation depth. Although there have been several studies about nanoindentation on np-Au, mechanism for indentation size effect in np-Au have not been studied. On the other hand, np-metals have a lot of free volume and surface area which make dislocation can be annihilated easily without multiplication or interaction. So, indentation size effect in np-metals cannot be explained by strain gradient and geometrically necessary dislocation in solid materials.

In this chapter, compressive and shear tests and nanoindentation on np-Au with different ligament size is performed to figure out mechanism for indentation size effect of np-Au. Also, nanomechanical modeling is suggested for numerical description of correlation between indentation size effect and ligament size effect.

### 3.1.1 Nanomechanical Modeling

I developed nanomechanics model to investigate indentation size effect behavior of np-Au using sharp Berkovich indenter regarding with ligament size. The sharp indenter is assumed to be serial stacking of infinite thin disk-shape flat punches (Fig. 3-1). While nanoindentation progresses to indentation depth of $\delta h$, the circumference area, $2\pi(r+\delta r)\delta h$, anew penetrates np-Au by shear force inducing plastic collapse. The volume of np-Au in touch with bottom penetrates by $\delta h$ in the loading direction with bottom area of $\pi r^2$ that is the summation of segment $\pi(r+\delta r)^2 - \pi r^2$ from 0 to r with respect to r :

$$\sum_{n=0}^{r}[\pi(n+\delta r)^2 - \pi n^2] = \sum_{n=0}^{r}[\pi \cdot 2n\delta r] = \pi\int_0^r 2r dr = \pi r^2. \qquad (3\text{-}1)$$

The unit length scale for plastic collapse of np-Au along the loading direction is assumed to be one cell size *D*, which consists of single ligament and single pore, and cell size is briefly assumed to be three times the ligament size 3*l* from measurement of average pore size. The relation between *D* and spacing of individual steps, *s*, is construed as

$$tan\,\theta = \frac{h}{r} = \frac{\delta h}{\delta r} = \frac{D}{s}, \quad s = \frac{Dr}{h}, \qquad (3\text{-}2)$$

where $\theta$ is a contact angle between surface of sample and surface of indenter tip (19.7° for a Berkovich indenter) and $r$ and $h$ are contact radius and indentation depth, respectively, as shown in Fig. 3-1. The work introduced by nanoindentation, $\underline{dW}$[46] by indentation depth of $\delta h$ is expressed by

$$dW = \left(w_{\text{comp}} + w_{\text{shear}}\right)\frac{dr}{s}. \tag{3-3}$$

The work induced by shear and compressive forces, $w_{comp}$ and $w_{shear}$, described by

$$w_{\text{comp}} = \sigma \cdot \pi r^2 \cdot D, \tag{3-4a}$$

$$w_{\text{shear}} = \tau \cdot 2\pi r \cdot D \cdot kD, \tag{3-4b}$$

where $k$ is a proportional constant which means the number of cells deformed by shear force at the circumferential area $2\pi r \cdot D$ along loading direction when indentation depth increases by $D$[47-48]. $\sigma$ and $\tau$ in Eqs. (3-4a) and (3-4b) are considered with the intrinsic irregularity of np-Au, not for simplified nanoporous structure in simple stress modes[48]. The indentation force $P$ can be construed as

$$P = \frac{dW}{dh} = \sigma \cdot \pi r^2 + \tau \cdot 2\pi r \cdot kD. \tag{3-5}$$

Relation between indentation hardness $H$ and compressive strength $\sigma$ can be described with plastic constraint factor $\Psi$ as $H = \Psi\sigma$. By this relation, $\sigma$ in Eq. (3-5) can be replaced by $(1/\Psi)H_0$ since $\sigma$ is independent of indentation depth. Dividing both sides of Eq. (3-5) with $\sigma \cdot \pi r^2$ yields the indentation size effect model for np-Au.

$$\frac{H}{H_0} = \frac{1}{\Psi}\left(1 + \frac{K}{h/D}\right), \tag{3-6}$$

where

$$K = 2\tan\theta \cdot \frac{\tau}{\sigma} \cdot k. \tag{3-7}$$

$H$ and $H_0$ are the hardness and macroscopic hardness which is convergent with the hardness value at sufficient indentation depth, respectively. $\Psi$ is the plastic constraint factor of np-Au, $K$ is the characteristic length for the indentation size effect for np-Au, and $h/D$ is the indentation depth normalized by cell size. The Eq. (3-6) is an inverse function of indentation depth similar to the Nix-Gao model for solid materials, which is $\frac{H}{H_0} = \sqrt{1 + \frac{h*}{h}}$, where $h*$ is the indentation size effect characteristic length for solid materials[45].

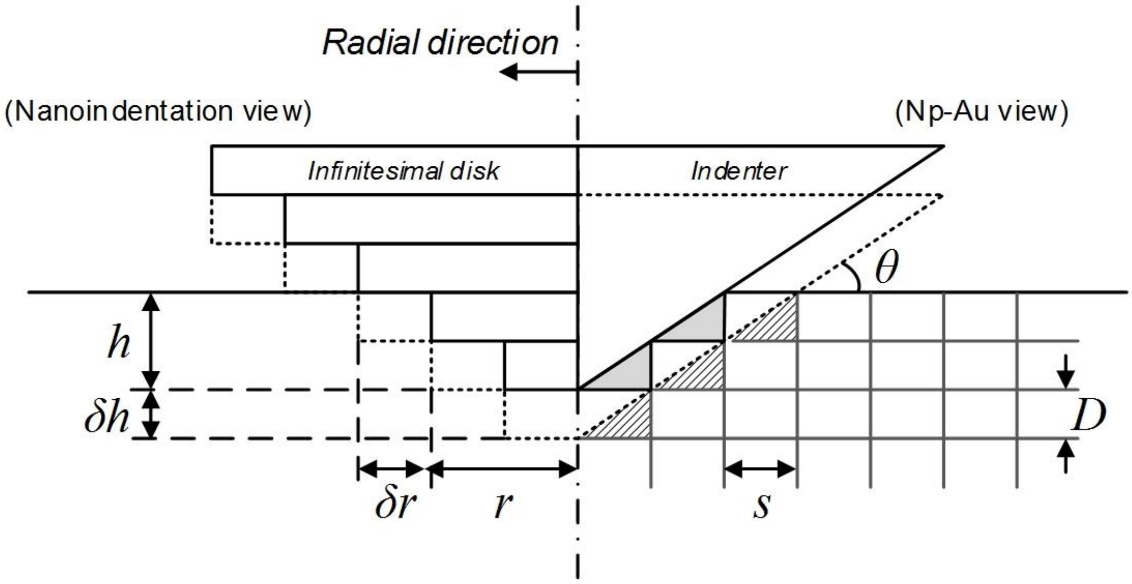

**Figure 3-1** Nanomechanical model for sharp tip nanoindentation on np-material (adapted from Kim et al., Copyright 2017 Elsevier[49]).

In the suggested indentation size effect model for np-Au, macroscopic hardness, $H_0$, is dependent on $\Psi$. At the beginning level of research related with mechanical behavior of np-Au, plastic constraint factor $\Psi$ was supposed to be 1 as porous materials with very low relative density[12, 39]. Recent studies found that np-Au has plastic constraint factor in range of 2.65 to 3 similar to solid metals by comparing tensile and compressive tests[41, 50-52]. The characteristic length for the indentation size effect for np-Au, $K$ in Eq. (6) is independent of value of $\Psi$.

Self-similarity in np-Au samples obtained from dealloying and post-heat treatment is an important factor to suggest universal indentation size effect model for np-Au with different ligament structure. Np-Au has random irregular ligament structure, thus mechanical properties are altered by connectivity and curvature evolution in np-Au. In this research, nanoporous structure is assumed to be self-similar. Geometrically self-similarity of np-Au is still controversial. Self-similarity in np-Au has been investigated by several researchers using destructive and non-destructive three-dimensional reconstruction, tomography and numerical analysis[17, 37, 53-56]. Kertis *et al*. demonstrated the evolution of self-similar structure of np-Au using SEM analysis with ligament sizes from few nanometer to micrometer-scale obtained by dealloying and annealing treatment[37]. Hu *et al*. demonstrated that ligament connectivity is self-similar in coarsened np-Au with genus parameter[53]. Chen-Wiegart *et al*. measured three-dimensional structures of np-Au samples by X-ray tomographic reconstruction[54]. The interfacial normal distribution(IND) and interfacial shape distribution (ISD) analysis suggested that distributions of surface orientation and scaled surface curvature were not self-similar during thermal coarsening. Mechanical self-similarity of np-Au was also discussed with regard to network connectivity[55]. The connectivity of each ligament was explained by introducing an effective relative density, which was defined as a ratio of measured elastic moduli from compressive testing and elastic moduli expected by Gibson-Ashby model. According to change in effective density, the network connectivity of np-Au samples was gradually increased by increasing ligament size above ligament size of 150 nm due to volume contraction. Ziehmer *et al*. conducted three-dimensional FIB-based tomography for np-Au samples with ligament size of 25 nm in as-dealloyed sample to 420 nm in annealed at 300°C and concluded that coarsened np-Au might be self-similar[56]. Jeon *et al*., also conducted 3D reconstruction of thermally-coarsened np-Au, and analyzed evolution of nanoporous structure during thermal coarsening[17]. In their research, it was found out that np-Au coarsens in self-similar way in terms of distribution of ligament size, surface-to-volume ratio which means surface roughness of ligament, and scaled connectivity density. In this chapter, self-similarity of np-Au is assumed consistent during coarsening by annealing to simplify the theoretical approach.

### 3.1.2 Experimental Procedure and Results

#### 3.1.2.1 Experimental Procedure

Precursor alloy of Au 30 at.% and Ag 70 at.% were prepared from Au (99.99%) and Ag (99.99%) pellets and liquefied together at high temperature by plasma arc-melting in an Ar environment. Alloyed precursor ingot was homogenized at 800°C for 72 hours in a tube furnace under $N_2$ environment and cooled to room temperature in the furnace. Precursor ingot was cut and pressed to make 1 mm-thick plate-like shape. Top and bottom sides of the precursor plate were polished down to 0.25 μm diamond suspension. The samples were annealed in a tube furnace under $N_2$ environment at 800°C for 24 hours to homogenize and to release residual stress in precursor alloy generated by mechanical machining and polishing.

The np-Au samples were prepared from annealed precursor $Au_{30}Ag_{70}$ alloys by free-corrosion dealloying. Dealloying process was executed in diluted nitric acid under different conditions in order to control ligament size: in 35% concentrated nitric acid at 20°C for 72 hours, producing ligament size ($l$) 26 nm (hereafter called sample #1 ($l$ = 26 nm)), in 35% concentrated nitric acid at 50°C for 72 hours, producing ligament size 73 nm (hereafter called sample #2 ($l$ = 73 nm)), and 35% concentrated nitric acid at 80°C for 72 hours, producing ligament size 127 nm (hereafter called sample #3 ($l$ = 127 nm)). These dealloying conditions were selected to get different ligament sizes based on the previous work[57]. Through annealing of sample #3 ($l$ = 127 nm) at 600°C for 2 hours, ligament size 630 nm were obtained (hereafter called sample #4 ($l$ = 630 nm)). Each np-Au samples were examined in field emission scanning electron microscopy (FE-SEM, FEI Nanonova 230). Average ligament sizes were measured from thickness of the thinnest necks at the ligament center from at least 100 measurements in SEM images. Surface morphology of four np-Au samples of ligament sizes 26 (±4.0), 73 (±8.8), 127 (±12.8), 630 (±61.4) nm is presented in Figs. 3-2(a)−(d).

Nanoindentations using sharp Berkovich indenter were performed on all four samples. Reproducible force versus indentation depth curves were obtained from over 12 tests. The maximum indentation depth in each sample was determined to be 40 times the size of the ligament, where cell size $D$ consists of single ligament and single adjacent pore, assuming a ligament size of three, $3l$; that is, intended maximum indentation depth = $13.3D = 40l$. The volume indented into maximum indentation depth contains 27000 cells approximately, and convergent trend in hardness was confirmed with increasing indentation depth as far as maximum indentation depth of $40l$. Nanoindentations were carried out using continuous stiffness measurement (CSM) by XP module with load capacity 500 and DCM II module with load capacity 30 mN in a Nanoindenter G200 (KLA). All nanoindentation tests were conducted at constant indentation strain rate 0.05 $s^{-1}$, with allowable thermal drift limit of 0.05 nm/s. Relative densities of the np-Au samples were calculated from direct measurements of external volume and weight. Np-Au cuboids of dimensions 0.8 mm × 0.8 mm × 1.2 mm for testing in both uniaxial compression and pure shear were prepared. Uniaxial compressive tests and pure shear tests were performed at constant displacement rate of 0.05 $s^{-1}$ using a micro universal testing machine (Instron 5948) using custom-designed jigs. For each sample, reproducible force-displacement curves more than 4 time were obtained from compression and shear tests.

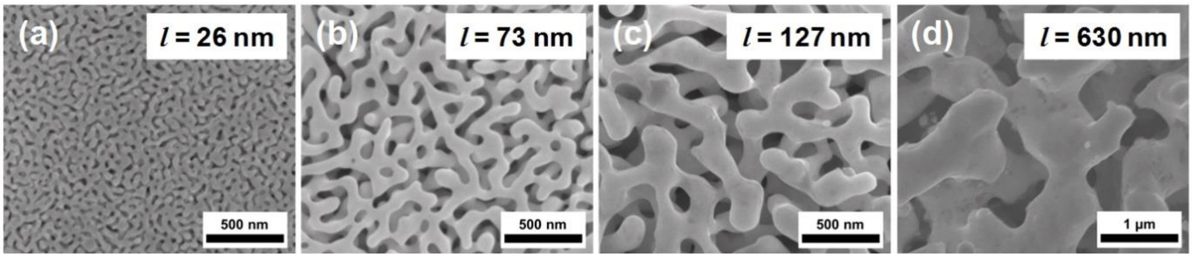

**Figure 3-2** Surface morphology of np-Au samples from different dealloying conditions and annealing process (adapted from Kim et al., Copyright 2017 Elsevier[49]).

#### 3.1.2.2 Nanoindentation Results

Typical indentation force-depth curves for np-Au samples are shown in Fig. 3-3(a)-(d) and typical indentation hardness versus indentation depth for four np-Au samples are shown in Fig.3-3(e)-(h). Figure 3-3(a)-(d) show that higher force is required to penetrate certain indentation depth as ligament size decreases. That is conforming to previous researches that np-Au with smaller ligament size has higher indentation hardness[12]. Figure 3-3(e)-(h) show that hardness increases by decreasing indentation depth for all np-Au samples, i.e. an indentation size effect in np-Au. Macroscopic hardness $H_0$ is convergent hardness value as increasing indentation depth. The macroscopic hardness for np-Au samples were measured by averaging hardness values between indentation depths $30l$ and $40l$ where $40l$ is the maximum indentation depth; 106.1 (±4.52) MPa for sample #1 ($l$ = 26 nm), 55.8 (±1.62) MPa for sample #2 ($l$ = 73 nm), 26.5 (±1.34) MPa for sample #3 ($l$ = 127 nm), and 3.0 (±0.11) MPa for sample #4 ($l$ = 630 nm).

To compare trend in indentation size effect for np-Au with different ligament size, normalized hardness ($H/H_0$) against normalized indentation depth ($h/D$) for np-Au samples relation are shown in Fig. 3-4. By Fig. 3-4, it revealed that trends of indentation size effect for np-Au samples #1 ($l$ = 26 nm), #2 ($l$ = 73 nm) and #3 ($l$ = 126 nm) are almost identical, whereas sample #4($l$ = 630 nm) shows enhanced indentation size effect above the other three. These results mean that np-Au obviously shows indentation size effect with ligament size of 26 nm to 630 nm and their trend of indentation size effect has transition depending on ligament size since indentation size effect curve for np-Au with coarsened ligament size doesn’t overlap to those of np-Au with smaller ligament size.

Indentation hardness versus indentation depth curves were fitted with Eq. (3-6) to examine consistency to np-Au samples and Fig. 3-5(a)-(d) show that Eq. (3-6) successfully explains the typical relation of hardness vs indentation depth for all four samples. The characteristic constant $K$ in Eq. (3-6) is 0.52 (±0.15) for sample #1 ($l$ = 26 nm), 0.54 (±0.20) for sample #2 ($l$ = 73 nm), 0.52 (±0.30) for sample #3 ($l$ = 126 nm), and 1.86 (±0.47) for sample #4 ($l$ = 630 nm), respectively. Measured $K$ values indicates that np-Au samples #1-#3 have almost identical indentation size effect propensity, on the other hand, indentation size effect behavior for sample #4 is increased over the other three as shown in Fig. 3-4.

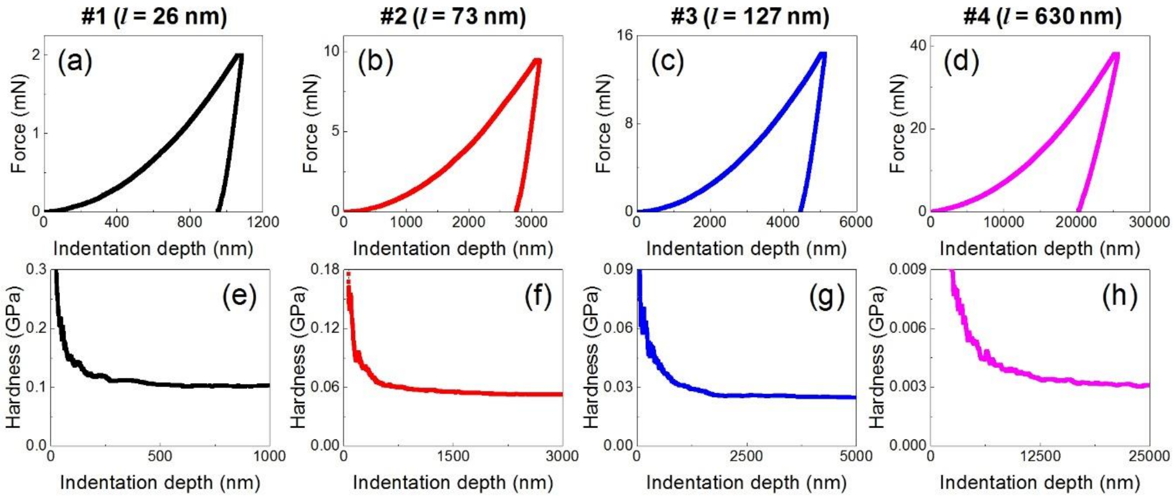

**Figure 3-3** (a)-(d) Force-indentation depth curves and (e)-(h) hardness-indentation depth curves on np-Au samples with different ligament sizes (adapted from Kim et al., Copyright 2017 Elsevier[49]).

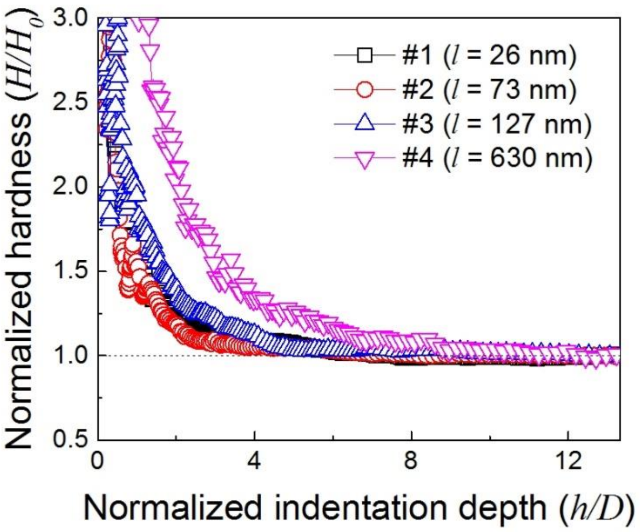

**Figure 3-4** Normalized hardness by macroscopic hardness versus normalized indentation depth by cell size curves of np-Au samples (adapted from Kim et al., Copyright 2017 Elsevier[49]).

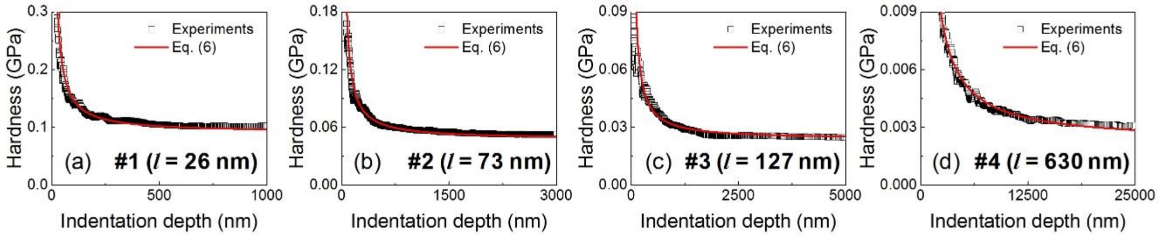

**Figure 3-5** Typical hardness-indentation depth curves and fitted curves of np-Au samples (adapted from Kim et al., Copyright 2017 Elsevier[49]).

A parameter in Eq. (3-7) is the ratio of shear strength over compressive strengths, $\tau/\sigma,$ of np-Au which need to be measured. To get this strength ratio, uniaxial compressive tests and pure shear tests were performed for np-Au samples. Figs. 3-6(a) show typical compressive stress to compressive strain curves and Fig. 3-6(b) is enlarged graph of (a) at low strain and low stress range. In general, compressive stress-strain curves for np-Au samples show similar trend with compressive stress-strain behavior of cellular materials with three stages: linear elastic, plastic collapse, and densification[39]. Compressive yield strengths, $\sigma$ in Eqs. (3-4a) and (3-7), were determined by 0.2% offset method. Measured $\sigma$ values were 122.6 (±1.16) MPa for sample #1 ($l$ = 26nm), 41.5 (±4.30) MPa for sample #2 ($l$ = 73nm), 22.9 (±0.96) MPa for sample #3 ($l$ = 126nm), and 5.3 (±0.05) MPa for sample #4 ($l$ = 630 nm). In Fig. 3-6(c), the relation between compressive strength and ligament size is presented in log-log scale. There is linear scaling relation in four np-Au samples about ligament size with slope of 0.98 where slope is size effect exponent, $m_{comp}$ in $\sigma = l^{-m_{comp}}$.

Typical pure shear stress to shear strain curves of np-Au samples are presented in Figs. 3-7(a) and (b). Samples #1~#3 show almost linear elastic deformation and catastrophic fracture. On the contrary, sample #4 ($l$ = 630 nm) shows continuous strain-hardening after linear elastic region. And strain-softening with increasing shear strain after shear strain of 0.18 as partial cracks are generated. Shear strength $\tau$ in Eqs. (3-4a) and (3-7) are considered as measured shear yield strength : 52.0 (±10.56) MPa for sample #1 ($l$ = 26 nm), 7.6 (±1.36) MPa for sample #2 ($l$ = 73nm), and 1.5 (±0.34) MPa for sample #3 ($l$ = 126nm), respectively. The shear yield strength of sample #4 ($l$ = 630nm) determined by the 0.2% offset method is 0.3 (±0.06) MPa. The shear yield strength also shows strong ligament-size effect tendency with slope, which is size effect exponent for shear mode, $m_{shear}$, is calculated as 1.60 in $\sigma = l^{-m_{shear}}$., as seen in Fig. 3-7(c).

For samples #1~#3, deformation is concentrated at thinnest neck of ligament and cross-sectional area of ligament decreases during shear deformation of np-Au while nucleated dislocations from ligament surfaces are pile-up at thicker ligament junction. By necking of ligament, given stress is larger than load-carrying ability of ligament causing catastrophic failure in np-Au.

The shear stress-strain curve for sample #4 ($l$ = 630nm) shows strain-hardening behavior that is ductile behavior on the contrary to other three samples. This indicates that there exist a transition in shear deformation mechanism from brittle to ductile between ligament size 126 nm (sample #3) and 630 nm (sample #4). In line with our results of ligament-size-dependent brittle to ductile transition in shear testing, it has been reported that transition of ductile and brittle fracture of np-Au is shown depending on ligament size in flexural testing[58].

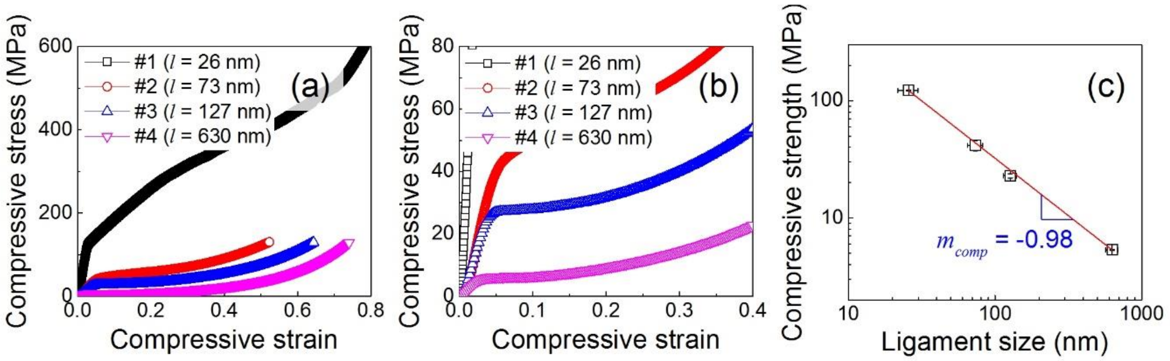

**Figure 3-6** Uniaxial compressive stress-strain curves of np-Au samples and compressive yield strength and ligament size relation (adapted from Kim et al., Copyright 2017 Elsevier[49]).

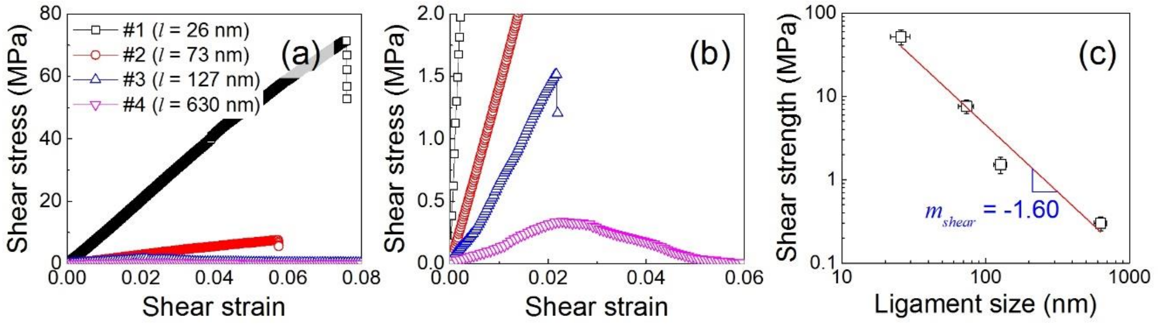

**Figure 3-7** Shear stress-strain curves of np-Au samples and shear strength and ligament size relation (adapted from Kim et al., Copyright 2017 Elsevier[49]).

Fig. 3-8(a) shows the ratio of shear strength to compressive strength, $\tau/\sigma$, as a function of ligament size. The ratio $\tau/\sigma$ of four samples are less than one, in other words, shear strength is lower than compressive strength. Np-Au has random irregular nanoporous structure containing many dangling ligaments. During compression, these dangling ligaments might contact and support nanoporous structure additionally from external compressive loading inducing strengthening. On the other hand, ligaments are separated and become far from neighbors in shear testing and could not enhance strength of np-Au. This difference between pore closing during compression and pore opening during shear deformation could be attributed to that the ratio $\tau/\sigma$ is less than one. This asymmetry in strength have been noticed by some researchers. Balk *et al*., conducted milli-meter scale tension and compression test for polycrystalline np-Au with ligament size about 30 nm and reported a compressive strength of 15.5 MPa and a tensile strength of 11.5 MPa whose ratio of tensile strength to compressive strength was 0.74[59]. In tensile loading, pore opening mode is dominated while many separated neighboring ligaments are further separated without any strengthening role, and grain boundaries might also weaken tensile strength of np-Au[15]. The ratio of tensile to compressive strength could be less than one for the same reason. Whereas, it has been presented that single-crystalline np-Au with ligament size of 55.9 nm have a compressive strength of 22.5 MPa and a tensile strength of 25.3 MPa. This result yields a ratio of tensile strength to compressive strength of 1.12[60].

Based on measured the ratio $\tau/\sigma$ and characteristic constant $K$, calculated values of $k$ are presented in Fig. 3-8(b) and it shows that $k$ values are dependent on ligament size. Figs. 3-8(a) and (b) give clue to understand ligament-size related indentation size effect trend in np-Au. For samples #1~#3, as ligament size increases, the ratio of shear strength to compressive strength, $\tau/\sigma$, decreases and $k$ increases, and multiplication of $\tau/\sigma$ and $k$ yields almost same characteristic constant $K$ in Eq. (3-7). Sample #4 ($l$ = 630 nm) has much higher k value than other three samples since the constant $K$ is higher than three samples and the ratio of $\tau/\sigma$ of sample #4 is similar to sample #3. In other words, sample #4 shows enhanced indentation size effect behavior comparing with np-Au with smaller ligament size.

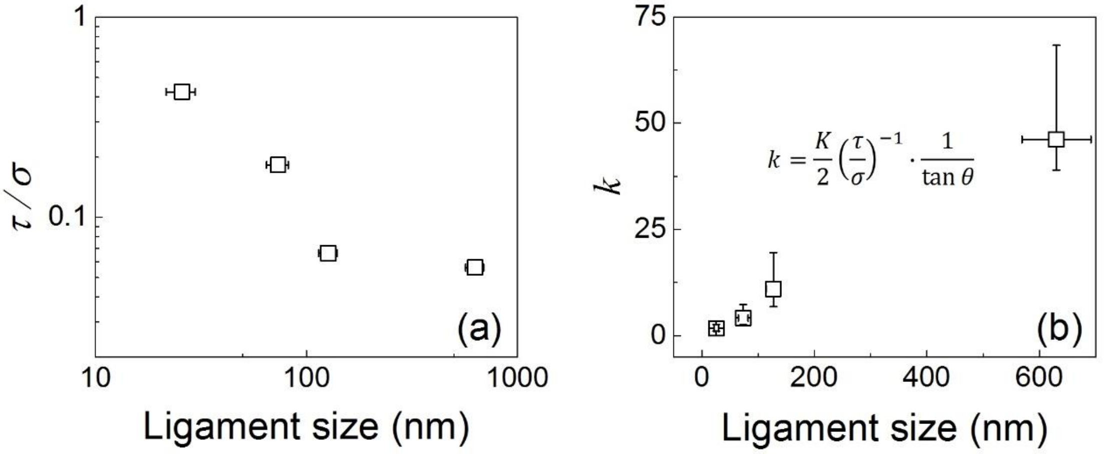

**Figure 3-8** Relation between (a) shear strength/compressive yield strength and ligament size and (b) constant k and ligament size (adapted from Kim et al., Copyright 2017 Elsevier[49]).

### 3.1.3 Ligament Size Effect and Indentation Size Effect Relation

As discussed in previous section, both compressive and shear strength have ligament size dependency shown in Figs. 3-6(c) and 3-7(c). But the ratio of shear strength to compressive strength decreases as ligament size increase and slightly alleviate for sample #4 ($l$ = 630 nm) described in Fig. 3-8(a). This trend comes from difference in the size effect exponents $m$, i.e. the slope of strength vs ligament size curve in log-log scale in Figs. 3-6(c) and 3-7(c). The size effect exponent for compressive strength, $m_{comp}$, is 0.98 (Fig. 3-6(c)) and that for shear strength, $m_{shear}$, is 1.60 (Fig. 3-7(c)). The size effect exponent for shear strength is 39% greater than that for compressive strength, which is caused by difference in deformation mode for shearing and compression.

It has been reported from many studies that yield strength of nanostructured materials indicates power-law-type dependence on characteristic length. Briot and Balk reported power law exponent of -0.551 function of ligament size on yield strength obtained from converted yield strength from nanoindentation hardness, which reported by Hodge *et al.*, with a plastic constraint factor $\Psi$ of 2.65[12, 41]. McCue *et al.*, analyzed the power law exponents calculated from experimental data obtained by 6 different mechanical tests reported by 17 previous research articles[51]. Upper and lower boundaries for the power law exponents are -0.97 and -0.73, respectively. Obtained $m_{comp}$ of -0.98 for compressive yield strength in this study is in good agreement with this trend. Li and Sieradzki have reported ligament size dependent change in fracture stress with power law exponent of -0.2 from three-point bending tests[58]. Badwe *et al.*, recently reported the power law exponent of -0.23 for tensile fracture stress for brittle fracture region corresponding to ligament size smaller than about 220 nm[61]. Mameka *et al.*, recently found that phenomena that strength and hardness of np-Au increase as ligament size decreases is universal, but the power law exponents that had reported are quite diverse depending on materials and mechanical tests[62].

Greer *et al.*, measured compressive flow stress at 10% strain for Au micropillars with diameters ranging from 300 nm to 7450 nm[9]. They found that the relation between flow stress and micropillar diameter can be described with two power-law exponents in transition at critical pillar diameter of about 1000 nm. Brinckmann *et al.*, showed that size-dependent compressive strength of Au nanopillars is described with the power law exponent of -0.97[63]. The Hall-Petch relationship describing dependence of yield strength on grain size for nanocrystalline metals shows the power law exponent of -0.5[64]. Deformation mechanism in np-Au might be similar to that of Au nanopillars in terms that mobile dislocations can escape at free surface due to external size of sub-micron scale, whereas dislocations can pile up at grain boundaries in nanocrystalline metals[65]. While entire volumes of nano- and micro-pillars are in uni-axial stress and strain conditions, ligaments in np-Au have surface curvature and irregular distribution in size and orientation introducing complex stress and strain in the ligaments, hence power-law exponents could be different from Au nano- and micro-pillars.

The size effect of materials at sub-micron scale is attributed to dislocation starvation or depletion of dislocation sources, since dislocations tend to escape at free surfaces and dislocations are exhausted due to small external size rather than multiplying as in bulk metals. In shear testing of np-Au, plastic deformation is likely localized at necks of ligaments, possibly the thinnest part in ligaments. Dislocation starvation model that take into account size effect in Au nanopillar compression could be applied to shear strength of np-Au since the dislocations on ligament surface can travel through ligament and escape at the opposite free surface of ligament. Ngo *et al.*, suggested that initial yielding in compression of np-Au occurs at very early stage of loading due to surface-induced prestress and anomalously high elastic compliance through MD simulations[66]. They also found that typical dislocation-based mechanism contributes to the strain hardening of np-Au during compressive deformation while dislocation-starvation model is not applied to np-Au under compression.

Np-Au has irregular geometry in curvature, ligament thickness and orientation of ligaments as contrasted with nano- and micro-pillars made by FIB milling and lithography. Structural irregularity of np-Au exemplify unique deformation behavior that stress can be concentrated at the thinnest parts, possibly necks of ligaments and existence or density of initial dislocation in volumes of necks is more critical in yielding rather than overall initial dislocation density[13].

The volume of thinnest neck of ligament is assumed to be cylinder with diameter of ligament size and height of ligament size to calculate initial dislocation density when it is under deformation. When initial dislocation density is assumed as $10^9$ $m^{-2}$ of well-annealed gold, total dislocation length in the volume of cylindrical neck is calculated to be $1.38\times10^{-5}$ nm for sample #1($l$=26 nm) and that is 0.2 nm for sample #4($l$=630 nm)[67]. This means that rare initial dislocations are statistically included in the neck volumes that is critical in yielding. Also, length of initial dislocation in the neck is much lower than in the ligament junction and difference in yielding mechanism under shear and compressive deformation could lead to imbalance in power law exponents of shear and compressive modes. The difference in the size effect exponent $m$ in shear and compressive strengths yields a trend of $\tau/\sigma$ as a function of ligament size, as shown in Fig. 3-8(a), and associates indentation size effect in np-Au depending on ligament size.

Figure 3-8(b) shows that *k,* the proportional constant in Eq. (3-7), is proportional to ligament size. In the proposed nanomechanical modeling for indentation size effect in np-Au, *k* means the number of cells deformed along the loading direction by shear force in the circumferential area $2\pi r \cdot D$ when indentation depth increases by *D*. But it is hard to define *k* exactly in the case of real indentation on np-Au. By my definition of *k*, it is understandable that *k* would correlate with depth where shear stress is applied at indent boundary between the np-Au surface and nanoindenter. In terms of normalized indentation depth, the strength of ligaments decreases with increasing ligament size. In other words, in self-similar structures of ligaments and pores for samples #1-#4, only the ligament strength is different.

The increase in $k$ with increasing ligament size demonstrates that shear stress introduced at indent boundary is applied farther as ligament strength decreases in terms of normalized indentation depth. Therefore, the origin of indentation size effect in np-Au is attributed to a combination of ligament-size-dependent $\tau/\sigma$ and $k$ shown in Figs. 3-8(a) and 3-8(b).

## 3.2 Indentation Size Effect and Indentation Size Effect Relation in Spherical Tip Indentation

Spherical indentation has been widely studied because unlike geometrically self-similar sharp indenters, spherical indenters introduce various stress–strain fields depending on the indentation depth [68-69]. These days, studies to measure tensile properties by spherical indentation have been suggested and trend of indentation size effect in spherical indentation becomes important. Indentation size effect in spherical indentation is induced by indenter tip radius, on the contrary to indentation size effect in sharp tip indentation induced by indentation depth. As in indentation size effect for sharp tip indentation, numerical explanation is introduced to describe indentation size effect for spherical tip indentation [70]. Indentation depth is defined as $h_p = \frac{r^2}{2R_P}$, where $R_p$ is spherical radius of residual surface, $r$ is indenter radius. Total length of dislocation loops, λ, is described as $\lambda = \frac{2\pi a^3}{3bR_P}$ where contact radius is $a$ and average density of geometrically necessary dislocations is $\rho_G = \frac{1}{bR_P}$. Contact radius, a, is calculated by function of $R_p$ and hp as $a^2 = 2R_P h_P - h_P^2$. Similar to Nix-Gao model, indentation size effect for spherical indentation is expressed by

$$H/H_0 = \sqrt{1 + R^*/R_P} \qquad (3\text{-}8)$$

when characteristic constant, $R^*$ is $R^* = \bar{r}/b\rho_S$. Though indentation size effect for spherical indentation have been studied for solid material, it has not been studied for np-metal. Thus, nanomechanical modeling was suggested and the correlation of the indentation size effects for spherical and sharp (Berkovich) indentations was investigated in terms of strain hardening and indentation work.

### 3.2.1 Experimental Results and Nanomechanical Modeling

Since indentation size effect in spherical indentation is induced by tip radius, ligament size of np-Au samples was designed to be single value of 26 nm. Pure Au and Ag pellets was melted to fabricated precursor AgAu alloy with composition of 30 at.% of Au and 70 at.% of Ag using arc melter and copper crucible. After alloying, $Ag_{70}Au_{30}$ alloy went through homogenization at 800 °C for 72 h under a $N_2$ atmosphere and was pressed into plate shape with a thickness of 1 mm using an universal testing machine (Instron 5982). $Ag_{70}Au_{30}$ alloy plate was polished down to 0.25 μm using diamond suspension and was annealed in a tube furnace in a $N_2$ environment at 800 °C for 24 h to alleviate residual stress induced by mechanical machining and polishing. Then, precursor alloy was immersed into a 70% $HNO_3$ solution for 72 h at room temperature for free-corrosion dealloying to produce nanoporous structure. Ligament sizes were defined by averaging thickness of the neck diameters which are possibly the thinnest parts of ligaments measured by using scanning electron microscope images.

Spherical nanoindentations were carried out using diamond spheroconical indenters with nominal tip radii of 4, 12, and 50 µm. Effective radius, $R$, of each indenter was measured by using optical microscope from the side view; the radii were 3.68 (±0.07) µm for the 4 µm nominal radius, 11.42 (±0.11) µm for the 12 µm nominal radius, and 54.99 (±0.39) µm for the 50 µm nominal radius. Figure 3-9(a) describes indenter geometry during indentation; $R$ is indenter radius which is measured effective radius, indentation depth which is the maximum height from tip point to pile-up surface less than effective indentation depth, and $a$ is contact radius after penetration. Spherical nanoindentations were conducted using the XP module of a Nanoindenter G200 (KLA) with a maximum load capacity of 500 mN in the CSM mode at an indentation strain rate of 0.05 $s^{-1}$.

Figure 3-9(b)-(d) shows typical spherical indentation force to indentation depth curves for np-Au. Obtained hardness values from nanoindentation with different tip radius are presented as a function of the contact radius, $a$, in Fig. 3-10. Indentation depth was designated by having $a/R = 0.142$, where $R$ is the indenter radius. The ratio of $a/R = 0.142$ corresponds to the compressive yield strain, which is discussed in detail below. The hardness and the contact radius were calculated by the Oliver–Pharr method[71]. Figure 3-10 indicates that calculated hardness increases with smaller contact radius. In other words, np-Au shows similar tendency to indentation size effect in spherical indentation on solid materials[70]. The hardness values in Fig. 3-10 were averaged from more than 15 reproducible indentation force–depth curves.

To analyze the indentation size effect for spherical nanoindentation on np-Au, nanomechanics model was developed similar to previous chapter[49]. As shown in Fig. 3-11(a), the spherical indenter is assumed to be series of infinitesimal thin flat punches. Same with nanomechanics model for sharp indenter, the total indentation work is considered to be consumed in the plastic collapse of the unit cells of np-Au caused by normal and shear forces. When the cell size, $D$, is $3l$, the indentation force is equal to the differential of the total indentation work:

$$P = \frac{dW}{dh} = \frac{w_{\text{total}}}{D} = \frac{w_{\text{comp}} + w_{\text{shear}}}{D}. \qquad (3\text{-}9)$$

Here, the work dissipated by compressive and shear forces is

$$w_{\text{comp}} = \sigma \cdot \pi r^2 \cdot D, \qquad (3\text{-}10)$$

$$w_{\text{shear}} = \tau \cdot 2\pi r \cdot D \cdot k_R D, \qquad (3\text{-}11)$$

where nomenclatures are same with nanomechanics model for sharp indentation but, $k_R$ is a proportional constant in spherical indentation indicating the number of cells deformed along the loading direction by the shear force at the circumferential area $2\pi r \cdot D$ when the indentation depth increases as far as $D$. Contact radius $a$ can be described as $R\sin\theta$, where $\theta$ is the contact angle between the specimen plane surface and the indenter surface as shown in Fig. 3-11. Combining equations through Eq.(3-8) to Eq. (3-11) with Tabor's relation $\sigma = H_0/\Psi$ yields

$$\frac{H}{H_0} = \frac{1}{\Psi}\left(1 + \frac{K_R}{R/D}\right), \qquad (3\text{-}12)$$

$$K_R = \frac{\tau}{\sigma} \cdot \frac{2k_R}{sin\,\theta}. \qquad (3\text{-}13)$$

Eq. (3-12) suggests that hardness depends on the indenter radius normalized by the unit cell size of np-Au, *R/D*, in the spherical indentation on np-Au[49].

The solid black line in Fig.3-10 is fitted curve of Eq. (3-12) to experimental values. From the fitted curves, it is shown that Eq.(3-12) describes contact-radius-dependent hardness trend accordingly. The characteristic constant $K_R$ and the macroscopic hardness $H_0$ in Eq. (3-12) are found to be 2026 and 117.6 MPa, respectively, when a plastic constraint factor $\Psi$ is assumed to be 2.65[41, 72]. $k_R$ value was also evaluated to be 339 in Eq. (3-13) by using obtained value in previous chapter when ligament size is 26 nm(np-Au sample #1) having $\tau/\sigma$=0.42 and $\sin\theta$=0.142 (=$a/R$). In comparison with Berkovich indentation, $k$ was 2.56. $k_R$ for the spherical indenter and $k$ for the Berkovich indenter have the same physical essence: the number of cells deformed along the loading direction by the shearing force at the circumferential area $2\pi r \cdot D$ when the indentation depth increases as much as $D$. But, contact angle for spherical indentation was assigned to be 8.16° which is much less than contact angle for Berkovich indentation of 19.7°. That is, number of cells deformed to in-plane direction is higher in spherical indentation than those of Berkovich indentation when have same penetration depth of $D$.

Since np-Au has surface curvature with roughness of ligament size, nanoindentation results might be affected by surface roughness different from nanoindentation on flat surface of solid materials. Whether the tip surface is in contact with ligament or not should be considered to get away from confusion. The depth difference, $h_0$, is defined as height difference when contact at the top of the ligament and at the middle of two ligaments. It can be expressed as

$$h_0 = R + \frac{l}{2} - \sqrt{(R + 2l)(R - l)}. \qquad (3\text{-}14)$$

The average contact depth for spherical indentation could be assumed to be the half of $h_0$ and possible range of hardness differed by tip position is drawn in Fig. 3-10 with red and blue dot lines. By calculating possible deviation in tip position, aberration in hardness for each spherical tip is approximately 0.4%, 0.04%, and 0.002% for the indenters with nominal radii of 4, 12, and 50 μm, respectively. Thus aberration by tip contact position doesn't give significant difference in hardness values obtained from spherical indentation as shown in Fig. 3-10.

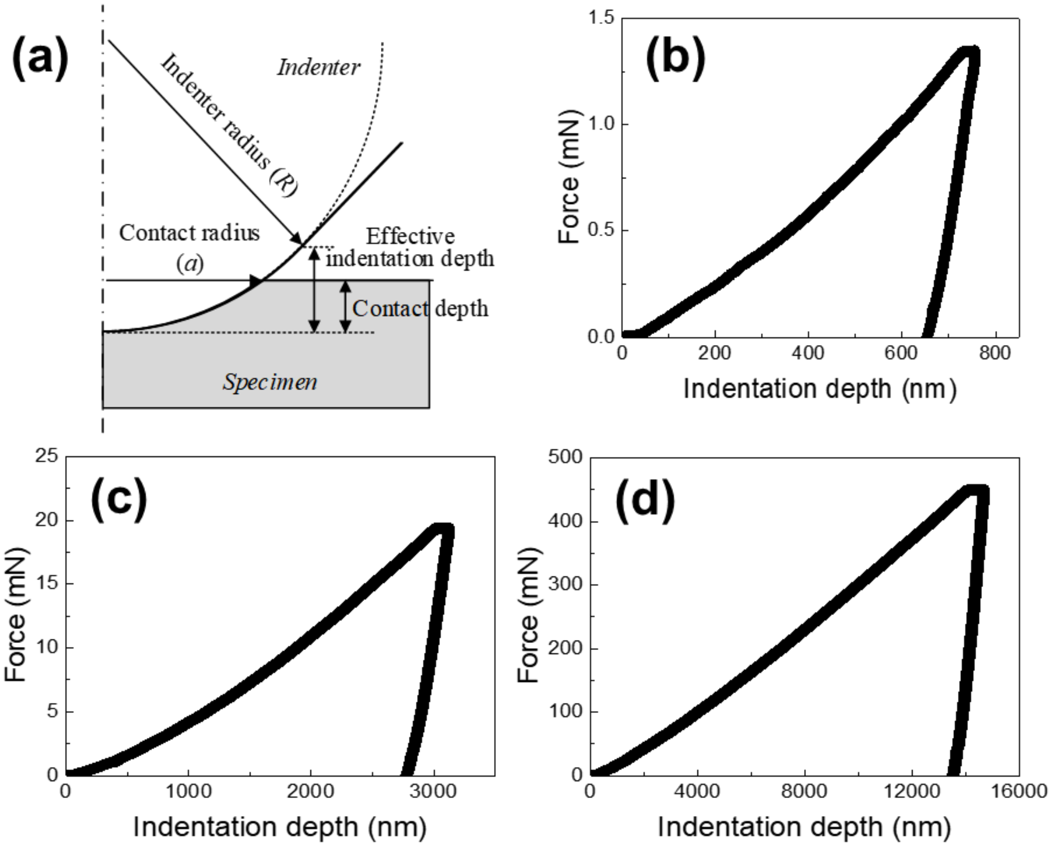

**Figure 3-9** (a) Graphical definitions of contact morphology and typical force-indentation depth curves for spherical indentation with (b) 4, (c) 12 and (d) 50 μm tip radii (adapted from Kim et al., Copyright 2018 Elsevier[14]).

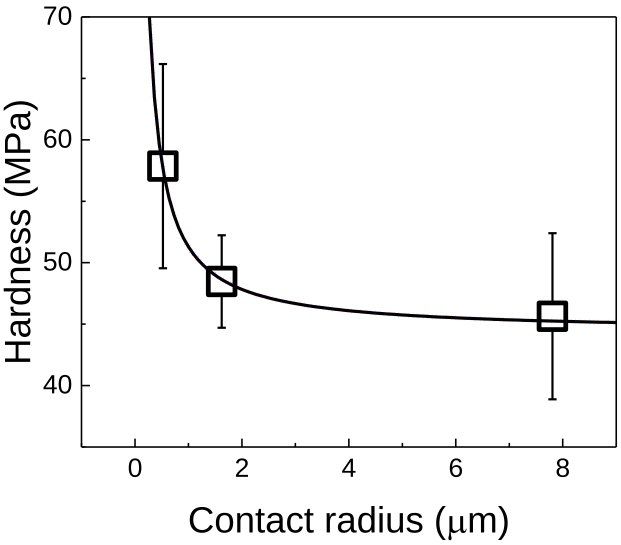

**Figure 3-10** Relation between indentation hardness and contact radius (adapted from Kim et al., Copyright 2018 Elsevier[14]).

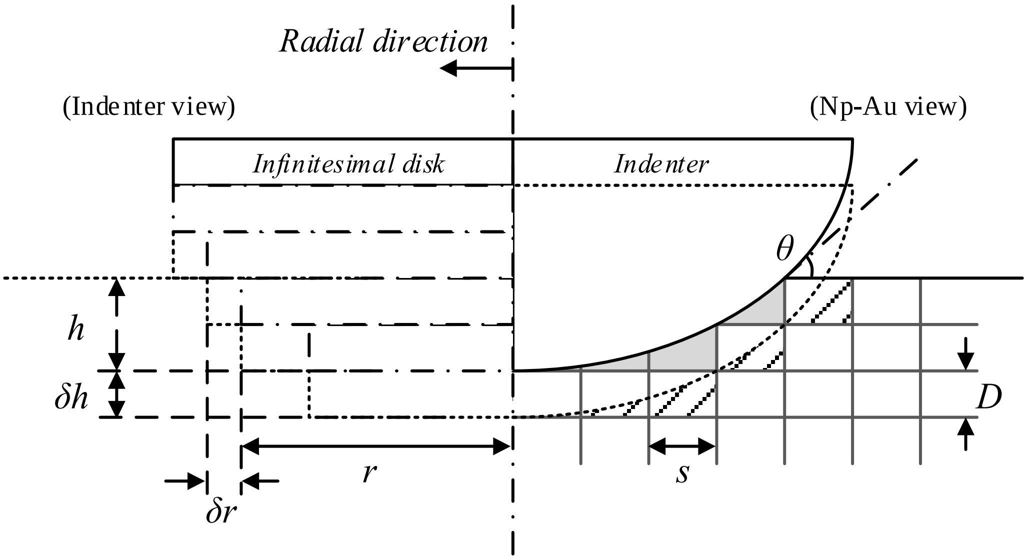

**Figure 3-11** Nanomechanical modeling of spherical indentation on np-material (adapted from Kim et al., Copyright 2018 Elsevier[14]).

### 3.2.2 Relation between Indentation Size Effect Trend of Sharp Tip and Spherical Tip

The representative strain for Berkovich indenter is consistent with any indentation depth, which means geometrically self-similar, representative strain of spherical indenter changes by indentation depth. The representative strain in spherical indenter increases with increasing indentation depth. In general, np-Au shows three deformation stages during compression; linear elastic region, plastic collapse and densification as increasing compressive strain. So, strain hardening could be occurred during spherical indentation by changing representative strain as shown in Fig. 3-12(a). Swadener *et al*. have reported indentation size effect in spherical indentation with different indenter tip radius by adjusting indentation depth to have same representative strain, that is, *a/R* value is same for all indenters[70]. In this part, the representative strains are maintained to be 2.84% for all cases by controlling *a/R* value to be 0.142. Representative strain of 2.84% is same with compressive yield stress of np-Au sample with ligament size of 26 nm as presented in Fig. 3-12(a). So, strain hardening is not prominent in spherical indentation hardness.

The indentation size effects for Berkovich and spherical indentations can be correlated based on the concept of the total length of GNDs in solid materials because GND density is the primary mechanism for the indentation size effect in solid materials[70]. Similar to solid materials, the indentation size effects for Berkovich and spherical indentations of np-Au can be correlated by taking into consideration the indentation work caused by shear force, $w_{shear}$. According to the Eq. (3-12), indentation size effect in spherical indentation is related with constant $K_R$ which is induced by shear work during indentation and the figure $K_R$ is not zero. That means indentation work caused by shear force is the primary mechanism for the indentation size effect during spherical indentation of np-Au. The indentation work by shearing force for Berkovich indentation and spherical indentation are $w_{shear} = \tau \cdot 2\pi h(tan\,\theta)^{-1} \cdot D \cdot kD$ and $w_{shear} = \tau \cdot 2\pi R\, sin\,\theta \cdot D \cdot k_R D$ , respectively. When indentation work by shearing is assumed to be same, the relation between indenter radius and indentation depth is calculated to be $R = 0.149h$. In np-Au, strain hardening is occurred by irregular porous structure in plastic collapse stage. The ratio of $R = 0.149h$ corresponds to the difference in flow stresses of 38.5 MPa between representative strain of 7% for a Berkovich indenter and 2.84% for a spherical indenter as shown in Fig. 3-12(a). This difference is presented on the right and left axes of Fig. 3-12(b), and $R = 0.149h$, which is derived above, is presented on the top and bottom axes of Fig. 3-12(b). Figure 3-12(b) shows that the indentation size effects for the Berkovich and spherical indentations on np-Au show similar trends. Based on this correlation, the trend in the indentation size effect for spherical indentations on np-Au is evaluated by that for Berkovich indentations, and vice versa.

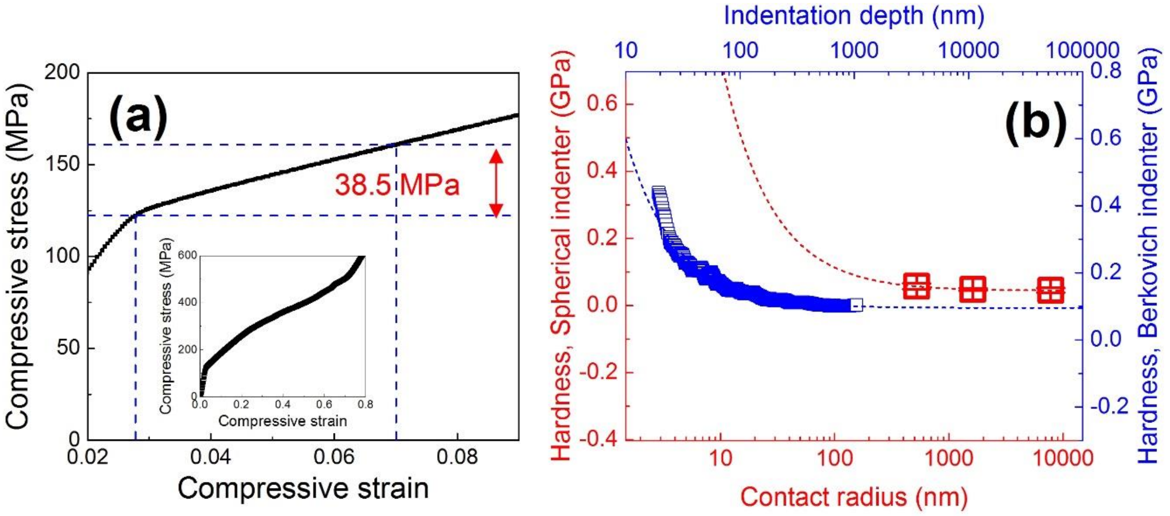

**Figure 3-12** (a) Typical compressive stress-strain curve for ligament size of 26 nm (inset of entire curve) and (b) hardness-contact radius relation comparing with hardness-indentation depth relation in sharp tip indentation (adapted from Kim et al., Copyright 2018 Elsevier[14]).

## 3.3 Conclusion

In this chapter, nanomechanical modeling and mechanical characterization by nanoindentation, compression and shear test were conducted to figure out mechanism of indentation size effect of np-Au in both sharp Berkovich indentation and spherical indentation. Nanomechanical modeling is based on that total work of indentation is the summation of work by compressive force under indenter and work by shear force on circumferential area around indenter. The indentation size effect in np-Au caused by the difference in size-effect exponents in compression and shear loading depending on ligament sizes, where the size effect dependency in shear strength is stronger on ligament size than that in compressive strength. This phenomenon was come from irregular nanoporous structure and explained by dislocation movements toward thinner connections in ligaments and thicker junctions in ligaments, resulting in a tendency to greater strain-hardening by dislocation pile-up during bending of ligament structure Thus, the ratio of shear to compressive strength depends on ligament size. The combination of a linear increase in $k$ and a convergent decrease in $\tau/\sigma$ caused by different size-effect exponents in shear and compressive strength with increasing ligament size explains the indentation size effect transition between ligament sizes of 126 and 630 nm.

We investigated the indentation size effect for spherical indentation on np-Au samples using three different indenters. The indentation depth was set depending on the indenter radius so that the same representative strain was used for consistency in geometrical similarity. We developed a nanomechanics model for the indentation size effect during spherical indentation on np-Au based on two forms of work expended in the plastic collapse caused by the pressing and shearing of internal cells. According to the experimental and modeling results, $k_R$ is considerably greater than $k$ for Berkovich indentation; this might be because more in-plane cells are deformed by the shear force along the loading direction during penetration because of the lower contact angle of the spherical indenter. We correlated the indentation size effects for the spherical and Berkovich indentations by comparing the strain-hardening behavior in the compressive stress–strain curve in terms of the representative strain and indentation work caused by shear force for each indenter.

# 4. Mechanical Properties of Np-Au Depending on Internal Microstructures

## 4.1 Effect of Grain Size and Initial Dislocation Density on Deformation of Np-Au

Based on materials science and engineering, process can change microstructure in materials and microstructure can change properties and performance. During deformation of np-Au, mechanism of plastic deformation is dislocation motion in individual ligaments. That is, new approaches about controlling microstructure in ligaments should be considered to obtain enhanced mechanical property. In np-Au, microstructure in precursor is preserved during dealloying due to short surface diffusion range. In other words, microstructure of np-Au could be varied by controlling microstructure of precursor[50].

For crystalline metal alloys, mechanical properties depend on motion of dislocations. By restricting dislocation mobility, required force to initiate plastic deformation would be increased leading to enhanced mechanical strength. Grain size reduction is the most common method among strengthening mechanism for polycrystalline metals. Grain boundary is planar defect that acts as dislocation barrier that difference of crystallographic orientation between adjacent grains and atomic disorder induce higher stress for dislocation motion. Thus, the smaller grain size, the harder and stronger polycrystalline metals. The dependence of yield strength, $\sigma_y$, on average grain size, $d$, could be explained by Hall-Petch relation as

$$\sigma_y = \sigma_0 + k_y d^{-1/2}. \qquad (4\text{-}1)$$

where $\sigma_0$ and $k_y$ are constant for particular material. Hall-Petch relation (eq. 4-1) is useful and well-fitted for grain size in the range of 10~100 μm where most engineering alloys have grain size in that range. To get high strength, fabrication techniques and research about mechanical properties of ultra-fine grained material with grain size in range of 250 ~ 1000 nm and nanocrystalline material with grain size in range of 1 ~ 250 nm have been developed. Nanocrystalline materials possess large volume fraction of grain boundary than that of materials with coarsened grain. High grain boundary density might alter mechanical, electrical and chemical properties. In the case of mechanical properties of nanocrystalline metals, Hall-Petch trend could not be corresponded in grain size below critical grain size around 1 μm. This phenomenon is called inverse Hall-Petch relation. Inverse Hall-Petch trend is originated from transition of main deformation mechanism. When grain size is too small, a grain contains rare dislocation and dislocation pile-up could be retained. Since threshold stress for dislocation transmission through grain boundary reaches to maximum, deformation mechanism alters to grain-boundary sliding due to large excess volume along grain boundary.

One of strengthening mechanism of metal is strain hardening. Strain hardening is a phenomenon that strength increases with plastic deformation. Plastic deformation increases dislocation density in metals and introduces dislocation interaction and multiplication. Repulsive interaction between dislocations increase resistance to dislocation motion leading hardening of material.

In this part, microstructural evolution of np-Au is examined using scanning electron microscopy, energy dispersive spectroscopy, electron back-scattered diffraction and transmission electron microscopy. Effect of microstructure on mechanical behavior of np-Au is investigated by nanoindentation, flexural test and tensile test.

### 4.1.1 Fabrication of Nanocrystalline and Pre-strained Np-Au

Same with previous chapter, np-Au samples were prepared by free-corrosion dealloying from precursor Au-Ag alloys ($Ag_{72}Au_{28}$ in at.%), which were fabricated from Au (99.99%) and Ag (99.99%) pellets by melting at 1100°C and homogenizing for 72 hours at 850°C under nitrogen atmosphere. From this homogenized state, three different 'annealed', 'pre-strained', and 'ball-milled' precursor alloys were prepared. Samples are named by their fabrication process which controls internal microstructure in precursors. Samples called 'annealed' and 'pre-strained' were cut into about 1mm-thick disks, polished on both sides with 0.25 μm diamond suspension, and annealed for 24 hours at 850°C to relieve stress. The as-annealed sample is referred to as 'annealed' precursor alloy. Some annealed precursor alloys were compressed to 5% compressive engineering strain using a universal testing machine (Instron 5982) at loading rate 50 μm/min. This compressed sample is called the 'pre-strained' precursor alloy. There are various synthesis methods for nanocrystalline material as shown in Fig. 4-1. Ball milling process is a kind of top-down nanocrystallization technique by severe plastic deformation. Repeated deformation by impact of hard balls and dynamic recrystallization produces nanocrystalline structure in material. Grain size decreases with increasing milling time during ball-milling. Advantages of nanocrystallization by ball-milling are that homogeneous microstructure could be obtained and process is at near room temperature. The 'ball-milled' sample was prepared by high-energy ball milling (SPEX Mixer Mill 8000D). After homogenization, pieces of this alloy were sealed in stainless steel vials together with stainless steel balls and shaken at 1060 back-and-forth cycles/min for an hour. Ball-milled alloys were cut into about 1 mm-thick disk and polished gently on both sides with 0.25 μm diamond suspension.

For free corrosion dealloying to obtain np-Au, these three precursor alloys were dipped in diluted 35% nitric acid at 80 °C for 72 hours and rinsed repeatedly with ethanol and de-ionized water. Np-Au samples were examined by field emission scanning electron microscopy (FE-SEM, FEI NovaNano 230) for imaging, energy-dispersive x-ray spectroscopy (EDS) to measure amount of residual Ag, and electron backscatter diffraction (EBSD, TSL-OIM) to obtain an inverse pole figure.

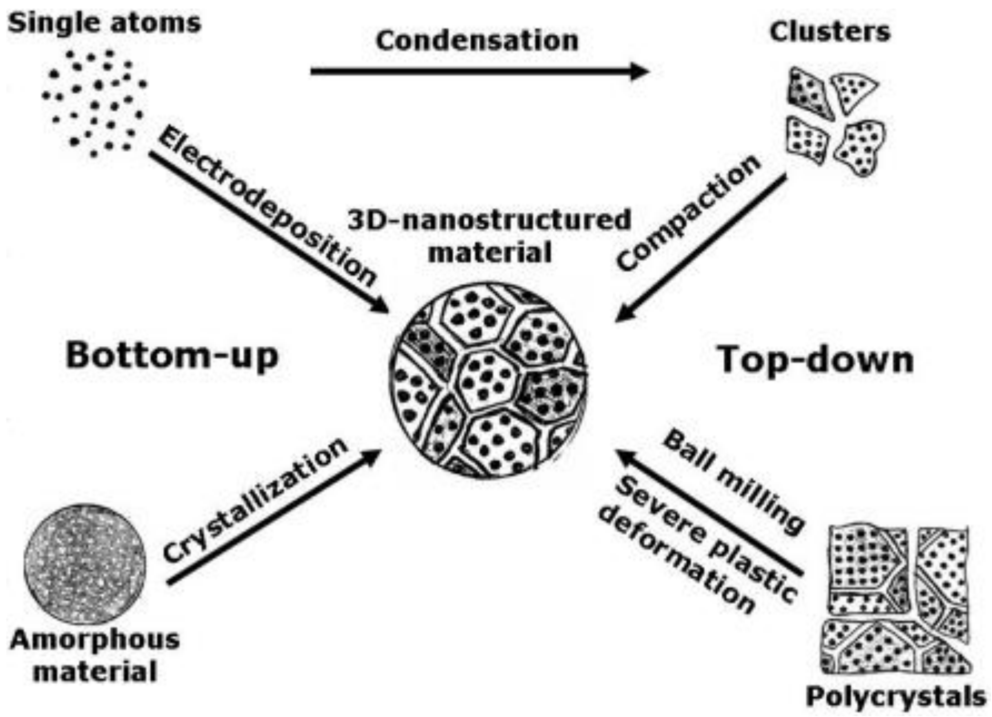

**Figure 4-1** Schematics of approaches for synthesis of nanocrystalline materials (adapted from Murty and Venugopal, Copyright 2011 Encycl. Nanosci. Nanotechnol.[73]).

Nanoindentation and flexural test were performed to np-Au samples to see effect of internal microstructure on mechanical responses under different stress conditions. Nanoindentations (KLA Nanoindenter G200) were carried out on precursor alloys and np-Au samples with a Berkovich indenter using continuous stiffness measurement (CSM) in XP module with force capacity 500 mN for the precursor alloys and dynamic contact module II (DCM II) with force capacity 30 mN for np-Au samples. Nanoindentations were performed to a maximum indentation depth of 2.5 μm with strain rate 0.05 $s^{-1}$. Nanoindentation data were analyzed from 80 nanoindentations for each sample. Three-point bending tests were performed with a custom-build three-point bending jig of 4 mm span length at constant cross-head speed of 0.002 mm/s using a micro-scale universal testing machine (Instron 5948). Cuboid samples for the bending tests were machined from both-sides-polished precursor alloys to dimensions of 2 mm-wide, 8 mm-long and 0.5 mm-thick beams using a nano-machining instrument (FANUC Ultra-Precision Nano Machine). Span length and sample dimension for three-point bending tests were determined by a standard test method[74].

Figure 4-2 shows microstructure evolution in three precursors and np-Au samples. Figure 4-2(a)-(c) show EBSD inverse pole-figure (IPF) maps for precursor alloys. Grain sizes were measured by intercept method from IPF images of each samples. Grain sizes were 238 μm for the annealed precursor alloy, 266 μm for the pre-strained one, and 206 nm for ball-milled one, respectively. Fig. 4-2(c) shows that ultra-fine grains are uniformly formed by the high-energy ball-milling process. Evolution of texture was not observed in the pre-straining and ball-milling process. Fig. 4-2(d)-(e) display EBSD IPF maps for np-Au after dealloying. Those images exhibit that grain morphology and crystallographic orientation were preserved in free-corrosion dealloying for all three samples. This implies that nanoporosity formation is accomplished by short-range surface diffusion of Au atoms during dealloying[31-32, 50, 75]. Figure 4-2(j)-(l) show SEM images for np-Au samples obtained from three different precursor alloys: annealed, pre-strained and ball-milled. Ligament sizes were measured from at least 100 measurements necks at the center of connects in ligaments, possibly the thinnest part in ligaments in SEM images. Ligament sizes are almost identical: 73 (±19.5) nm for annealed, 70 (±21.9) nm for pre-strained, and 75 (±24.2) nm for ball-milled np-Au. The pre-strained precursor alloy is presumed to have higher initial dislocation density than the annealed one, and the ball-milled precursor alloy is most likely to have greater densities of initial dislocations and grain boundaries than the other two precursor alloys. Size and morphology of ligaments and pores are known to be controlled by precursor composition[76], dealloying conditions[7, 37], and post-treatment[38]. On the other hand, the almost identical ligament sizes for three np-Au samples imply that changes in initial dislocation density and grain size in a precursor alloy are unlikely to change the nanoporous structure obtained by dealloying.

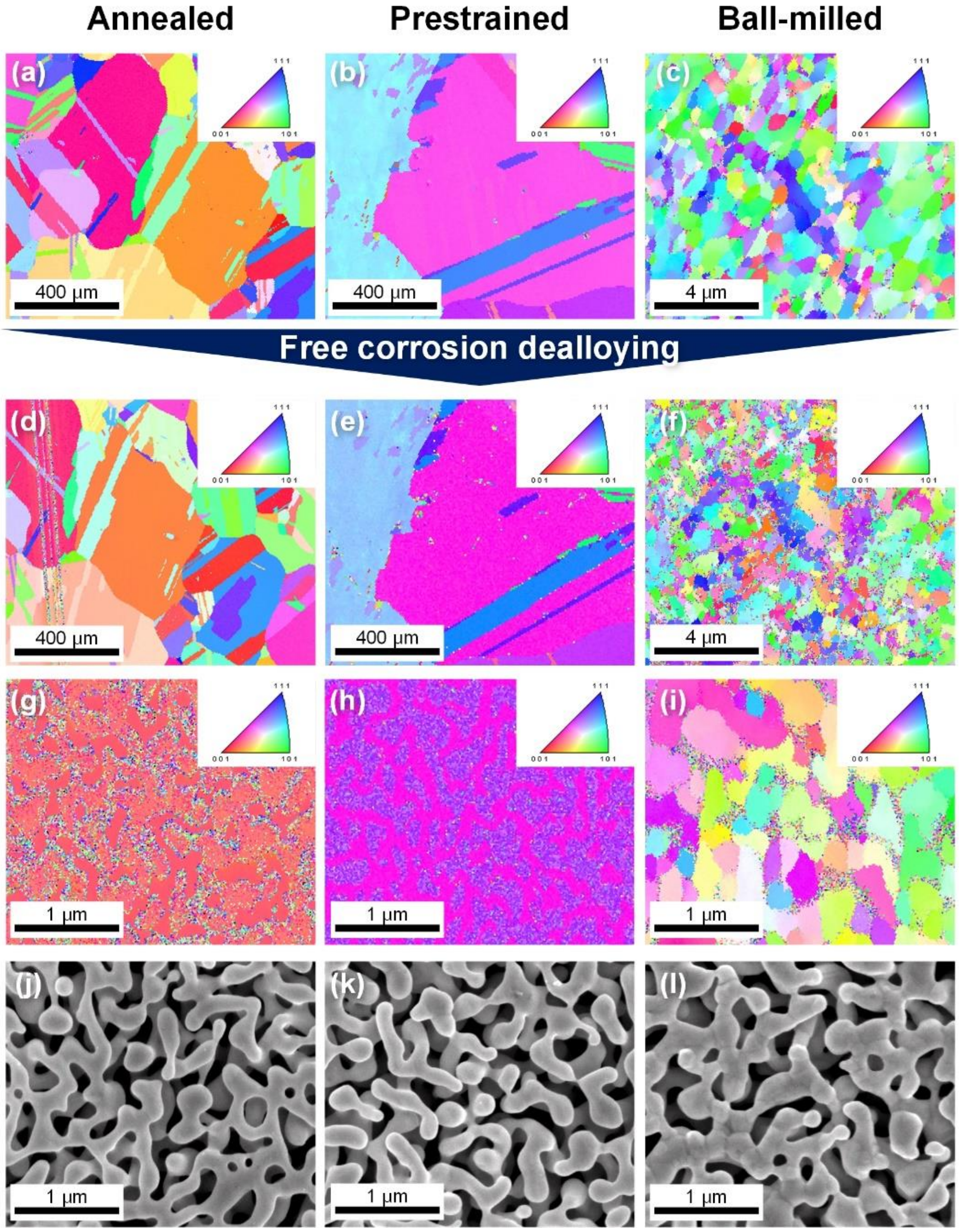

**Figure 4-2** (a)-(i) Grain structure and (j)-(l) surface morphology before and after dealloying of annealed, prestrained and ball-milled samples (adapted from Gwak and Kim Copyright 2016 American Chemical Society[15]).

### 4.1.2 Nanoindentation on Np-Au Samples

Typical and average nanoindentation force-depth curves for the three precursor alloys are presented in Fig. 4-3(a) and (b). Forces attained at maximum indentation depth of 2.5 μm are in the order of ball-milled, pre-strained, and annealed precursor alloys. Since Ag-Au precursor alloy shows indentation size effect where hardness is increased by decreasing indentation depth, hardness averaged for 25 nanoindentation curves of each sample for indentation depth from 2 to 2.5 μm is 0.93 (±0.04) GPa for ball-milled, 0.63 (±0.06) GPa for pre-strained, and 0.48 (±0.01) GPa for annealed samples, while elastic moduli in this range are similar: 76.0 (±2.8) GPa for ball-milled, 78.1 (±2.6) GPa for pre-strained, and 72.6 (±2.0) GPa for annealed samples. The greatest hardness of the ball-milled precursor alloy is attributed to refinement of grain size and extremely high initial dislocation density because of the severe plastic deformation induced by the high-energy ball-milling process. The hardness of pre-strained sample is 31.3% higher than that of annealed sample. This could be caused by an increase in initial dislocation density generated by compressive plastic deformation. Assuming that the pre-strained and annealed samples have the same plastic constraint factor and obey the Taylor hardening model, the initial dislocation density of the pre-strained precursor alloy is about two orders of magnitude greater than that of the annealed one, by comparison of macroscopic hardness in the Nix-Gao model[45]. This value agrees well with that evaluated from the change in flow and yield stress in the compression stress-strain curve up to 5% in the pre-straining process.

Typical and average nanoindentation force-depth curves for np-Au samples; the curves are almost identical as shown in Fig. 4-3(c) and (d). As discussed in chapter 3, np-Au shows indentation size effect trend, thus hardness values of np-Au samples averaged for 25 nanoindentation curves for indentation depth from 2.0 to 2.5 μm are 33.5 (±0.74) MPa for ball-milled, 31.1 (±1.79) MPa for pre-strained, and 32.1 (±0.79) MPa for annealed np-Au samples; again, the values are almost identical. These results suggest that grain size and initial dislocation density are not critical factors for determining the nanoindentation hardness of np-Au of ligament size about 70 nm, while nanoindentation hardness of np-Au is known to be strongly dependent on ligament size[11-12]. The compressive strength of a pre-strained Au nanopillar with diameter of 200~300 nm is lower than that of a pristine one since pre-straining introduces weak dislocation sources such as mobile dislocations and single-arm sources[77]. However, the high initial dislocation density of np-Au with ligament size about 70 nm does not affect the nanoindentation hardness. Unlike the uniaxial compression of the nanopillar, ligaments and junctions in np-Au experience such a complicated stress state in nanoindentation that structural stress concentrators are likely to be more critical factors than dislocation sources inside ligaments.

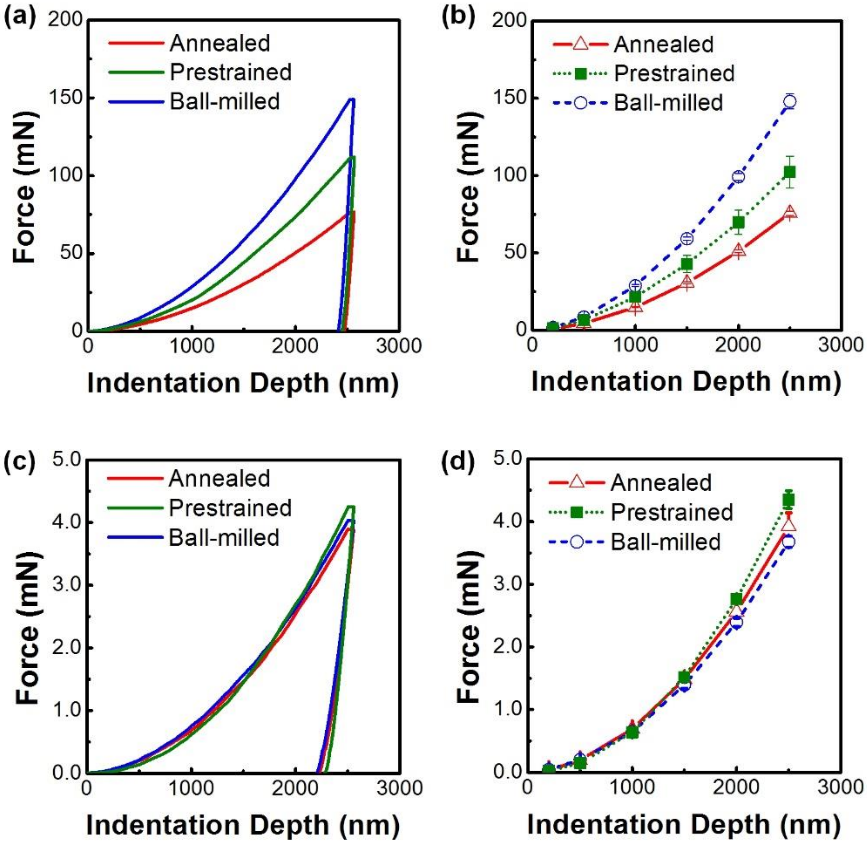

**Figure 4-3** (a) Typical and (b) averaged force-indentation depth curves of precursors and (c), (d) np-Au samples (adapted from Gwak and Kim Copyright 2016 American Chemical Society[15]).

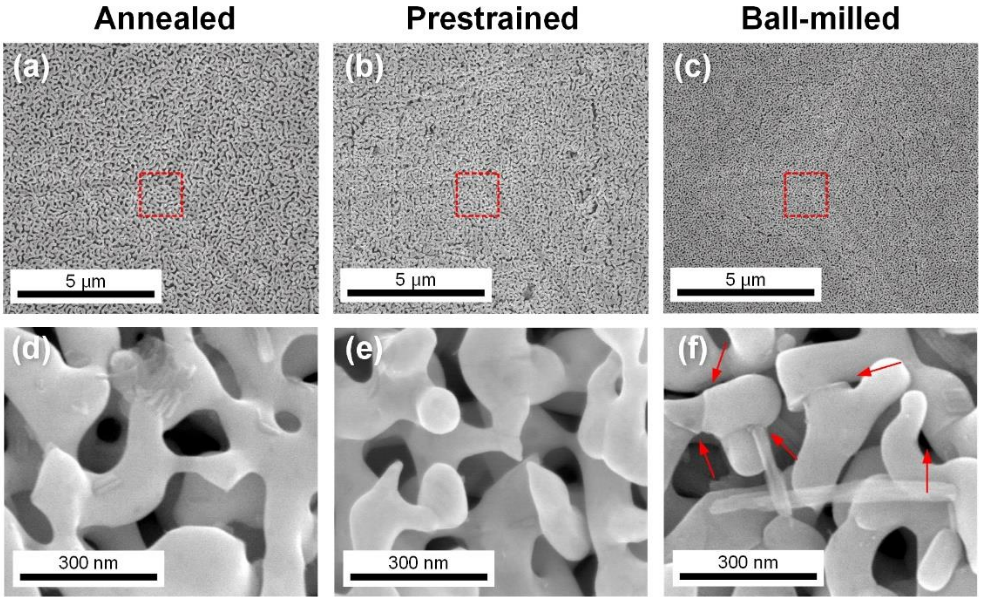

**Figure 4-4** Surface morphology of residual indents after nanoindentation on each sample (adapted from Gwak and Kim Copyright 2016 American Chemical Society[15]).

Figure 4-4(a)-(c) show SEM images of nanoindentation marks on the top of np-Au samples. A common feature of these three images is that ligaments beneath nanoindenter do not experience significant densification during nanoindentation. The relative density of np-Au samples in this chapter was 28% measured by direct weighing. Even ligaments directly beneath the nanoindenter are likely to experience an increase in relative density by structural plastic collapse rather than by severe deformation of ligaments[15, 38]. While this behavior agrees with a previous report for np-Au with relative density 25%, ligaments of np-Au with relative density 42% beneath nanoindenter show severe deformation. The relative density of np-Au might be a primary factor that attribute ligament deformation behavior. As in the Gibson-Ashby model, yield strength and elastic modulus increase with increasing relative density[78]. This implies that in the case of np-Au with higher relative density, undeformed volume can support collapsed region more strongly, so that the collapsed region can be densified as severe deformation of ligaments. On the other hand, for np-Au with lower relative density, expanding collapsed region to undeformed region is more preferred to densifying collapsed ligaments.

Fig. 4-4(d)-(f) show high-magnification SEM images of the nanoindentation marks. As shown in Fig. 4-4(f), ligaments under indentation mark were sheared off by grain-boundary sliding in the ball-milled np-Au (indicated by arrow in Fig. 4-4(f)). Figs. 4-4(d) and (e) show typical plastic collapse features by dislocation slip in ligaments of annealed and pre-strained np-Au samples. Reports on compression of bicrystalline pillars show that a vertically-aligned grain boundary increases strength compared to single-crystalline pillars[79-80], whereas a grain boundary inclined to the loading direction slides in shear stress about 40% below the flow stress of bicrystalline pillar including a vertical grain boundary, which is similar to the flow stress of single crystalline pillars[81]. Grain-boundary density is very high in ball-milled np-Au, and their distribution is random. Some grain boundaries are seen to slide during nanoindentation (as shown in Fig. 4-5), but this grain boundary sliding does not affect nanoindentation hardness significantly.

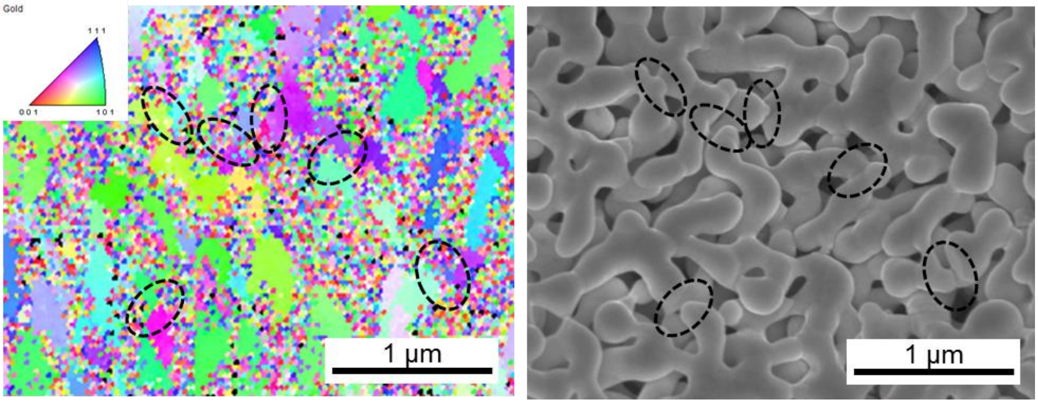

**Figure 4-5** EBSD IPF image and SEM image of residual indent on ball-milled np-Au (adapted from Gwak and Kim Copyright 2016 American Chemical Society[15]).

### 4.1.3 Flexural Test of Np-Au Samples

Figure 4-6 shows fracture behavior of typical np-Au sample during three-point bending test. As discussed in previous researches, np-Au samples show brittleness in fracture by depletion. Fig. 4-7(a) shows typical flexural stress-strain curves for three np-Au samples obtained from three-point bending test. This indicates that np-Au samples show brittle fracture right after the linear elastic regime. Flexural stress $\sigma_f$ is given by $\sigma_f = 3PL/2wt^2$, where $P$ is force, $L$ is outer span length, $w$ is sample width, and $t$ is sample thickness. Flexural strain, $\varepsilon_f$ is expressed by $\varepsilon_f = 6vt/L^2$, where $v$ is the displacement. The average flexural strength is 8.16 (±1.47) MPa for annealed np-Au, and 9.03 (±2.24) MPa for pre-strained np-Au, and 5.41 (±0.68) MPa for ball-milled np-Au, respectively. The flexural strength of ball-milled np-Au is 33.7% lower than that of annealed np-Au and 40.1% lower than that of pre-strained np-Au. Lower flexural strength of ball-milled np-Au suggests that high density of grain boundaries could weaken flexural strength of np-Au.

Fracture surfaces of each specimens were examined using SEM in order to investigate correlation between grain structure and flexural strength as presented in Figs. 4-7(c)-(h). Fig. 4-7(c) and (f) show fracture surface for the highest flexural strength of 12.51 MPa among several data for pre-strained np-Au. The fracture surface is flat at low magnification, and the ligaments show ductile fracture features, necking and point-to-point separation. This is typical transgranular fracture behavior in np-Au[82-83]. Fig. 4-7(d) and (g) show the fracture surface for the lowest flexural strength, 5.55 MPa, among the flexural strengths of annealed np-Au. This fracture surface shows a mixed configuration of transgranular and intergranular fracture. A high-magnification image of the intergranular fracture surface shows undeformed ligaments and area-to-area separations of ligaments (see Fig. 4-7(g)), unlike the point-to-point separation by transgranular fracture in Fig. 4-7(f).

During dealloying, Ag atoms at grain boundaries leach faster than those in the grain interior, so that grain boundaries in np-Au contain excess volumes[82]. Furthermore, Ag atoms segregate to interfaces such as surface or grain boundaries during annealing of the precursor alloys[84]. The amount of residual Ag was about 2 at.% for the three np-Au samples in this chapter. Excess volume and segregated Ag atoms at grain boundaries induce localized stress, and thus grain boundaries act as two-dimensional void-like defects as shown in Fig. 4-8. It seems reasonable from previous experiments and computational simulations that grain boundaries weaken np-Au, especially in tensile or flexural testing. Li and Sieradzki measured fracture strength and strain of np-Au in three-point bending tests[58]. The grain size of np-Au in their work was not reported but could be assumed to be on order of 100 μm or greater, since precursor alloys, they used, was annealed at 900°C for 24 hours. Calculated fracture strengths are 8.2 MPa for ligament size 18 nm and 12 MPa for ligament size 60 nm, whose strengths were similar to measured flexural strengths in this chapter. Biener *et al*. performed three-point bending tests to compare fracture behaviors of np-Au with different ligament sizes[82]. They found that the strength of np-Au depends on 'the largest critical defects' such as grain-boundary opening regions where stress is concentrated. Balk *et al*. compared tensile and compressive behavior of polycrystalline np-Au micro-sample[59].

Fractography of np-Au showed that individual ligaments go through ductile failure by necking even though np-Au exhibits macroscopic brittle fracture. Furthermore, indentation hardness for np-Au was twice the flexural strength in this chapter. Briot *et al*., comparing the tensile properties of polycrystalline and single-crystalline np-Au, found that the strength of single-crystalline np-Au is three times greater than that of polycrystalline np-Au, while cracks initiate at grain boundaries with low connectivity[60]. When there exist grain boundaries parallel to the span direction in three-point bending at the middle of the outer surface where maximum tensile stress is applied, fracture initiates by grain-boundary opening, leading to low flexural strength. On the contrary, high flexural strength is achieved by transgranular fracture. Since grain size of annealed and pre-strained np-Au is relatively large, flexural strength appears to be dependent on the stochastic distribution of grain boundaries and they show the larger scatter in flexural strength for annealed and pre-strained np-Au than for ball-milled np-Au.

Figure 4-7(e) and (h) reveal that the fracture surface was formed by uniform intergranular fracture, possibly due to the small grain size (206 nm) in ball-milled np-Au. This fractured feature clearly illustrates the much lower flexural strength and smaller scatter for ball-milled np-Au. Fractography of np-Au samples prepared from four Au-Cu precursor alloys have been reported when the samples have been fabricated by as-cast state, annealing, cold-rolling and high-pressure torsion (HPT)[85]. It has found that intergranular cleavage at the fracture surface was shown for annealed np-Au, even if Cu (unlike Ag) does not segregate at grain boundaries, which indicates preferential dealloying path along grain boundaries due to higher energy state. For np-Au made from Au-Ag precursor alloys, segregation of residual Ag atoms at grain boundaries during annealing can weaken grain boundaries further. Weakening effect by segregation of Ag atoms along grain boundaries could be less in ball-milled np-Au than that in annealed np-Au because ball-milling can randomize the segregated Ag atoms by severe plastic deformation. It has also found that grain boundaries with higher excess volume can be formed in cold-rolled and HPT-treated np-Au due to irregular local stress induced during severe deformation of precursor Au-Cu alloys. This could also be a possible weakening mechanism of grain boundaries in ball-milled np-Au. Additionally, cusps at grain boundaries in ligaments, as seen in Fig. 4-2(l), can act as stress concentrators due to the reduction in cross-sectional area at grain boundary and this, in addition to the possible mechanisms mentioned above, could make grain-boundary opening easier.

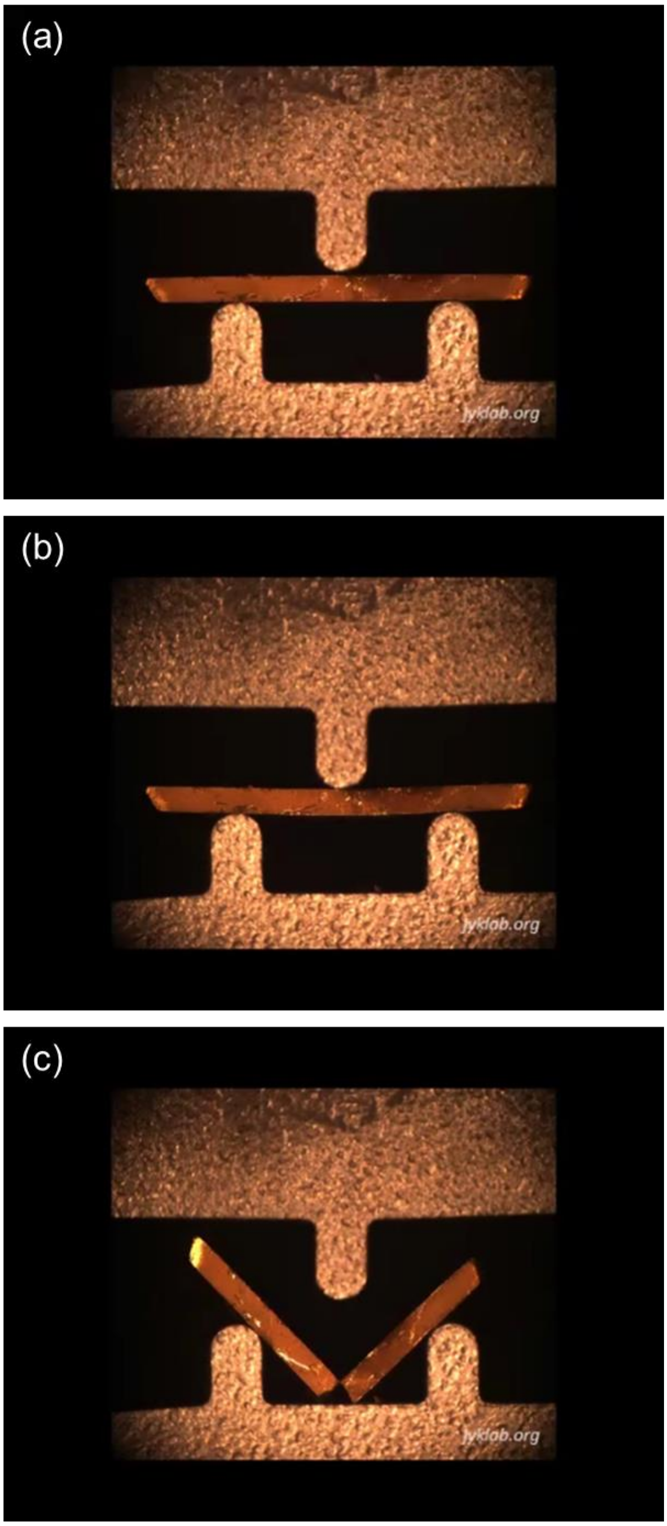

**Figure 4-6** Still images during 3-point bending test; (a) initial contact; (b) right before fracture; and (d) after fracture

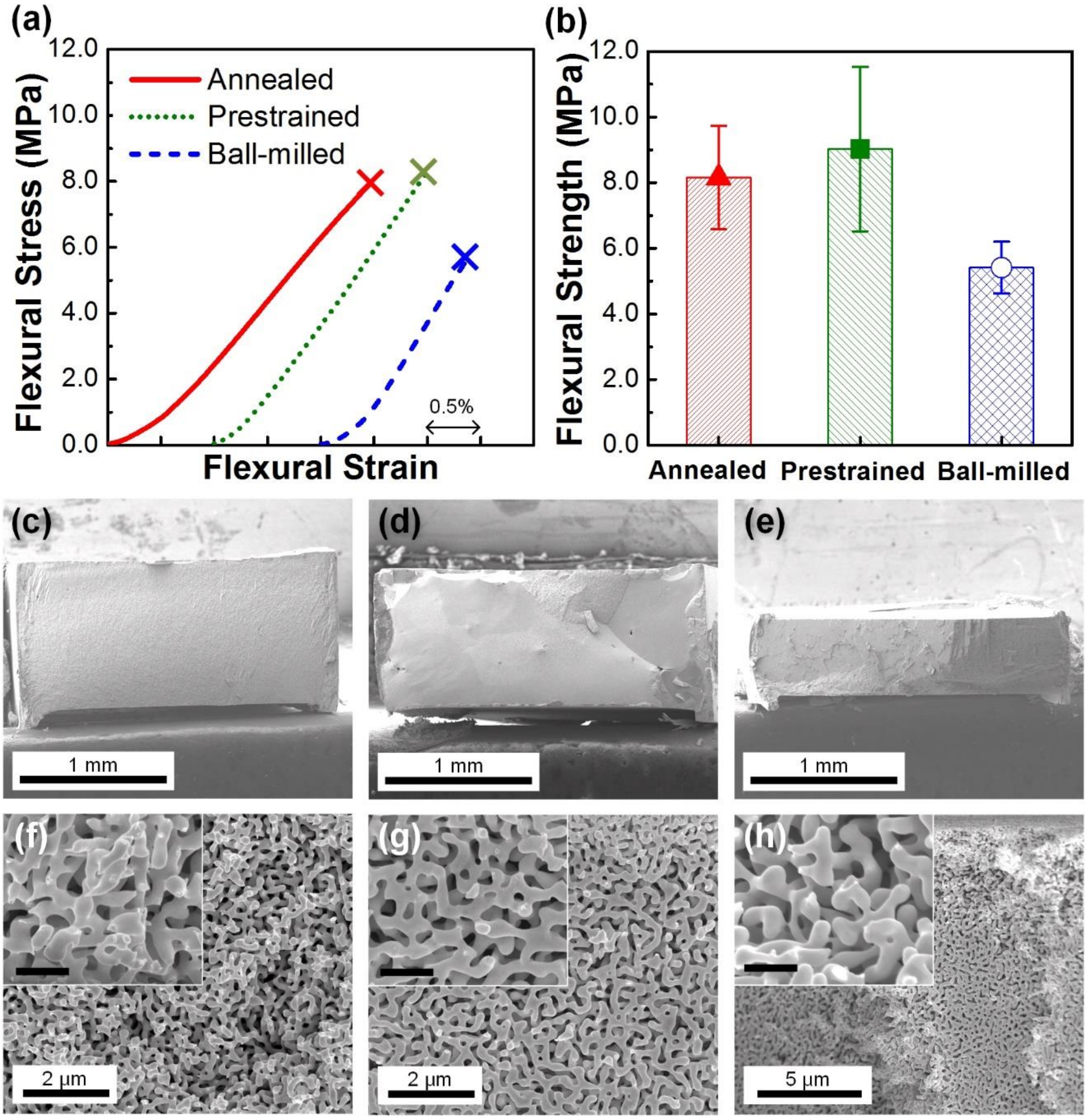

**Figure 4-7** (a) Typical flexural stress-strain curve during 3-point bending test, (b) average flexural strength of each samples, (c)-(e) fracture surface and (f)-(h) enlarged fracture surface of samples with (c), (f) transgranular fracture, (d), (g) intergranular fracture and (e), (h) ball-milled sample (adapted from Gwak and Kim Copyright 2016 American Chemical Society[15]).

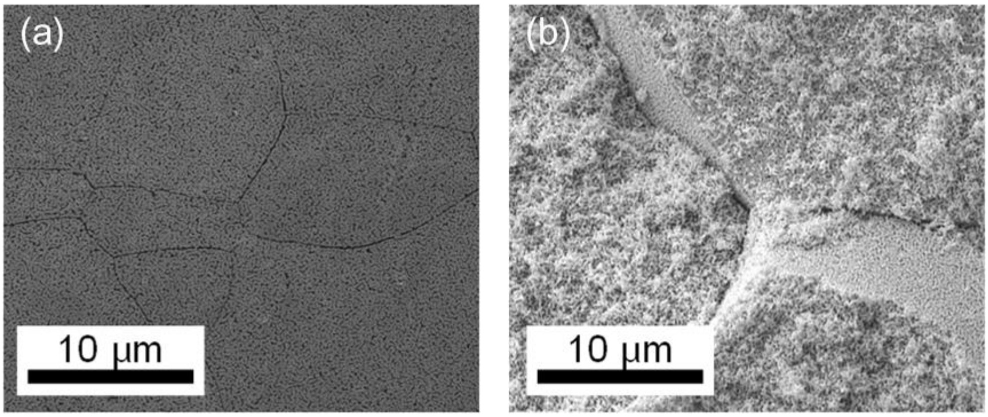

**Figure 4-8** (a) Surface morphology and (b) cross-sectional fractured surface showing grain boundary opening for annealed and prestrained np-Au.

## 4.2 Strengthening Effect of Nanotwinned Structure in Ligament of Np-Au

Twin boundary is an important interfacial defect with crystallographic mirror plane as shown in Fig. 4-9. Especially, twin boundary has low interface energy and high lattice coherency, so that it can serve as strong barrier of dislocation motion and transfer. Nanotwin structure which has high density of twin boundary in nanometer spacing have been suggested in past years due to both high strength and ductility while nanocrystalline materials have high strength but extremely low ductility. By applying nanotwin structure, twin boundaries serve as not only barrier for dislocation transfer but also dislocation source inducing ductility. Thus, twin boundary spacing could be an intrinsic characteristic length for deformation behavior and mechanical properties[86-89]. Twin structures are generally formed during bottom-up crystallization, which can be induced by physical vapor deposition[90-91] and electrodeposition[86], and severe plastic deformation[87]. To obtain nanotwin structure, materials should have low stacking fault energy and twin boundary energy for stable twin structure.

The mechanical fragility of np-Au is fundamentally attributable to its low tensile strength, which is caused by its irregular open-cell structures and results in catastrophic failure under tension[13, 58-60, 82]. The distributions of the shape, size, and surface curvature of the ligaments in np-Au are irregular. Thus, stress gets concentrated at the weak parts of the load-bearing ligaments when the material is subjected to an external tensile force. Once the weakest load-bearing ligament is ruptured, the stress concentration in the neighboring load-bearing ligaments increases, and the crack propagates rapidly. Owing to this structural nature of np-Au, efforts to enhance its tensile strength have been rare.

In this part 4.2, nanotwin structure is introduced to np-Au to enhance the tensile strength. Optimized co-sputtering condition is suggested for dense columnar nanotwin structure in Ag-Au precursor foil and nanotwinned np-Au is obtained by free-corrosion dealloying. Mechanical properties are investigated by in-situ tensile test in SEM chamber regarding with twin boundaries and tensile angle. It is revealed that nanotwin structure perpendicular tensile axis can significantly enhance ultimate tensile strength (UTS) of np-Au.

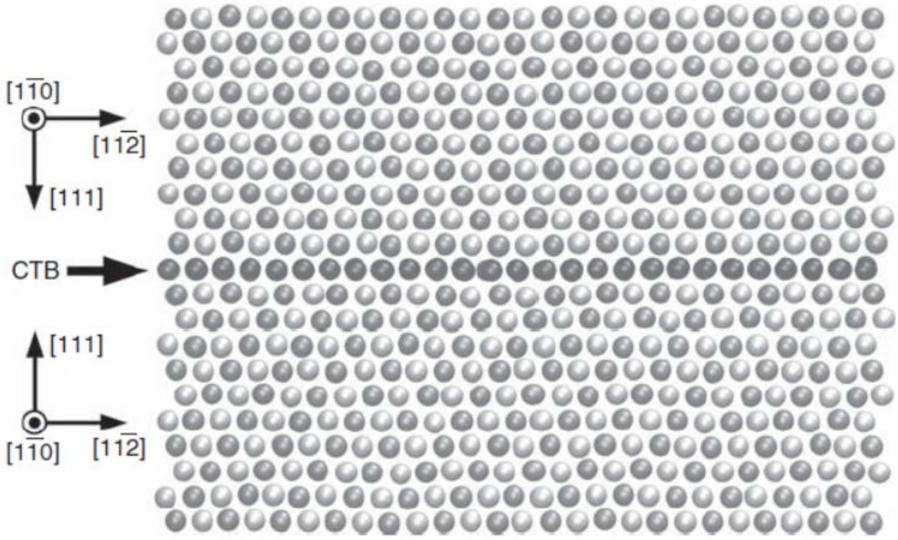

**Figure 4-9** Illustration of a CTB in FCC metals. White and gray atoms are on adjacent {110} planes (adapted from Li and Gao, Copyright 2012 John Wiley and Sons[92]).

### 4.2.1 Fabrication and Microstructure Evolution of Nanotwinned Np-Au

15 µm-thick $Ag_{70}Au_{30}$ precursor foils with high density of growth twins were deposited by co-sputtering from high purity Ag (99.99%) and Au (99.99%) targets in magnetron sputter on Si (111) substrate. Conditions for co-sputtering were base pressure of $10^{-6}$ Torr, Ar working pressure of 5 mTorr and ambient substrate temperature. A group of nanotwinned $Ag_{70}Au_{30}$ foils were annealed at 300°C for 12 hours for homogenization without grain growth and annihilation of twin structure. Another group of nanotwinned Ag70Au30 foils were annealed at 600°C for 2 hours to produce well-annealed precursor foil with large grain size. Heat treatments were carried out in tube furnace under pure $N_2$ environment. The foils were immersed in 35% nitric acid at 60°C for 48 hours for free-corrosion dealloying. Two group of np-Au samples were prepared which are nanotwinned np-Au from nanotwinned precursor and np-Au with rare twins from well-annealed precursor.

Top (top free surface plane when foil was on Si (111) substrate), bottom (plane in contact with Si (111) substrate), and cross-section views of precursor and np-Au foils were observed in SEM (FEI Nova Nano 230 FE-SEM), and chemical compositions of precursors and residual Ag in np-Au foils were measured by energy-dispersive X-ray spectroscopy (EDS) in SEM. Ligament sizes of each sample were averaged from at least 100 ligament thicknesses from SEM images at different positions; 99.2 ± 30.9 nm for nanotwinned np-Au and 110.8 ± 33.7 nm for np-Au with rare twins. Ligament sizes were measured for the thinnest necks of connecting ligaments. The amounts of residual Ag were 2.5 (±0.9) at. % for nanotwinned np-Au foil and 1.8 (±0.6) at. % for np-Au foil with rare twins in average. Grain size and texture of precursor foils were examined with electron backscatter diffraction (EBSD, TSL-OIM) in focused ion beam (FIB, FEI Quanta 3D FEG). Twin structures in precursor and nanotwinned np-Au were characterized using transmission electron microscope (TEM, JEOL JEM-2100) and high-resolution TEM (HR-TEM, JEOL JEM2100F) at accelerating voltage of 200kV. The TEM specimens were prepared by lifting out and transferring on Cu grid using tungsten micromanipulator (Omniprobe) in FIB. For TEM sampling, pores in np-Au were infiltrated with epoxy, which makes it possible to handle and thin the TEM samples of np-Au conveniently by holding dangling ligaments. Twin spacing, $\lambda$, was averaged from at least 100 measurements of distance between twin boundaries in TEM images.

Figure 4-10(a) – (d) show the microstructures of the nanotwinned $Ag_{70}Au_{30}$ precursor foils after heat treatment at 300°C for homogenization. As shown in Fig. 4-10(a), the precursor foil exhibits a <111> dominant texture with a grain size of approximately 500 nm which is in-plane directional size in columnar grain structure. Dense twin boundaries were observed on the (111) crystallographic plane, which was normal to the thickness direction of the precursor foils, for the entire volume of the foils, as shown in Figs. 4-10(b) – (d). The average twin spacing was 6.8 (± 6.6) nm. Fig. 4-10(e) – (h) show the microstructures of the nanotwinned np-Au samples prepared by free-corrosion dealloying of the precursor foils with dense twin boundaries. The ligament size of nanotwinned np-Au is 99.2 (±30.9) nm. The TEM images in Figs. 4-10(f) – (h) exhibit that the twin boundaries with high density exist over the entire volume of the nanotwinned np-Au samples. The average twin spacing in the nanotwinned np-Au samples is 7.9 (±5.9) nm, which implies that most of the twin boundaries were preserved during the dealloying process. Microstructures of the well-annealed precursor and np-Au foils are present in Fig. 4-10(i) – (k). The grain size of the well-annealed precursor is much larger than that of the precursor for nanotwinned np-Au by grain growth by annealing in higher temperature of 600°C. Further, the <111> texture is mostly maintained during the grain growth process. As shown in Fig. 4-10(j), a uniform crack-free nanoporous structure is obtained, with the average ligament size being 110.8 (±33.7) nm. The TEM images in Fig. 4-10(k) suggest that most of the twin boundaries were annihilated during heat treatment.

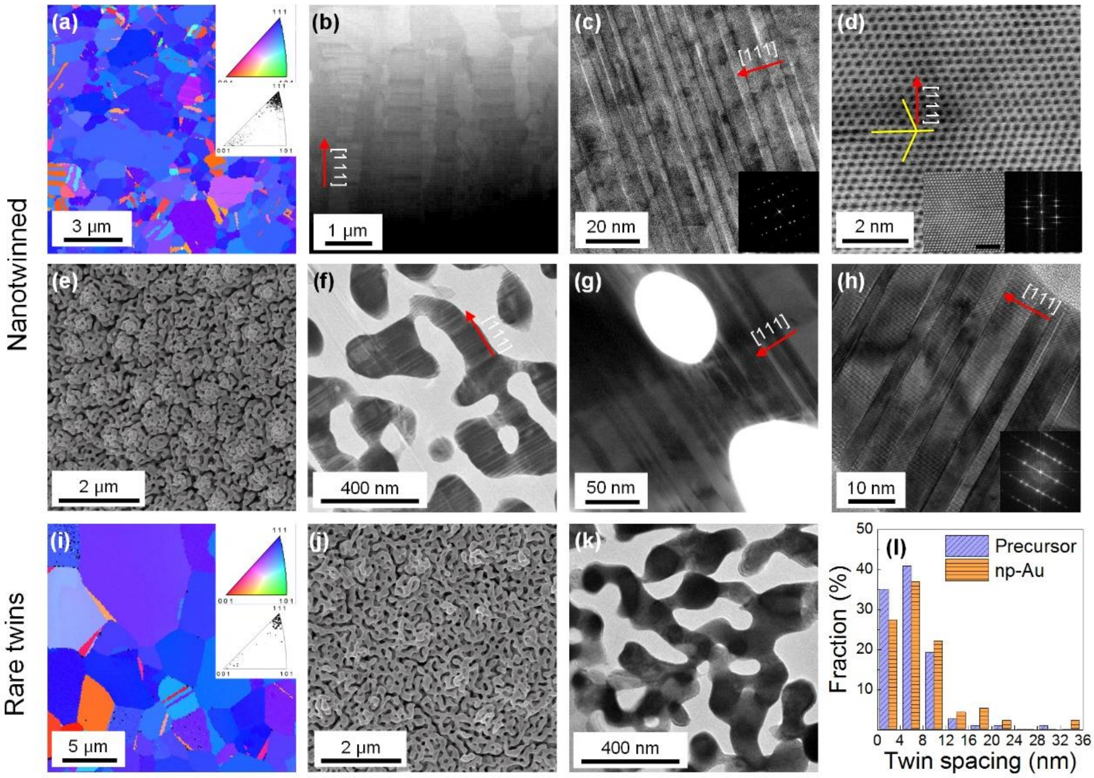

**Figure 4-10** Microstructure of precursor alloy and np-Au thin films. (a) (111) textured and (b) columnar nanotwin structure in nanotwinned precursor foil was confirmed with (c) HRTEM and (d) STEM image and diffraction pattern (inset of (d)). After dealloying, nanotwin structure preserved in np-Au foil and was confirmed with (f) and (g) TEM and diffraction pattern. Rare twin sample has (i) large grain without (k) nanotwin structure (adapted from Gwak et al., Copyright 2018 Elsevier[16]).

### 4.2.2 Deformation Behavior during In-Situ Tensile Test

To prepare micro-tensile specimens of np-Au, 3 μm-thick np-Au lamellas were machined using FIB, transferred to and attached on push-to-pull devices (Hysitron). Dog bone-shaped micro-tensile samples were machined to have dimension of 3 μm gauge width × 5 μm gauge length × 3 μm thickness by FIB milling (Fig. 4-11). Since preparation of tensile specimen utilizes FIB milling, ligaments at the outermost surface of np-Au could go through damages and contamination of Ga ions. In previous researches on Au nanopillars prepared by FIB milling, strengthening was not pronounced by the Ga ion surface damages[10, 93-94]. Even supposing surface ligaments are strengthened by the Ga ions implantation, UTS of np-Au depends on the weakest ligaments rather than hard ligaments and all the specimens are prepared by identical fabrication process using FIB. Thus, effect of Ga ions is not dominant factor determining mechanical properties of np-Au samples. In-situ micro-tensile tests were performed in SEM (FEI Quanta 200 FE-SEM) using in-situ nanoindenter (Hysitron PI-87 PicoIndenter) with a flat punch diamond indenter and strain rate was $3\times10^{-3}$ $s^{-1}$. Videos of tensile tests were recorded and still images were obtained from recorded video to analyze strain distribution during tensile test calculated using digital image correlation (DIC) technique (Correlated Solutions, VIC-2D).

Figure 4-12(a) – (c) show the tensile engineering stress-strain curves for the three types of np-Au samples: those with twin boundaries normal to the tensile loading direction (hereafter referred to as the “nanotwinned-normal” samples), those with twin boundaries inclined at 45° to the tensile loading direction (hereafter referred to as the “nanotwinned-inclined” samples), and those with rare twin boundaries and produced from the well-annealed precursor foils (hereafter referred to as the “rare twins” samples). In the case of stress-strain curves for nanotwinned-normal np-au, they can also be divided into two groups: those in gray corresponds to a high UTS and those in green corresponds to a low UTS as shown in Fig. 4-12(a). The distribution of UTS values of three types of samples are displayed in Fig.4-12(d). In the Fig.4-12(d), only nanotwinned-normal np-Au presents a bimodal UTS distribution. The average UTS was 87.5 (±9.0) MPa for high-UTS group among nanotwinned-normal np-Au, whereas average UTS was 31.5 (±8.7) MPa for low-UTS group among nanotwinned-normal np-Au. The stress-strain curves for nanotwinned-normal np-Au for the high-UTS group generally show linear elasticity, low plasticity, and catastrophic failure. On contrary, those for the low-UTS group generally indicate lower elastic modulus, low yield strength, a small degree of plasticity, and catastrophic failure. For both cases, the fracture strain is approximately 1%. However, as shown in Fig. 4-12(d), the UTS values of nanotwinned-inclined np-Au and np-Au with rare twins exhibit a unimodal distribution. The UTS of nanotwinned-inclined np-Au is 32.9 (±10.6) MPa and average UTS of np-Au with rare twins is 27.4 (±10.5) MPa that includes all the results for intergranular fracture-dominant, transgranular fracture-dominant, and mixed fracture modes.

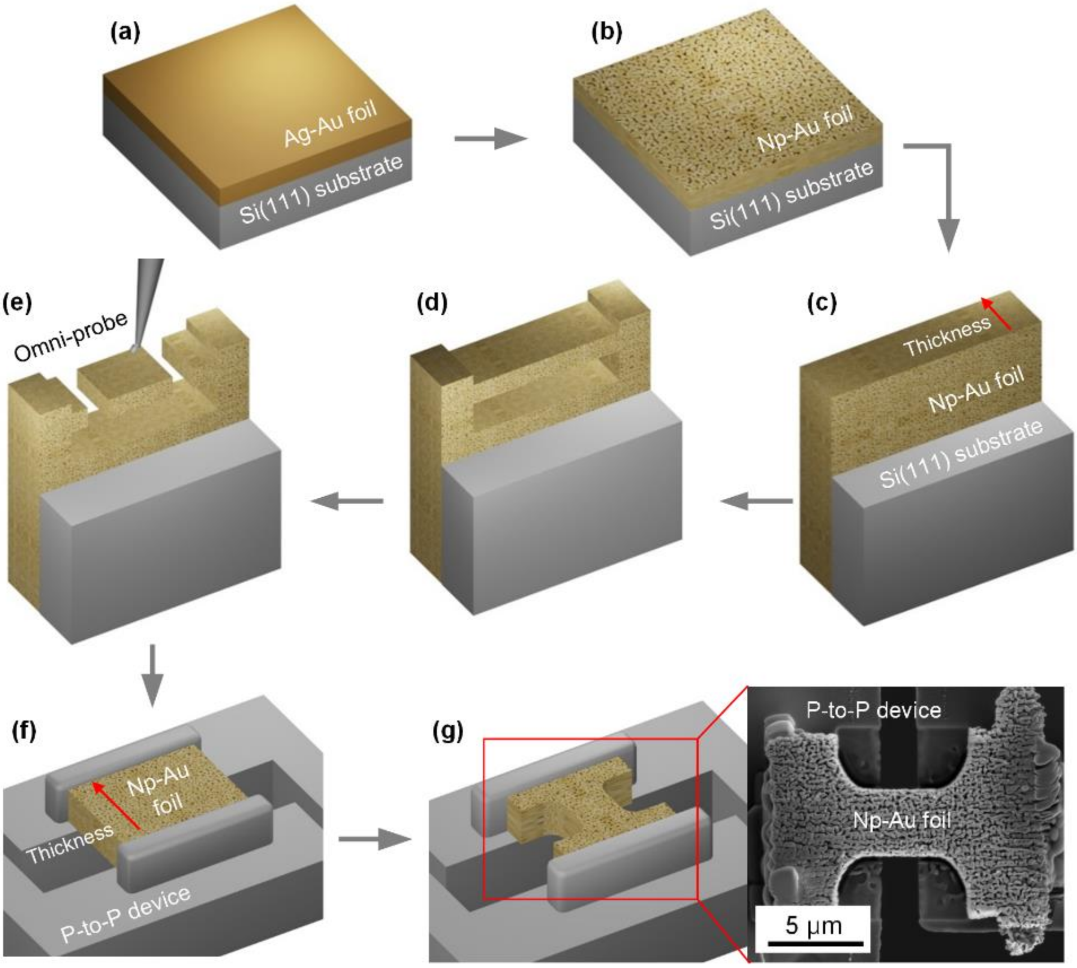

**Figure 4-11** Schematics of preparation for tensile specimen using FIB and omniprobe system. (adapted from Gwak et al., Copyright 2018 Elsevier[16]).

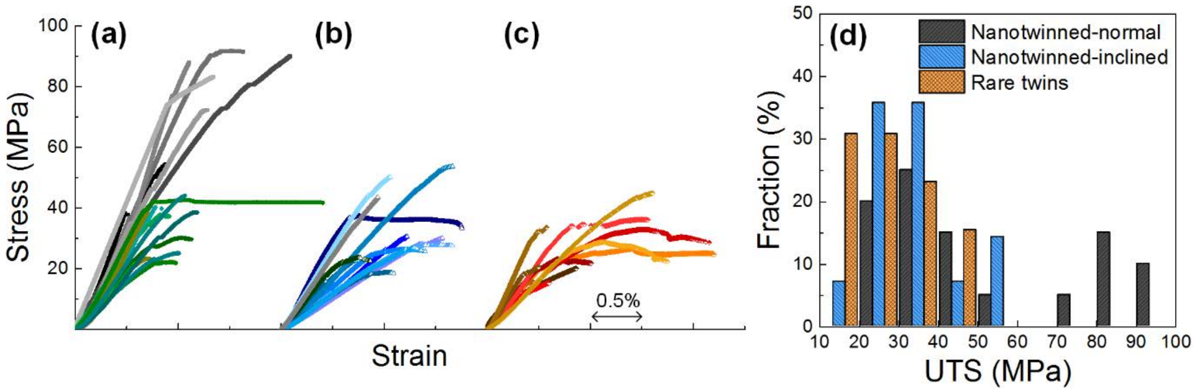

**Figure 4-12** Tensile stress-strain curves of (a) nanotwinned-normal, (b) nanotwinned-inclined np-Au and (c) np-Au with rare twins. (d) distribution of UTS of np-Au samples (adapted from Gwak et al., Copyright 2018 Elsevier[16]).

It has been reported that millimeter scale np-Au with single-crystalline structure is 28.4MPa which is comparable with UTS of low-UTS group in nanotwinned-normal np-Au and that of nanotwinned-inclined and np-Au with rare twins[60]. The UTS of nanotwinned-normal np-Au corresponding to the high-UTS group is 87.5 (±9.0) MPa. This is approximately three times greater than those for the other three cases, namely, nanotwinned-normal np-Au corresponding to the low-UTS group, nanotwinned-inclined np-Au, and np-Au with rare twins.

With similar ligament sizes and same relative density of np-Au samples, tensile properties can depend on (1) distribution of grain boundaries in the gauge section, (2) distribution of structural morphology of the ligaments, and (3) role of twin boundaries. Grain structure of Au-Ag precursor films were examined with FIB and EBSD as shown in Figs. 4-10(a), (b) and (i). Grain boundaries are randomly-distributed for np-Au with rare twins with grain size of about 5 μm, and nanotwinned np-Au has columnar grain structure along with [111] direction with grain size of about 500 nm. Dimension of the gauge section in in-situ micro-tensile testing is 3 μm width × 3 μm thickness × 5 μm length. By calculating number of grains included in gauge section of tensile specimen, there could be 36 columnar grains in gauge volume of nanotwinned-normal np-Au samples, 66 45°-inclined columnar grains in gauge section of nanotwinned-inclined np-Au samples and one or a few isotropic grains in gauge volume of np-Au with rare twins samples. In the case of nanotwinned-normal np-Au specimen, all failures were proceeded by transgranular fractures rather than intergranular fractures. It is because most of grain boundaries in nanotwinned-normal np-Au are parallel to tensile loading direction due to columnar grain structure. As shown in Fig. 4-13, grain structure in nanotwinned-normal np-Au is not perfectly columnar, so grains might be slightly tilt and have multiple junctions. This defects could be a reason to lower the UTS of nanotwinned np-Au than that with perfect columnar grain structure. As far as the tensile specimens prepared, nanotwinned-normal np-Au was failed by transgranular-way observed by SEM.

In nanotwinned-inclined np-Au samples, fracture surface was defined by angle of fracture surface to tensile axis and three failure modes are observed: (1) Intergranular fracture-dominant in which considerable cracks are propagated along 45°-inclined grain boundaries, (2) transgranular fracture-dominant in which crack propagates mainly along direction normal to tensile loading direction regardless of inclined grain boundaries, and (3) mixed mode by partial intergranular fractures and partial transgranular fractures (Fig. 4-14(a) and (b))[15]. UTS and elastic modulus for 14 nanotwinned-inclined np-Au samples are presented and failure mode for each result is indicated in Fig. 4-15(c). Any trend in UTS or elastic modulus depending on failure mode are not seen in Fig. 4-15(c) for nanotwinned-inclined np-Au samples. Therefore, it is concluded that inclined grain boundaries in nanotwinned-inclined np-Au samples do not affect UTS values significantly.

The grain size of np-Au with rare twins was approximately 5 μm isotropically, indicating that there is a few grain boundaries in the gauge section of the gauge volume of np-Au with rare twins samples. As discussed in chapter 4.1, the UTS was relatively low for intergranular fracture, while the UTS was relatively high for transgranular fracture as presented in Fig. 4-14(c) – (h) and Fig. 4-15(d). From the DIC analysis for np-Au with rare twins, severe strain localization is observed nearby intergranular fracture surface, on the other hand, strain is more distributed in gauge volume of transgranular-fractured specimen.

Figure 4-13 shows the typical stress-strain curves for nanotwinned-normal np-Au with high UTS and low UTS as well as the axial strain distributions just before failure and SEM images obtained after failure. Strain distribution of the tensile axis is uniform before failure for nanotwinned-normal np-Au with a high UTS, on the other hand, strain distribution is irregular and localized near fracture surface for nanotwinned-normal np-Au with a low UTS. One reason for this phenomenon could be the wide distribution of the local load-bearing ability due to the irregular distribution of ligaments in np-Au. The distributions of the shape, curvature, connectivity, and other parameters of the ligaments in np-Au are irregular, and so is the distribution of the pores that act as notches and result in stress concentration at the necks of the ligaments. For the np-Au samples with a high UTS and elastic modulus, the irregularity distribution is stochastically narrow, and the load-bearing ligaments can withstand a high external tensile force uniformly. However, once a ligament is ruptured, the stress concentration at the neighboring ligaments increases, and the crack propagates fast and linearly. For the case of narrow distribution of ligament strength, even when elongation or rupturing of a ligament occurs, the neighboring ligaments are strong enough to withstand the stress concentration. For the np-Au samples with a low UTS and elastic modulus, the irregularity distribution is stochastically wide. In such a case, highly strained local volumes form and the crack tends to propagate by the coalescence of the highly strained local volumes.

It is important to note that "the stiffer, the stronger" phenomenon is observed in nanotwinned-normal and nanotwinned-inclined np-Au as shown in Figs. 4-15(a) and (b). In these two samples, there are no trend in UTS depending on distribution of grain boundaries or fracture mode. Thus, for nanotwinned-normal and nanotwinned-inclined np-Au, whether strain is localized or uniform is dependent on stochastic distribution of structure morphology. But, for np-Au with rare twins, "the stiffer, the stronger" phenomenon is not observed as shown in Fig. 4-15(d). UTS for those samples is likely to depend on failure mode, i.e., UTS for intergranular fracture-dominant is generally lower than other two modes. Worse load-bearing ability of grain-boundary than grain-interior has been extensively discussed in previous works[15, 59-60]. Meanwhile, distribution of elastic modulus does not depend on failure mode. This means that initial elastic deformation is uniform in gauge section regardless of grain boundaries even if stain is severely localized at grain boundary right before the failures.

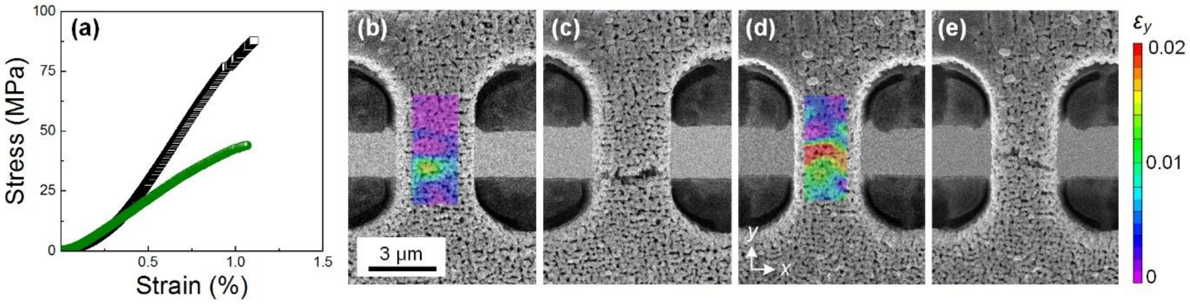

**Figure 4-13** (a) Typical stress-strain curves for nanotwinned-normal np-Au with (b), (c) distributed strain and high strength (black open squares in (a)) and localized strain and low strength (green filled circles in (a)) (adapted from Gwak et al., Copyright 2018 Elsevier[16]).

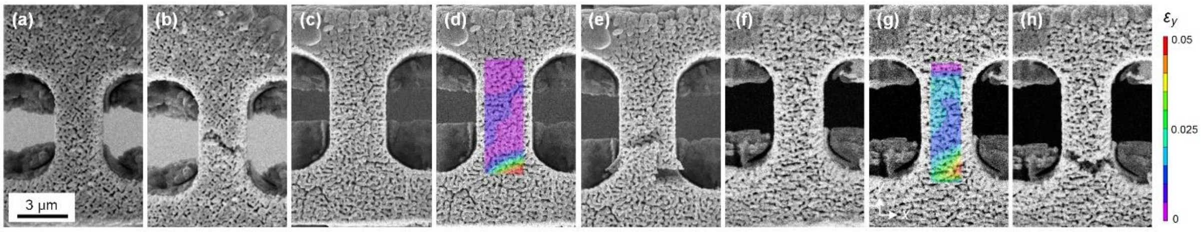

**Figure 4-14** Fracture morphology and strain distribution for (a), (b) nanotwinned-inclined , (c)-(e) intergranular fractured and (f)-(h) transgranular fractured np-Au with rare twin (adapted from Gwak et al., Copyright 2018 Elsevier[16]).

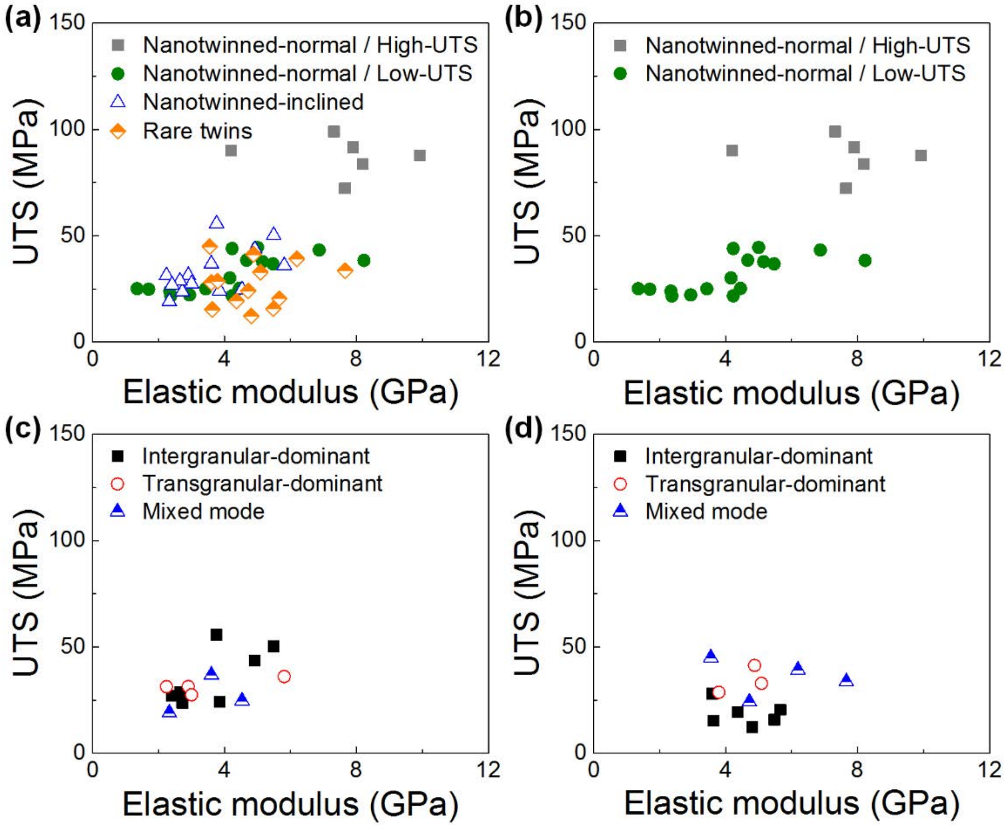

**Figure 4-15** Relation between UTS, elastic modulus and morphology of fracture surface for (a) all samples, (b) nanotwinned-normal, (c) nanotwinned-inclined np-Au and (d) np-Au with rare twins (adapted from Gwak et al., Copyright 2018 Elsevier[16]).

### 4.2.3 Ligament Plasticity

The failure of np-Au during tensile loading occurs as a result of the sequential ruptures of the load-bearing ligaments aligned along the tensile direction. Ruptures of each load-bearing ligaments are proceeded by a typical ductile failure which consists of dislocation slips, necking, and rupturing. The strength of np-Au with an irregular nanoporous structure can be explained based on the weakest link theory, wherein the strength of np-Au is closely related to the rupturing of the weakest load-bearing ligament[60, 82, 95-96]. First, the onset of plasticity and rupturing of the weakest load-bearing ligament were examined for np-Au with rare twins. The weakest ligaments were assumed to be the thinnest load-bearing ligaments with a negative surface curvature parallel to the tensile loading direction, as shown in Fig. 4-16(a). The neck volume is assumed to be a cylinder with diameter of $l$ and thickness of $l$, where $l$ is ligament diameter. When cylindrical volume with $l$ of 100 nm, the neck volume could have a total length of initial dislocations of approximately 8 nm, while the initial dislocation density in the precursor Ag-Au foil is $10^{13}$ m$^{-2}$ and all the dislocations are preserved during the dealloying process[15, 77]. This indicates that no initial dislocations are involved in the incipient plasticity observed at the neck volume or that only a few initial dislocations escape at the free surface and are starved instead of being multiplied (Fig. 4-16(a)). With respect to dislocation activity, dislocations nucleate on the free surface with a high stress concentration because of dislocation starvation in the ligament neck volume. They subsequently slip through the ligament interior, and escape at other free surface. This is known to be the primary plasticity mechanism in the ligaments of np-Au by which the necking and rupturing of the ligaments occurs[13]. The UTS of np-Au with rare twins, which was 27.4 (±10.5) MPa, is likely related to the axial stress required for these slip activities.

The UTS of nanotwinned-inclined np-Au, which was 32.9 (±10.6) MPa, was not significantly greater than that for np-Au with rare twins. Since nanotwinned structure have anisotropic nature, three dislocation slip modes could be defined in this case: mode 1 corresponds to the case where the slip plane and slip direction are inclined with respect to the twin boundaries with Burgers vector $\overrightarrow{b_1}$, as shown in Fig. 4-16(b); mode 2 indicates that the slip plane is inclined with respect to the twin boundaries and the slip direction is parallel to the twin boundaries with Burgers vector $\overrightarrow{b_2}$; and mode 3 indicates that the slip plane and slip direction are parallel to the twin boundaries with Burgers vector $\overrightarrow{b_3}$ [97-98]. The Schmid factors for modes 1, 2, and 3 are 0.484, 0.360, and 0.5, respectively, for the case where the tensile direction is at an angle of 45° with respect to the twin boundaries, as in the case of nanotwinned-inclined np-Au[99]. For nanotwinned-inclined np-Au, all three dislocation slip modes could be activated. However, mode 3, which has the highest Schmid factor, was the most preferred one. The primary dislocation activity in the nanotwinned-inclined np-Au is probably the nucleation of dislocations at the junction of the free surface and the twin boundary at the neck of the ligament, and the slip along the twin boundary ($\{\bar{1}11\}$<$01\bar{1}$> slip planes), which is a mode 3 dislocation slip called a soft slip and results in migration of the twin boundary (Figs. 4-16(c) and (d)). Therefore, np-Au with rare twins and nanotwinned-inclined np-Au have similar UTS values since stress required for slip in ligament with inclined twin boundaries is nearly similar to stress for slip in ligament without twin boundaries.

The interesting result of this work is that nanotwinned-normal np-Au in the high-UTS group has UTS as high as 87.5(±9.0) MPa. In the case of nanotwinned-normal np-Au, only the dislocation slip corresponding to mode 1, called hard slip (Schmid factor of 0.272), is activated, in contrast to the case for nanotwinned-inclined np-Au, as shown in Figs. 4-16(e) and (f). Dislocations are nucleated at the junction of the free surface and the twin boundary. These subsequently slip along the $\{\bar{1}11\}$<011> slip planes and pile up at the neighboring twin boundaries. The transmission of these dislocations through the twin boundaries and their decomposition at the boundaries are theoretically possible. However, the stress required for these events to occur is much higher than that needed for the nucleation of another dislocation at the free surface[100]. In practice, dislocation activities, surface nucleation, and slips and pile-up at the twin boundaries occur continuously. Piled-up dislocations induce higher stress due to repulsive force between them. When a coherent twin boundary is not perfect, dislocations can nucleate at the imperfect twin boundaries such as kinks where stress is concentrated[101]. In this case, following mode 1 slip and pile-up at neighboring twin boundaries are same as the case of surface nucleation. This ligament-strengthening mechanism could be a reason for the high UTS of nanotwinned-normal np-Au. The strengthening of nanotwinned-normal np-Au which deformed by slip mode 1 is in line with previous reports, that nanowires and nanopillars with dense nanotwin structure have shown significantly enhanced strength when twin boundaries are normal to loading direction. The UTS of a nanotwinned Au nanowire was found to be 3.12 GPa, which is 2.2 times greater than that (1.42 GPa) for an Au nanowire with no twins, as measured by in-situ TEM tensile testing[102]. Further, an electroplated nanotwinned Cu nanowire exhibited a UTS 1.5 times greater and a compressive yield strength 3 times greater than those of a single-crystalline Cu nanowire[88, 103].

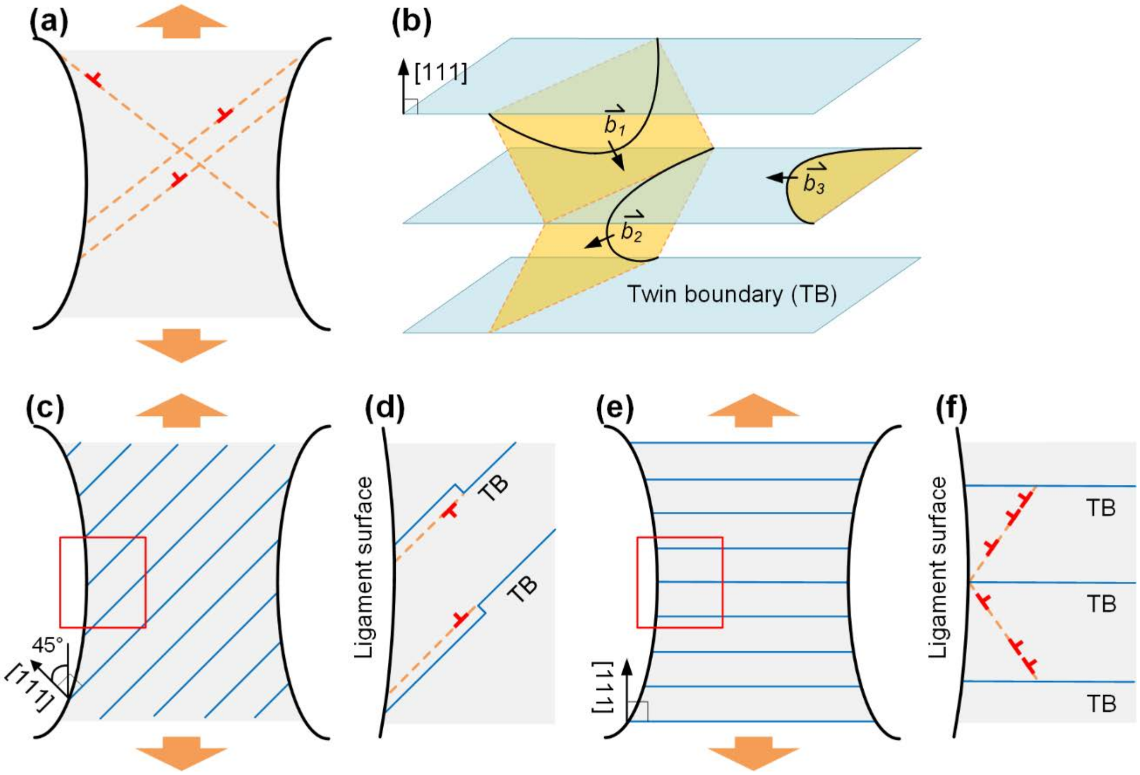

**Figure 4-16** Schematics for dislocation motion in ligaments with different microstructures. (a) single crystal ligament, (c), (d) ligament with 45°-inclined nanotwin structure and (e), (f) ligament with nanotwin structure perpendicular to ligament axis. (b) Possible dislocation path in FCC material with twin boundaries (adapted from Gwak et al., Copyright 2018 Elsevier[16]).

### 4.2.4 Bimodal Distribution for UTS of Nanotwinned-normal Np-Au

Bimodal distribution has been found in fracture strength of bundle of brittle ceramic fibers. The bimodal distribution for fracture strength is related with populations of two critical defects in the fibers; (1) intrinsic flaws from its own structure and (2) extrinsic flaws at surface introduced during manufacturing or sampling process[104-106]. Bimodal distribution is induced by lower fracture strength of fiber bundle with extrinsic flaws than that with only intrinsic flaws. If extrinsic flaws are introduced in ceramic fibers, fracture strength of fiber bundle becomes much lower than that with only intrinsic flaws, leading to bimodal distribution. Similar to bundle of ceramic fibers, gauge volume of nanotwinned-normal np-Au consists of columnar grains parallel to tensile axis as discussed in section 4.2.2.

High UTS in nanotwinned-normal np-Au samples could be accomplished when three conditions are satisfied simultaneously; (1) columnar grain structure is close to ideal columnar structure so that weakening effect of grain boundaries could not involve, (2) distribution of ligament (or pore) structure is so uniform that strain distribution is not localized severely and (3) spacing of twin boundaries is so uniform that ligament hardening by twin boundaries can occur globally in the gauge section. Some grain boundaries in the nanotwinned samples could be slightly tilt and could have multiple junctions because columnar structures are not perfect as shown in Fig. 4-10(b). If intergranular fracture which can lower UTS of np-Au occurs, high UTS is not attainable. Also, irregular pores in gauge section could act as high stress concentrators that reduce UTS of np-Au. As shown in Fig. 4-10(l), spacing of twin boundaries in nanotwinned np-Au is sometimes greater than 30 nm (average spacing is 7.9 nm in the nanotwinned np-Au). Ligament hardening by dislocation pile-up nearby twin boundaries are required to attain high UTS as discussed in section 4.2.3. But, sparse twin boundaries could be included stochastically in the ligaments disrupting strengthening of load-bearing ligaments. As in the ceramic bundles which have high UTS among bimodal distribution when only intrinsic flaws operate, high UTS of nanotwinned-normal np-Au can be obtained only if ideal columnar grains, regular porous structure and uniform and dense twin boundaries are completed at the same time. On contrary, like ceramic bundles have low UTS with extrinsic flaws, np-Au have low UTS when three conditions are not satisfied at the same time. For example, the highest UTS of nanotwinned-inclined np-Au and np-Au with rare twins is less than 60 MPa even though they satisfied conditions of transgranular fracture and uniform strain distribution because of no hardening effect of dense twin boundaries.

### 4.2.5 Relation between UTSs and Relative Density for Np-Au

Figure 4-17 shows the relation between the UTS as measured by uniaxial tensile testing or the flexural strength and the relative density for np-Au. The solid pink circles represent the results obtained in this study, while the other symbols represent the results of other studies[12, 15, 41, 58-59, 61, 78, 83, 107-109]. It is important to note that the both ligament size and the relative density are dominant factor for the mechanical strength of np-Au, and strengthening by reduction of ligament size is not pronounced in our results comparing with previous ones in Fig. 4-17. It is because the ligament size of the order of 100 nm in this chapter which is relatively large ligament size comparing with other reports. The relation between the strength of porous materials and the constituent materials can generally be expressed using the Gibson-Ashby (G-A) equation,

$$\sigma^* = C\sigma_s \left(\frac{\rho^*}{\rho_s}\right)^n, \quad (4\text{-}2)$$

where $C$ is 0.3, $n$ is 1.5, $\sigma^*$ and $\sigma_s$ are the strengths of np-Au and gold ligament, respectively, and $\rho^*/\rho_s$ is the relative density of np-Au[78]. It should be noted that the G-A equation was developed for bending-dominant deformation. Thus, the use of the G-A equation in the case of np-Au with an irregular porous structure and a relative density of approximately 30% could be inaccurate. Using Eq. (4-2) and for an np-Au strength of 27.4 MPa, the strength of a gold ligament for the np-Au with rare twins, was estimated to be 556 MPa. On the other hand, for an np-Au strength of 87.5 MPa, the ligament strength for nanotwinned-normal np-Au corresponding to the high-UTS group was determined to be 1.775 GPa. The ligament strengths estimated using Eq. (4-2) were probably lower than the actual values considering irregular connectivity in np-Au. Liu *et al*. suggested that the effective relative density, i.e. the ratio of volume of the load-bearing ligaments to the total volume of np-Au, could be reduced to approximately 25% of nominal relative density[55]. Hu *et al*. reported that the volume fraction of the load-bearing ligaments is 10–14%[53], and Kang *et al*. found that only 14% of the ligaments were broken by tensile testing when comparing with nanoporous structure with perfect connectivity[19]. Some results shown in Fig. 4-17 are lower than that estimated using Eq. (4-2) (represented by the black line) when the ligament strength is 160 MPa corresponding to that of well-annealed bulk gold, even though the size of the ligaments falls within the range corresponding to the “the small, the stronger” phenomenon[8-9, 65]. This could be because of the imperfect connectivity in np-Au. Therefore, the actual strength of ligaments in the nanotwinned-normal np-Au samples would probably be higher than the value estimated using Eq. (4-2), namely, 1.775 GPa, and would approach the theoretical strength of gold, which is 4.3 GPa.

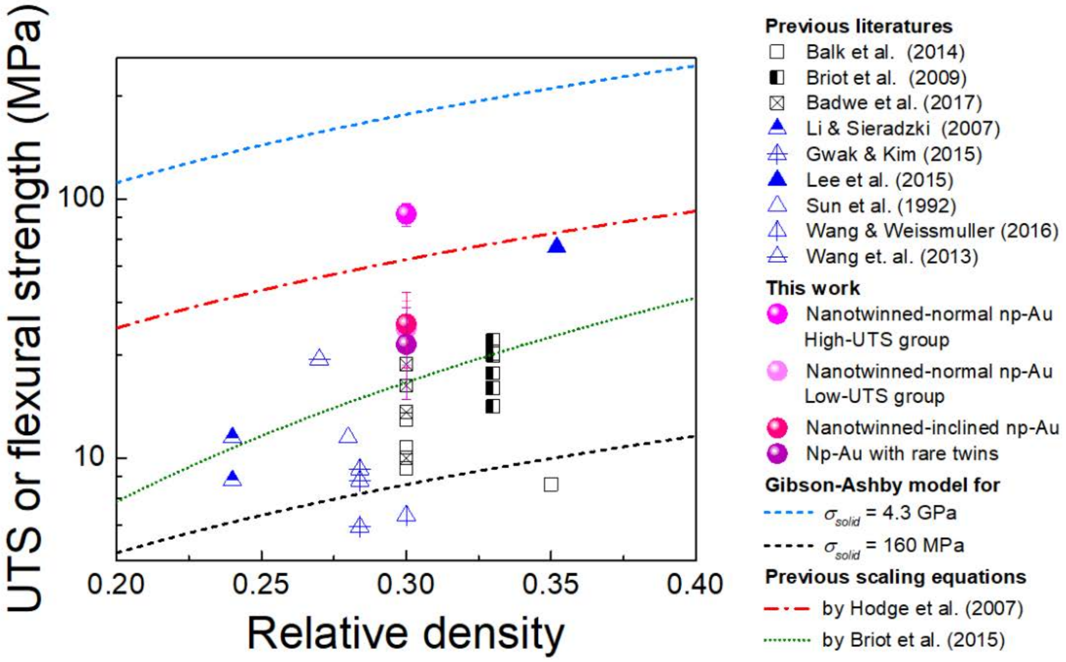

**Figure 4-17** Relation between strength and relative density of np-Au**.**

## 4.3 Conclusion

In this chapter 4, three internal microstructural factors; grain size, initial dislocation density, and twin spacing were investigated on mechanical properties and deformation behavior of np-Au. Fabrication methods using ball-milling process and prestraining precursor followed by free-corrosion were suggested for nanocrystalline and prestrained np-Au. In nanoindentation on np-Au samples, hardness of ball-milled and prestrained np-Au was not higher or lower than hardness of annealed np-Au while main deformation mechanism was changed from dislocation slip in annealed and prestrained np-Au to frictional grain boundary sliding in ball-milled np-Au confirmed by EBSD IPF map. This change in deformation mechanism give effect on creep behavior of np-Au at room temperature measured by spherical nanoindentation[110]. High dislocation density in np-Au lower creep strain exponent, $n$, and activation volume, $V^*$. On the other hand, high grain boundary density doesn't change $n$ and $V^*$, but grain boundary sliding increases creep strain rate in quasi-steady-state.

In 3-point flexural test, all three np-Au samples show brittle fracture and flexural strength of each np-Au samples were 8.16 MPa for annealed np-Au, 9.03 MPa for prestrained np-Au and 5.41 MPa for ball-milled np-Au. The relatively large scatter in flexural strength for annealed and prestrained np-Au samples depends stochastically on the distribution of grain boundaries acting as two-dimensional defects with low connectivity. Ball-milled np-Au has a much greater density of two-dimensional defects than annealed and prestrained np-Au, where intergranular fracture is preferred. Therefore, the probable existence of grain boundary opening in the highest tensile region is attributed to the flexural strength of np-Au. Excess volume by faster dealloying at grain boundaries than inside grains, segregated Ag atoms at grain boundaries, and reduction of cross-sectional area by cusp formation at grain boundaries were suggested as possible mechanisms for the grain boundary-induced weakening in the flexural strength of np-Au.

Nanotwinned np-Au could be fabricated by co-sputtering on Si (111) wafer and free-corrosion. Mechanical properties depending on nanotwin structure and angle of twin boundary to tensile axis were investigated by in-situ micro-tensile test. The UTS value of some of the nanotwinned-normal np-Au samples was 87.5 MPa and approximately three times greater than those of the other np-Au samples. The twin boundaries, which acted as effective barriers to the movement of dislocations, strengthened the load-bearing ligaments, resulting in the high UTS. In addition, the nanoporous structure was uniform enough for the strain-hardened ligaments to withstand the stress concentrated around the surrounding pores.

# 5. Conclusion

Np-Au has been widely studied due to its high surface to volume ratio by open-cell bicontinuous nanoporous structure and chemical inertness by component material, gold in order to use in sensor, catalyst, actuator, capacitor and even in template for other cellular materials. Even though np-Au holds superior characteristics and ease of fabrication technique, brittleness and complex mechanical behavior are retarding actual applications in the industrial fields.

By this dissertation, external and internal microstructural factors were considered for mechanical behavior of np-Au. Effect of ligament size, which is a representative and important external characteristic length for mechanical properties of np-Au, on indentation size effect was investigated in both sharp tip and spherical tip indentation. By nanomechanical modeling, it was revealed that indentation size effect is related with difference in dislocation motion and deformation mode in compression and shear mode. Irregular porous structure causes difference in ability for strain hardening between thinnest neck and thicker junction during bending of ligament structure in compression of np-Au. As indentation depth increases, proportion of compressive deformation is increased rather than shear deformation where ligament size dependency is higher in shear deformation than in compression inducing indentation size effect.

Effects of grain boundary, initial dislocation density and nanotwin structure, which are internal microstructural factors, on mechanical behavior of np-Au were investigated by nanomechanical tests; nanoindentation, flexural test and in-situ tensile test. Due to large free surface by nanoporous structure, there are difference in effect of microstructure on mechanical behavior comparing with bulk solid material. However, plastic deformation of np-Au is carried by dislocation movement and grain boundary sliding which shows unique mechanical responses in various deformation modes. Especially, application of nanotwin structure in ligament would enhance tensile strength of np-Au which could overcome fragility of np-Au or other np-metals.

In this study, synthesis of np-Au in bulk and thin film scale and mechanical properties of np-Au by microstructural characteristic lengths were suggested. This dissertation would play an important role in securing the mechanical reliability of various np-metal as well as np-Au.

# References

1. Qian, L. H.; Yan, X. Q.; Fujita, T.; Inoue, A.; Chen, M. W., Surface enhanced Raman scattering of nanoporous gold: Smaller pore sizes stronger enhancements. *Applied Physics Letters* **2007,** *90* (15), 153120.
2. Wittstock, A.; Biener, J.; Baumer, M., Nanoporous gold: a new material for catalytic and sensor applications. *Physical Chemistry Chemical Physics* **2010,** *12* (40), 12919-12930.
3. Wittstock, A.; Zielasek, V.; Biener, J.; Friend, C. M.; Baumer, M., Nanoporous Gold Catalysts for Selective Gas-Phase Oxidative Coupling of Methanol at Low Temperature. *Science* **2010,** *327* (5963), 319-322.
4. Lang, X.; Hirata, A.; Fujita, T.; Chen, M., Nanoporous metal/oxide hybrid electrodes for electrochemical supercapacitors. *Nature Nanotechnology* **2011,** *6* (4), 232-236.
5. Fujita, T.; Guan, P. F.; McKenna, K.; Lang, X. Y.; Hirata, A.; Zhang, L.; Tokunaga, T.; Arai, S.; Yamamoto, Y.; Tanaka, N.; Ishikawa, Y.; Asao, N.; Yamamoto, Y.; Erlebacher, J.; Chen, M. W., Atomic origins of the high catalytic activity of nanoporous gold. *Nat. Mater.* **2012,** *11* (9), 775-780.
6. Hu, K. C.; Lan, D. X.; Li, X. M.; Zhang, S. S., Electrochemical DNA Biosensor Based on Nanoporous Gold Electrode and Multifunctional Encoded DNA-Au Bio Bar Codes. *Analytical Chemistry* **2008,** *80* (23), 9124-9130.
7. Gwak, E. J.; Kang, N. R.; Baek, U. B.; Lee, H. M.; Nahm, S. H.; Kim, J. Y., Microstructure evolution in nanoporous gold thin films made from sputter-deposited precursors. *Scripta Mater* **2013,** *69* (10), 720-723.
8. Uchic, M. D.; Dimiduk, D. M.; Florando, J. N.; Nix, W. D., Sample dimensions influence strength and crystal plasticity. *Science* **2004,** *305* (5686), 986-989.
9. Greer, J. R.; Oliver, W. C.; Nix, W. D., Size dependence of mechanical properties of gold at the micron scale in the absence of strain gradients. *Acta Mater.* **2005,** *53* (6), 1821-1830.
10. Kim, J. Y.; Greer, J. R., Tensile and compressive behavior of gold and molybdenum single crystals at the nano-scale. *Acta Mater.* **2009,** *57* (17), 5245-5253.
11. Biener, J.; Hodge, A. M.; Hayes, J. R.; Volkert, C. A.; Zepeda-Ruiz, L. A.; Hamza, A. V.; Abraham, F. F., Size effects on the mechanical behavior of nanoporous Au. *Nano Letters* **2006,** *6* (10), 2379-2382.
12. Hodge, A. M.; Biener, J.; Hayes, J. R.; Bythrow, P. M.; Volkert, C. A.; Hamza, A. V., Scaling equation for yield strength of nanoporous open-cell foams. *Acta Mater.* **2007,** *55* (4), 1343-1349.
13. Sun, X.-Y.; Xu, G.-K.; Li, X.; Feng, X.-Q.; Gao, H., Mechanical properties and scaling laws of nanoporous gold. *J Appl Phys* **2013,** *113* (2), 023505.
14. Kim, Y. C.; Gwak, E. J.; Ahn, S. M.; Kang, N. R.; Han, H. N.; Jang, J. I.; Kim, J. Y., Indentation

size effect for spherical nanoindentation on nanoporous gold. *Scripta Mater* **2018,** *143*, 10-14.

15. Gwak, E. J.; Kim, J. Y., Weakened Flexural Strength of Nanocrystalline Nanoporous Gold by Grain Refinement. *Nano letters* **2016,** *16* (4), 2497-2502.

16. Gwak, E. J.; Jeon, H.; Song, E.; Kang, N. R.; Kim, J. Y., Twinned nanoporous gold with enhanced tensile strength. *Acta Mater.* **2018,** *155*, 253-261.

17. Jeon, H.; Kang, N. R.; Gwak, E. J.; Jang, J. I.; Han, H. N.; Hwang, J. Y.; Lee, S.; Kim, J. Y., Self-similarity in the structure of coarsened nanoporous gold. *Scripta Mater* **2017,** *137*, 46-49.

18. Qi, Z.; Weissmüller, J., Hierarchical nested-network nanostructure by dealloying. *ACS Nano* **2013,** *7* (7), 5948-5954.

19. Kang, N.-R.; Kim, Y.-C.; Jeon, H.; Kim, S. K.; Jang, J.-i.; Han, H. N.; Kim, J.-Y., Wall-thickness-dependent strength of nanotubular ZnO. *Scientific Reports* **2017,** *7* (1), 4327.

20. Zeis, R.; Mathur, A.; Fritz, G.; Lee, J.; Erlebacher, J., Platinum-plated nanoporous gold: An efficient, low Pt loading electrocatalyst for PEM fuel cells. *Journal of Power Sources* **2007,** *165* (1), 65-72.

21. Wittstock, A.; Zielasek, V.; Biener, J.; Friend, C. M.; Baeumer, M., Nanoporous Gold Catalysts for Selective Gas-Phase Oxidative Coupling of Methanol at Low Temperature. *Science* **2010,** *327* (5963), 319-322.

22. Biener, J.; Wittstock, A.; Zepeda-Ruiz, L. A.; Biener, M. M.; Zielasek, V.; Kramer, D.; Viswanath, R. N.; Weissmueller, J.; Baeumer, M.; Hamza, A. V., Surface-chemistry-driven actuation in nanoporous gold. *Nat. Mater.* **2009,** *8* (1), 47-51.

23. Ying, J.; Yang, X.-Y.; Tian, G.; Janiak, C.; Su, B.-L., Self-assembly: an option to nanoporous metal nanocrystals. *Nanoscale* **2014,** *6* (22), 13370-13382.

24. Xu, T.; Stevens, J.; Villa, J. A.; Goldbach, J. T.; Guarini, K. W.; Black, C. T.; Hawker, C. J.; Russell, T. P., Block copolymer surface reconstruction: A reversible route to nanoporous films. *Advanced Functional Materials* **2003,** *13* (9), 698-702.

25. Jin, I., L.D. Kenny, and H. Sang Method of producing lightweight foamed metal. 1990.

26. Erlebacher, J.; Aziz, M. J.; Karma, A.; Dimitrov, N.; Sieradzki, K., Evolution of nanoporosity in dealloying. *Nature* **2001,** *410* (6827), 450-453.

27. Ding, Y.; Kim, Y. J.; Erlebacher, J., Nanoporous gold leaf: "Ancient technology"/advanced material. *Adv. Mater.* **2004,** *16* (21), 1897-+.

28. Elliott, R. P.; Shunk, F. A., The Ag−Au (Silver-Gold) system. *Bulletin of Alloy Phase Diagrams* **1980,** *1* (2), 45-47.

29. Sun, Y.; Kucera, K. P.; Burger, S. A.; Balk, T. J., Microstructure, stability and thermomechanical behavior of crack-free thin films of nanoporous gold. *Scripta Mater* **2008,** *58* (11), 1018-1021.

30. Erlebacher, J.; Seshadri, R., Hard Materials with Tunable Porosity. *MRS Bulletin* **2011,** *34* (8),

561-568.

31. Parida, S.; Kramer, D.; Volkert, C. A.; Rösner, H.; Erlebacher, J.; Weissmüller, J., Volume Change during the Formation of Nanoporous Gold by Dealloying. *Phys. Rev. Lett.* **2006,** *97* (3), 035504.

32. Seker, E.; Reed, L. M.; Begley, R. M., Nanoporous Gold: Fabrication, Characterization, and Applications. *Materials* **2009,** *2* (4).

33. Qian, L. H.; Chen, M. W., Ultrafine nanoporous gold by low-temperature dealloying and kinetics of nanopore formation. *Applied Physics Letters* **2007,** *91* (8), 3.

34. Okman, O.; Lee, D.; Kysar, J. W., Fabrication of crack-free nanoporous gold blanket thin films by potentiostatic dealloying. *Scripta Mater* **2010,** *63* (10), 1005-1008.

35. Okman, O.; Kysar, J. W., Fabrication of crack-free blanket nanoporous gold thin films by galvanostatic dealloying. *Journal of Alloys and Compounds* **2011,** *509* (22), 6374-6381.

36. Sieradzki, K.; Dimitrov, N.; Movrin, D.; McCall, C.; Vasiljevic, N.; Erlebacher, J., The dealloying critical potential. *Journal of the Electrochemical Society* **2002,** *149* (8), B370-B377.

37. Kertis, F.; Snyder, J.; Govada, L.; Khurshid, S.; Chayen, N.; Erlebacher, J., Structure/Processing Relationships in the Fabrication of Nanoporous Gold. *Jom-Us* **2010,** *62* (6), 50-56.

38. Sun, Y.; Burger, S. A.; Balk, T. J., Controlled ligament coarsening in nanoporous gold by annealing in vacuum versus nitrogen. *Philos Mag* **2014,** *94* (10), 1001-1011.

39. Gibson, L. J.; Ashby, M. F., *Cellular Solids: Structure and Properties*. 2nd ed. ed.; Cambridge University Press: Cambridge, 1997.

40. Biener, J.; Hodge, A. M.; Hamza, A. V.; Hsiung, L. M.; Satcher, J. H., Nanoporous Au: A high yield strength material. *J Appl Phys* **2005,** *97* (2).

41. Briot, N. J.; Balk, T. J., Developing scaling relations for the yield strength of nanoporous gold. *Philos Mag* **2015,** *95* (27), 2955-2973.

42. Sun, Y.; Ye, J.; Minor, A. W. M.; Balk, T. J., In Situ Indentation of Nanoporous Gold Thin Films in the Transmission Electron Microscope. *Microsc Res Techniq* **2009,** *72* (3), 232-241.

43. Sun, Y.; Ye, J.; Minor, A. M.; Balk, T. J., In situ indentation of nanoporous gold thin films in the transmission electron microscope. *Microsc Res Techniq* **2009,** *72* (3), 232-41.

44. Hodge, A. M.; Balk, T. J., Mechanical properties of nanoporous gold. In *RSC Nanoscience and Nanotechnology*, 2012; pp 51-68.

45. Nix, W. D.; Gao, H. J., Indentation size effects in crystalline materials: A law for strain gradient plasticity. *J. Mech. Phys. Solids* **1998,** *46* (3), 411-425.

46. Kim, J.-Y.; Kang, S.-K.; Lee, J.-J.; Jang, J.-i.; Lee, Y.-H.; Kwon, D., Influence of surface-roughness on indentation size effect. *Acta Mater.* **2007,** *55* (10), 3555-3562.

47. Andrews, E. W.; Gioux, G.; Onck, P.; Gibson, L. J., Size effects in ductile cellular solids. Part II: experimental results. *International Journal of Mechanical Sciences* **2001,** *43* (3), 701-713.

48. Onck, P. R.; Andrews, E. W.; Gibson, L. J., Size effects in ductile cellular solids. Part I: modeling. *International Journal of Mechanical Sciences* **2001,** *43* (3), 681-699.

49. Kim, Y.-C.; Gwak, E.-J.; Ahn, S.-m.; Jang, J.-i.; Han, H. N.; Kim, J.-Y., Indentation size effect in nanoporous gold. *Acta Mater.* **2017,** *138*, 52-60.

50. Jin, H. J.; Kurmanaeva, L.; Schmauch, J.; Rosner, H.; Ivanisenko, Y.; Weissmuller, J., Deforming nanoporous metal: Role of lattice coherency. *Acta Mater.* **2009,** *57* (9), 2665-2672.

51. McCue, I.; Benn, E.; Gaskey, B.; Erlebacher, J., Dealloying and Dealloyed Materials. *Annual Review of Materials Research* **2016,** *46* (1), 263-286.

52. Volkert, C. A.; Lilleodden, E. T.; Kramer, D.; Weissmüller, J., Approaching the theoretical strength in nanoporous Au. *Applied Physics Letters* **2006,** *89* (6), 061920.

53. Hu, K.; Ziehmer, M.; Wang, K.; Lilleodden, E. T., Nanoporous gold: 3D structural analyses of representative volumes and their implications on scaling relations of mechanical behaviour. *Philos Mag* **2016,** *96* (32-34), 3322-3335.

54. Chen-Wiegart, Y. C. K.; Wang, S.; Chu, Y. S.; Liu, W. J.; McNulty, I.; Voorhees, P. W.; Dunand, D. C., Structural evolution of nanoporous gold during thermal coarsening. *Acta Mater.* **2012,** *60* (12), 4972-4981.

55. Liu, L.-Z.; Ye, X.-L.; Jin, H.-J., Interpreting anomalous low-strength and low-stiffness of nanoporous gold: Quantification of network connectivity. *Acta Mater.* **2016,** *118*, 77-87.

56. Ziehmer, M.; Hu, K.; Wang, K.; Lilleodden, E. T., A principle curvatures analysis of the isothermal evolution of nanoporous gold: Quantifying the characteristic length-scales. *Acta Mater.* **2016,** *120*, 24-31.

57. Gwak, E.-J.; Kang, N.-R.; Baek, U. B.; Lee, H. M.; Nahm, S. H.; Kim, J.-Y., Microstructure evolution in nanoporous gold thin films made from sputter-deposited precursors. *Scripta Mater* **2013,** *69* (10), 720-723.

58. Li, R.; Sieradzki, K., DUCTILE-BRITTLE TRANSITION IN RANDOM POROUS AU. *Phys. Rev. Lett.* **1992,** *68* (8), 1168-1171.

59. Balk, T. J.; Eberl, C.; Sun, Y.; Hemker, K. J.; Gianola, D. S., Tensile and Compressive Microspecimen Testing of Bulk Nanoporous Gold. *Jom-Us* **2009,** *61* (12), 26-31.

60. Briot, N. J.; Kennerknecht, T.; Eberl, C.; Balk, T. J., Mechanical properties of bulk single crystalline nanoporous gold investigated by millimetre-scale tension and compression testing. *Philos Mag* **2014,** *94* (8), 847-866.

61. Badwe, N.; Chen, X.; Sieradzki, K., Mechanical properties of nanoporous gold in tension. *Acta Mater.* **2017,** *129*, 251-258.

62. Mameka, N.; Wang, K.; Markmann, J.; Lilleodden, E. T.; Weissmüller, J., Nanoporous Gold—Testing Macro-scale Samples to Probe Small-scale Mechanical Behavior. *Materials Research Letters* **2016,** *4* (1), 27-36.

63. Brinckmann, S.; Kim, J. Y.; Greer, J. R., Fundamental differences in mechanical behavior between two types of crystals at the nanoscale. *Phys. Rev. Lett.* **2008,** *100* (15).

64. Meyers, M. A.; Mishra, A.; Benson, D. J., Mechanical properties of nanocrystalline materials. *Prog. Mater. Sci.* **2006,** *51* (4), 427-556.

65. Greer, J. R.; De Hosson, J. T. M., Plasticity in small-sized metallic systems: Intrinsic versus extrinsic size effect. *Prog. Mater. Sci.* **2011,** *56* (6), 654-724.

66. Ngô, B.-N. D.; Stukowski, A.; Mameka, N.; Markmann, J.; Albe, K.; Weissmüller, J., Anomalous compliance and early yielding of nanoporous gold. *Acta Mater.* **2015,** *93*, 144-155.

67. Hull, D.; Bacon, D. J., *Introduction to dislocations*. 3rd ed.; Pergamon Press: Oxford Oxfordshire ; New York, 1984; p xiii, 257 p.

68. Kim, J. Y.; Lee, K. W.; Lee, J. S.; Kwon, D., Determination of tensile properties by instrumented indentation technique: Representative stress and strain approach. *Surface and Coatings Technology* **2006,** *201* (7 SPEC. ISS.), 4278-4283.

69. Pathak, S.; Kalidindi, S. R., Spherical nanoindentation stress-strain curves. *Materials Science and Engineering R: Reports* **2015,** *91*, 1-36.

70. Swadener, J. G.; George, E. P.; Pharr, G. M., The correlation of the indentation size effect measured with indenters of various shapes. *J. Mech. Phys. Solids* **2002,** *50* (4), 681-694.

71. Oliver, W. C.; Pharr, G. M., AN IMPROVED TECHNIQUE FOR DETERMINING HARDNESS AND ELASTIC-MODULUS USING LOAD AND DISPLACEMENT SENSING INDENTATION EXPERIMENTS. *J. Mater. Res.* **1992,** *7* (6), 1564-1583.

72. Shaw, M. C.; Sata, T., THE PLASTIC BEHAVIOR OF CELLULAR MATERIALS. *Int, J. Mech. Scl.* **1966,** *8*, 469-478.

73. B.S. Murty, T. V., Nanostructured materials by high-energy ball milling. In *Encyclopedia of Nanoscience and Nanotechnology*, Nalwa, H. S., Ed. American Scientific Publishers: 2011; Vol. 10, pp 1-41.

74. ASTM C1674-08, Standard Test Method for Flexural Strength of Advanced Ceramics with Engineered Porosity (Honeycomb Cellular Channels) at Ambient Temperatures. ASTM International: West Conshohocken, PA, 2008.

75. Van Petegem, S.; Brandstetter, S.; Maass, R.; Hodge, A. M.; El-Dasher, B. S.; Biener, J.; Schmitt, B.; Borca, C.; Van Swygenhoven, H., On the Microstructure of Nanoporous Gold: An X-ray Diffraction Study. *Nano Letters* **2009,** *9* (3), 1158-1163.

76. Lu, X.; Balk, T. J.; Spolenak, R.; Arzt, E., Dealloying of Au-Ag thin films with a composition gradient: Influence on morphology of nanoporous Au. *Thin Solid Films* **2007,** *515* (18), 7122-7126.

77. Lee, S. W.; Han, S. M.; Nix, W. D., Uniaxial compression of fcc Au nanopillars on an MgO substrate: The effects of prestraining and annealing. *Acta Mater.* **2009,** *57* (15), 4404-4415.

78. Gibson, L. J.; Ashby, M. F., The Mechanics of 3-Dimensional Cellular Materials. *Proceedings*

*of the Royal Society of London Series a-Mathematical Physical and Engineering Sciences* **1982,** *382* (1782), 43-&.

79. Kheradmand, N.; Vehoff, H., Orientation Gradients at Boundaries in Micron-Sized Bicrystals. *Adv Eng Mater* **2012,** *14* (3), 153-161.

80. Ng, K. S.; Ngan, A. H. W., Deformation of micron-sized aluminium bi-crystal pillars. *Philos Mag* **2009,** *89* (33), 3013-3026.

81. Aitken, Z. H.; Jang, D. C.; Weinberger, C. R.; Greer, J. R., Grain Boundary Sliding in Aluminum Nano-Bi-Crystals Deformed at Room Temperature. *Small* **2014,** *10* (1), 100-108.

82. Biener, J.; Hodge, A. M.; Hamza, A. V., Microscopic failure behavior of nanoporous gold. *Applied Physics Letters* **2005,** *87* (12).

83. Sun, S. F.; Chen, X. Y.; Badwe, N.; Sieradzki, K., Potential-dependent dynamic fracture of nanoporous gold. *Nat. Mater.* **2015,** *14* (9), 894-+.

84. Meinel, K.; Klaua, M.; Bethge, H., Segregation and Sputter Effects on Perfectly Smooth (111) and (100) Surfaces of Au-Ag Alloys Studied by Aes. *Phys Status Solidi A* **1988,** *106* (1), 133-144.

85. Zhong, Y.; Markmann, J.; Jin, H. J.; Ivanisenko, Y.; Kurmanaeva, L.; Weissmuller, J., Crack Mitigation during Dealloying of Au25Cu75. *Adv Eng Mater* **2014,** *16* (4), 389-398.

86. Lu, L.; Shen, Y.; Chen, X.; Qian, L.; Lu, K., Ultrahigh Strength and High Electrical Conductivity in Copper. *Science* **2004,** *304* (5669), 422-426.

87. Zhao, W. S.; Tao, N. R.; Guo, J. Y.; Lu, Q. H.; Lu, K., High density nano-scale twins in Cu induced by dynamic plastic deformation. *Scripta Mater* **2005,** *53* (6), 745-749.

88. Jang, D.; Li, X.; Gao, H.; Greer, J. R., Deformation mechanisms in nanotwinned metal nanopillars. *Nat Nano* **2012,** *7* (9), 594-601.

89. Lu, L.; Chen, X.; Huang, X.; Lu, K., Revealing the Maximum Strength in Nanotwinned Copper. *Science* **2009,** *323* (5914), 607-610.

90. Velasco, L.; Hodge, A. M., The mobility of growth twins synthesized by sputtering: Tailoring the twin thickness. *Acta Mater.* **2016,** *109*, 142-150.

91. Bufford, D. C.; Wang, Y. M.; Liu, Y.; Lu, L., Synthesis and microstructure of electrodeposited and sputtered nanotwinned face-centered-cubic metals. *MRS Bulletin* **2016,** *41* (4), 286-291.

92. Li, X.; Gao, H., Mechanics of Nanotwinned Hierarchical Metals. In *Nano and Cell Mechanics: Fundamentals and Frontiers*, 2012; pp 129-162.

93. Kim, J. Y.; Jang, D.; Greer, J. R., Tensile and compressive behavior of tungsten, molybdenum, tantalum and niobium at the nanoscale. *Acta Mater.* **2010,** *58* (7), 2355-2363.

94. El-Awady, J. A.; Woodward, C.; Dimiduk, D. M.; Ghoniem, N. M., Effects of focused ion beam induced damage on the plasticity of micropillars. *Phys. Rev. B* **2009,** *80* (10), 104104.

95. Duxbury, P. M.; Leath, P. L.; Beale, P. D., Breakdown properties of quenched random systems: The random-fuse network. *Phys. Rev. B* **1987,** *36* (1), 367-380.

96. Kahng, B.; Batrouni, G. G.; Redner, S.; de Arcangelis, L.; Herrmann, H. J., Electrical breakdown in a fuse network with random, continuously distributed breaking strengths. *Phys. Rev. B* **1988,** *37* (13), 7625-7637.

97. Sansoz, F.; Lu, K.; Zhu, T.; Misra, A., Strengthening and plasticity in nanotwinned metals. *MRS Bulletin* **2016,** *41* (4), 292-297.

98. Lu, K., Stabilizing nanostructures in metals using grain and twin boundary architectures. **2016,** *1*, 16019.

99. Lu, Q.; You, Z.; Huang, X.; Hansen, N.; Lu, L., Dependence of dislocation structure on orientation and slip systems in highly oriented nanotwinned Cu. *Acta Mater.* **2017,** *127* (Supplement C), 85-97.

100. Deng, C.; Sansoz, F., Enabling Ultrahigh Plastic Flow and Work Hardening in Twinned Gold Nanowires. *Nano Letters* **2009,** *9* (4), 1517-1522.

101. Wang, Y. M.; Sansoz, F.; LaGrange, T.; Ott, R. T.; Marian, J.; Barbee Jr, T. W.; Hamza, A. V., Defective twin boundaries in nanotwinned metals. *Nat. Mater.* **2013,** *12*, 697-702.

102. Wang, J.; Sansoz, F.; Huang, J.; Liu, Y.; Sun, S.; Zhang, Z.; Mao, S. X., Near-ideal theoretical strength in gold nanowires containing angstrom scale twins. *Nature Communications* **2013,** *4*.

103. Jang, D.; Cai, C.; Greer, J. R., Influence of Homogeneous Interfaces on the Strength of 500 nm Diameter Cu Nanopillars. *Nano Letters* **2011,** *11* (4), 1743-1746.

104. Lissart, N.; Lamon, J., Statistical analysis of failure of SiC fibres in the presence of bimodal flaw populations. *J Mater Sci* **1997,** *32* (22), 6107-6117.

105. Peterlik, H.; Loidl, D., Bimodal strength distributions and flaw populations of ceramics and fibres. *Engineering Fracture Mechanics* **2001,** *68* (3), 253-261.

106. Bourahli, M. E. H., Uni- and bimodal Weibull distribution for analyzing the tensile strength of Diss fibers. *Journal of Natural Fibers* **2017**, 1-10.

107. Lee, D.; Wei, X.; Chen, X.; Zhao, M.; Jun, S. C.; Hone, J.; Herbert, E. G.; Oliver, W. C.; Kysar, J. W., Microfabrication and mechanical properties of nanoporous gold at the nanoscale. *Scripta Mater* **2007,** *56* (5), 437-440.

108. Wang, K.; Weissmüller, J., Composites of Nanoporous Gold and Polymer. *Adv. Mater.* **2013,** *25* (9), 1280-1284.

109. Wang, K.; Kobler, A.; Kubel, C.; Jelitto, H.; Schneider, G.; Weissmuller, J., Nanoporous-gold-based composites: toward tensile ductility. *NPG Asia Mater* **2015,** *7*, e187.

110. Kang, N. R.; Gwak, E. J.; Jeon, H.; Song, E.; Kim, J. Y., Microstructural effect on time-dependent plasticity of nanoporous gold. *Int J Plasticity* **2018**.

# Curriculum Vitae

## Eun-Ji Gwak

Department of Materials Science and Engineering (MSE)
UNIST (Ulsan National Institute of Science and Technology), Republic of Korea
E-mail: geunji1225@unist.ac.kr
Cell phone: +82-10-3122-1135
Google Scholar: https://scholar.google.co.kr/citations?user=wWGUUkIAAAAJ&hl=ko

## Education

| | |
|---|---|
| **2014.03. ~ 2019.08.** | **Combined Master & Ph.D. degree** (GPA: 4.0 / 4.3)<br>Materials Science and Engineering (MSE)<br>UNIST (Ulsan National Institute of Science and Technology), Ulsan, 44919<br>Republic of Korea<br>Advisor: Prof. **Ju-Young Kim** |
| **2010.03. ~ 2014.02.** | **B.S. degree** (GPA: 3.86 / 4.3, Magna Cum Laude)<br>Materials Science and Engineering (MSE) and Chemical Engineering (CE)<br>UNIST (Ulsan National Institute of Science and Technology), Ulsan, 44919<br>Republic of Korea |

## Fellowships and Awards

### ➢ Fellowships

| | |
|---|---|
| 2010.03 ~ 2014.02 | National Scholarship for Science and Engineering (KOSAF) |
| 2014.03 ~ 2017.02 | Nine Bridges Fellowship (UNIST) |
| 2017.03 ~ 2019.02 | Researching Assistance (UNIST) |

### ➢ Awards

- Best student presentation prizes in the conference of the Korean Institute of Metals and Materials (KIM)
  - Best student oral presentation, Fall meeting (2017)
  - Best student oral presentation, Spring meeting (2015)
  - Best student oral presentation, Fall meeting (2014)

# Research Experience and Skills

## ➢ Representative research works

### 1. Synthesis and characterization of np-Au with various microstructures

- Twinned np-Au with enhanced tensile strength [**Acta Materialia** 155, 253-261 (2018)]
- Weakened flexural strength of nanocrystalline np-Au by grain refinement [**Nano Letters** 16 (4), 2497-2502 (2016)]
- Microstructure evolution in np-Au thin films made from sputter-deposited precursors [**Scripta Materialia** 69 (10), 720-723 (2013)]

### 2. Investigation and modeling of deformation mechanism for nanoindentation on np-Au

- Indentation size effect for nanoindentation on np-Au using sharp indenter [**Acta Materialia** 138, 52-60 (2017)]
- Indentation size effect for spherical nanoindentation on np-Au [**Scripta Materialia** 143, 10-14 (2018)]

### 3. Metallic glass thin films in electronic applications

- Stretchable, transparent electrodes as wearable heaters using nanotrough networks of metallic glasses with superior mechanical properties and thermal stability [**Nano Letters** 16 (1), 471-478 (2016)]

## ➢ Professional skills and qualifications (management and independent-user)

- **Mechanical property characterization :**
  - In-situ tensile test in SEM, nanoindentation based mechanical analysis, micro-scale tensile, compressive, flexural tests and analysis
  - Relevant equipments : Microscale universal testing machine (Instron 5948, Instron, USA), Nanoindenter (G200, Keysight, USA), In-situ pico-indenter in SEM (Hysitron PI-87, Bruker, USA)
- **Electron microscopy :**
  - Surface & qualitative element analysis, micro-manipulation and TEM sampling process, nanostructure fabrication, crystallographic orientation analysis
  - Relevant equipments : Field emission scanning electron microscope (Nano230 & Quanta200, FEI, USA), Focused ion beam (Quanta 3D FEG & Helios 450HP, FEI, USA), Electron backscatter diffraction (TSL-OIM, AMETEK, USA), Normal transmission electron microscope (JEOL-2100, JEOL, Japan)
- **Thin film deposition :**
  - Magnetron DC & RF sputter (domestic provider / custom-made), E-beam evaporator (domestic provider / custom-made)
- **Nanoporous gold fabrication**
  - all skills are mastered; alloying, dealloying and coarsening in bulk and thin film scale

## Publications (6 publications as first author)

1. **E.J. Gwak**, H. Jeon, E. Song, N.R. Kang, J.Y. Kim, “*Twinned nanoporous gold with enhanced tensile strength”*, Acta Mater. 155 (2018) 253-261.
2. N.R. Kang, **E.J. Gwak**, H. Jeon, E. Song, J.Y. Kim, *“Microstructural effect on time-dependent plasticity of nanoporous gold”*, Int. J. Plasticity 109 (2018) 108-120.
3. Y.C. Kim*, **E.J. Gwak***, S.M. Ahn, N.R. Kang, H.N. Han, J.I. Jang, J.Y. Kim, *“Indentation size effect for spherical nanoindentation on nanoporous gold*”, Scripta Mater. 143 (2018) 10-14. (*authors contributed equally)
4. S.Y. Park, **E.J. Gwak**, M. Huang, R.S. Ruoff, J.Y. Kim, *“Nanolaminate of metallic glass and graphene with enhanced elastic modulus, strength, and ductility in tension”*, Scripta Mater. 139 (2017) 63-66.
5. Y.C. Kim*, **E.J. Gwak***, S.M. Ahn, J.I. Jang, H.N. Han, J.Y. Kim, *“Indentation size effect in nanoporous gold*”, Acta Mater. 138 (2017) 52-60. (*authors contributed equally)
6. H. Jeon, N.R. Kang, **E.J. Gwak**, J.I. Jang, H.N. Han, J.Y. Hwang, S. Lee, J.Y. Kim, *“Self-similarity in the structure of coarsened nanoporous gold”*, Scripta Mater. 137 (2017) 46-49.
7. **E.J. Gwak**, J.Y. Kim, *“Weakened Flexural Strength of Nanocrystalline Nanoporous Gold by Grain Refinement”*, Nano Letters 16(4) (2016) 2497-2502.
8. B.W. An*, **E.J. Gwak***, K. Kim*, Y.C. Kim, J. Jang, J.Y. Kim, J.U. Park, *“Stretchable, Transparent Electrodes as Wearable Heaters Using Nanotrough Networks of Metallic Glasses with Superior Mechanical Properties and Thermal Stability*”, Nano Letters 16(1) (2016) 471-478. (*authors contributed equally)
9. **E.J. Gwak**, N.R. Kang, U.B. Baek, H.M. Lee, S.H. Nahm, J.Y. Kim, *“Microstructure evolution in nanoporous gold thin films made from sputter-deposited precursors*”, Scripta Mater. 69(10) (2013) 720-723.

## Patents

1. J.Y. Kim, **E.J. Gwak**, *“Nanoporous gold thin films and manufacturing method of the same,”* Korean Patent registration number: 10-1839966
2. J.Y. Kim, E. Song, N.R. Kang, **E.J. Gwak**, H. Jeon, *“Manufacturing nanoporous gold with hierachical structures using hot rolling,”* Korean Patent registration number: 10-1972540

## Conference Presentations (as presenter, selected)

### ➢ International

1. (Oral presentation) “Enhanced tensile strength of nanotwinned nanoporous gold,” **E.J. Gwak**, H. Jeon, E. Song, J.Y. Kim, *2019 International Symposium on Nanoporous Materials by Alloy Corrosion* (Philadelphia, Pennsylvania, United States, February 2019)

2. (Oral presentation) “Nanotwinned nanoporous gold with enhanced tensile strength”, **E.J. Gwak**, H. Jeon, E. Song, N.R. Kang, J.Y. Kim, *E-MRS 2018 Spring Meeting* (Strasbourg, France, June 2018)
3. (Oral presentation) “Mechanical Behavior of Nanotwinned Nanoporous Gold”, **E.J. Gwak**, J.Y. Kim, *MRS 2017 Spring Meeting* (Pheonix, Arizona, United States, April 2017)
4. “Weakened Flexural Strength of Nanocrystalline Nanoporous Gold by Grain Refinement”, **E.J. Gwak**, J.Y. Kim, *2nd International Symposium on Nanoporous Materials by Alloy Corrosion* (Lake Bostal, Germany, September 2016)
5. (Oral presentation) “Strengthening mechanisms in nanoporous gold”, **E.J. Gwak**, Y.C. Kim, J.Y. Kim, *14th International Union of Materials Research Societies-International Conference on Advanced Materials(IUMRS-ICAM)* (Jeju, Republic of Korea, October 2015)
6. “Effect of Microstructure of Ag-Au Precursor Alloy on Mechanical Behavior of Nanoporous Gold”, **E.J. Gwak**, J.Y. Kim, *TMS 2015 Annual Meeting* (Orlando, Florida, United States, March 2015)

## Professional Experience

---

➢ **Teaching Assistant (T.A)**

**2016.03. ~ 2016.06.** Mechanical Behavior of Materials
**2015.03. ~ 2015.06.** (Marc Andre Meyers & Krishan Kumar Chawla, 2nd edition)
Ulsan National Institute of Science and Technology(UNIST)